

Copyright

by

Julia Dorothea Silge

2005

The Dissertation Committee for Julia Dorothea Silge
certifies that this is the approved version of the following dissertation:

**Sweep the Dust Away:
Infrared Kinematics of Nearby Galaxies**

Committee:

Karl Gebhardt, Supervisor

Sandra Faber

Gary Hill

Daniel Jaffe

John Kormendy

Paul Shapiro

**Sweep the Dust Away:
Infrared Kinematics of Nearby Galaxies**

by

Julia Dorothea Silge, B.S., M.A.

Dissertation

Presented to the Faculty of the Graduate School of

The University of Texas at Austin

in Partial Fulfillment

of the Requirements

for the Degree of

Doctor of Philosophy

The University of Texas at Austin

May 2005

Dedicated to my husband Robert

Acknowledgments

As with any dissertation project, many people have contributed to my training and made it possible for me to complete this research. First and foremost, I would like to acknowledge my research advisor, Karl Gebhardt. He has been generous in his investment of time and talent for me and never fails to relate to me with respect and kindness. I honestly could not have a better advisor. I want to thank the members of my committee, Sandy Faber, Gary Hill, Dan Jaffe, John Kormendy, and Paul Shapiro, for their willingness to be a part of my graduate education. I would like to thank Marcel Bergmann and Doug Richstone for their collaboration on the Centaurus A project. I would also like to thank observatory personnel at McDonald Observatory, IRTF, and Gemini Observatory for their contribution to my training and their assistance during observing runs. Dan Lester has offered consistent help with CoolSpec observing throughout my dissertation research. Bernadette Rodgers was especially helpful in understanding and using the GNIRS instrument on Gemini during the system verification process.

My parents, Paul and Linda Smith, continue to be a steady source of love and support in my life. Their decisions in my earlier years gave me wide opportunities that brought me here and our relationship still enriches my life today. My husband Robert has brought new richness and depth to my life; our marriage has been freeing and joyful for me. He has been unfailing in his support of all my endeavors and continues to selflessly desire what is best for me. Lastly, I want to acknowledge the

importance of God in all areas of my life, including the academic and professional ones. God, in His love and grace through Jesus Christ, is my source of strength for today and hope for tomorrow.

JULIA DOROTHEA SILGE

The University of Texas at Austin

May 2005

Sweep the Dust Away: Infrared Kinematics of Nearby Galaxies

Publication No. _____

Julia Dorothea Silge, Ph.D.
The University of Texas at Austin, 2005

Supervisor: Karl Gebhardt

In this dissertation, I have conducted a study of the near-infrared kinematics of a well-defined sample of nearby galaxies. I use the CO bandhead at 2.29 microns to measure the internal stellar kinematics of this sample. Observing in the near-infrared allows us to address possible biases or problems in our current kinematic understanding of galaxies (based on optical kinematics alone) and extend our knowledge to galaxies often excluded from kinematic analyses. This spectral region minimizes the effects of dust in galaxies; it is long enough to minimize dust absorption but short enough to avoid dilution of the continuum by emission from

hot dust. Also, observing at these longer wavelengths traces the older, redder stellar population and minimizes effects due to recent star formation. I have chosen a sample of nearby early-type galaxies which are well-studied in optical wavelengths to first calibrate the CO bandhead for kinematic analysis, finding that for the galaxies which have the least dust and are the best-studied, optical and near-IR kinematics are consistent. I then apply this observational treatment to study the Fundamental Plane (FP) of galaxies in an unbiased way, as well as to measure the central black hole (BH) mass of Centaurus A, a galaxy so dusty that it is inaccessible to optical kinematic techniques. For a sample of early-type galaxies, I find a FP scaling relation different from the optical relation, indicating that systematic variation in mass-to-light ratio is important in the shape of the FP. For a sample of bulge galaxies, I find a FP scaling relation moderately different from the early-type FP, pointing to relative structural differences between these families of galaxies. I find a high value for the central BH of Centaurus A, five to ten times higher than that predicted by correlations between BH mass and global galaxy properties. This result implies that galaxy bulge growth and central BH growth are not coeval. Together, these results illustrate the power of using near-infrared kinematics.

Contents

Acknowledgments	v
Abstract	vii
List of Tables	xii
List of Figures	xiii
Chapter 1 Introduction	1
Chapter 2 Calibrating the CO Bandhead for Galaxy Kinematics	7
2.1 The CO Bandhead	7
2.2 Data	8
2.2.1 The Sample	8
2.2.2 Observations and Data Reduction	9
2.3 Analysis	13
2.3.1 Extracting the Velocity Distribution	13
2.3.2 Equivalent Widths	20
2.3.3 Dust Masses	23
2.4 Results and Discussion	25
2.4.1 Comparing IR and Optical Dispersions	27
2.4.2 Dust, Equivalent Widths, and Template Make-up	30

2.4.3	Messier 32	36
2.5	Conclusions	38
Chapter 3 An All-Infrared Fundamental Plane of Early-Type Galaxies		43
3.1	Moving the Fundamental Plane Redward	43
3.2	Data	46
3.2.1	Sample	46
3.2.2	2MASS Photometric Quantities	46
3.2.3	Kinematic Observations	54
3.2.4	Data Reduction	56
3.2.5	Extracting the Velocity Distribution	57
3.3	The Fundamental Plane	62
3.3.1	Fitting the Fundamental Plane	63
3.4	Discussion	71
3.5	Conclusions	74
Chapter 4 Bulges on the Fundamental Plane of Galaxies		80
4.1	Understanding Bulges	80
4.2	Data	84
4.2.1	Sample	84
4.2.2	2MASS Photometric Quantities	85
4.2.3	Kinematic Observations	100
4.2.4	Data Reduction	102
4.2.5	Extracting the Velocity Distribution	103
4.3	Fitting the Fundamental Plane	108
4.4	Discussion	110
4.5	Conclusions	118

Chapter 5	The Central Supermassive Black Hole in Centaurus A	123
5.1	An Unusual Nearby Neighbor	123
5.2	Data	126
5.2.1	Surface Brightness Profile	126
5.2.2	Kinematic Observations	132
5.2.3	Data Reduction	133
5.2.4	Extracting the Velocity Distribution	135
5.3	Dynamical Models	140
5.4	Results	142
5.5	Discussion	148
Chapter 6	Conclusions	153
	Bibliography	157
	Vita	165

List of Tables

2.1	Basic properties of sample galaxies	40
2.2	IRAS fluxes and dust characteristics of sample galaxies	41
2.3	Derived quantities from observed spectra and properties gathered from the literature	42
3.1	Basic properties of FP sample galaxies	76
3.2	Disk/bulge decomposition parameters for lenticular galaxies	77
3.3	Properties of observed spectra and <i>K</i> -band Fundamental Plane quan- tities	78
3.4	Fundamental Plane quantites for comparison sample	79
4.1	Basic properties of bulge galaxies	119
4.2	Disk/bulge decomposition parameters	120
4.3	Properties of observed spectra and <i>K</i> -band Fundamental Plane quan- tities	121
4.4	Results for Fundamental Plane fits	122
5.1	Gauss-Hermite moments of LOSVDs for NGC 5128	152

List of Figures

2.1	Average “flat” spectrum for December 2001 run. This spectrum is constructed from over 60 observations of A stars over the course of the run, as described in the text. The features in this spectrum are real and not due to noise.	12
2.2	CO bandhead in a typical mid-K giant (dotted line with high frequency features) at our resolution and then convolved with Gaussian LOSVDs with dispersions of 100, 200, and 300 km s ⁻¹ (solid spectra). The equivalent width for this star is 13.4 Å.	13
2.3	Equivalent width of the CO bandhead as a function of spectral type. These are our measurements of equivalent width for the stellar spectra of Wallace & Hinkle (1997).	15
2.4	Dispersion measured by the fitting program for NGC 1161 as a function of the equivalent width of the input template star and the χ^2 for each fit. The error bar shown is representative for all these dispersions. For comparison, the dispersion measured for NGC 1161 allowing the program to choose templates is 274 km s ⁻¹ with $\chi^2 = 211$, lower than any of the fits using individual stars. The dashed line shows the χ^2 for an acceptable fit, given the 210 constraints.	16

2.5	Rest-frame spectra for galaxies observed at McDonald Observatory (noisy line) and for the template stellar spectrum convolved with the derived velocity distribution (smooth line). The derived velocity dispersion and its 68% uncertainty are reported for each galaxy. . . .	18
2.6	Percent accuracy to which we measure the velocity dispersion using the fitting technique described in the text versus measured S/N per pixel of the spectra. Our wavelength scale is 1.9 Å/pixel.	19
2.7	Velocity dispersion and velocity curves for NGC 2787. The open and filled triangles are for the opposite sides of the galaxy. The velocity dispersion derived for the entire galaxy as described in the text is $153 \pm 8 \text{ km s}^{-1}$	20
2.8	Dispersion correction to the equivalent width of the CO bandhead. The different symbols represent the change in measured equivalent width for stars with a range of equivalent widths convolved with Gaussian LOSVDs; the line is a fit to these data (described in the text) used to correct our galaxy equivalent width measurements.	23
2.9	Correlation between the dispersion measured from the CO bandhead and the optical dispersion from the literature. The dashed line has a slope of unity, showing where the two measurements are equal. The solid line is the best fit to the data, as described in the text. Here and in following plots, the filled circles are S0 galaxies while the open triangles are true Es.	28
2.10	Histogram showing the number of galaxies in each bin of fractional difference between infrared and optical measurements of dispersion. The median difference is 11% smaller.	29

2.11	Fractional difference between infrared and optical dispersions as a function of the ratio of dust mass to B -band luminosity. The arrows indicate upper limits on the dust mass-to-light. The dashed line represents equality between the infrared and optical measurements.	30
2.12	Properties of the sample galaxies as they relate to the measured CO bandhead equivalent width. Shown are the relationships between equivalent width and CO bandhead dispersion, IRAS dust mass, and fractional difference between infrared and optical dispersions.	32
2.13	Same as Fig. 2.12, but for the fractional weight given to low equivalent width templates.	35
2.14	Properties of the sample galaxies as they relate to the Mg_2 index (from the literature). Shown are the Mg_2 index versus CO bandhead dispersion, CO bandhead equivalent width, and fractional difference between infrared and optical dispersions.	36
3.1	Surface brightness profile and bulge/disk decomposition information for each SO galaxy. For each galaxy, the top panel presents the surface brightness profile and the bottom panel shows the ellipticity profile. In the surface brightness profile panels, the points with error bars show the major axis surface brightness profile extracted from the image using the MGE method, the dotted line shows the bulge component, the dashed line shows the disk component, and the heavy solid line shows the combined fitted surface brightness profile.	50
3.2	Same as figure 3.1.	51
3.3	Same as figure 3.1.	52
3.4	Same as figure 3.1.	53

3.5	Rest-frame spectra for galaxies observed at McDonald Observatory (noisy line) and for the template stellar spectrum convolved with the derived LOSVD (smooth line). The derived velocity dispersion and its 68% uncertainty are reported for each galaxy.	58
3.6	Same as figure 3.5 but for galaxies observed at IRTF.	59
3.7	Correlation between the dispersion measured from the CO bandhead and the optical dispersion from Trager et al. (1998). The dashed line has a slope of unity. The open circles are S0s and the filled squares are Es.	61
3.8	The r^* -band (left-hand panel) and K -band (right-hand panel) Fundamental Plane for the sample of Bernardi et al. (2003a). The best-fit FP coefficients for each band are shown; the heavy solid line is the projection of that FP in this plot. The dashed line in the r^* -band plot is the projection of the orthogonal fit of Bernardi et al. (2003a).	65
3.9	The r^* -band (left-hand panel) and K -band (right-hand panel) Kormendy relation for the sample of Bernardi et al. (2003a).	66
3.10	The all-infrared Fundamental Plane. The best-fit FP coefficients for our main sample (large squares and circles) are shown; the heavy dashed line is the projection of that FP in this plot. The open circles are S0s and the filled squares are Es. The error bars in the lower right-hand corner show typical sizes of errors for the galaxies of this sample. The small points are from the comparison sample of Bernardi et al. (2003a) using K -band photometric data, as in the right-hand panel of figure 3.8.	68

3.11	Infrared versus optical quantities from Faber et al. (1989) for sample elliptical galaxies. (a) K -band effective radius versus B -band effective radius. The dashed line shows the location of the relation $r_{eff,B} = 3.4r_{eff,K}$. (b) K -band effective surface brightness versus B -band effective surface brightness. The dashed line shows the location of $\mu_{eff,B} = \mu_{eff,K} + 5$. (c) Velocity dispersion measured using infrared wavelengths versus optical velocity dispersion. The dashed line shows where the two measurements are equal.	69
3.12	The B -band (left-hand panel) and K -band (right-hand panel) Kormendy relation for the sample elliptical galaxies.	70
4.1	Histogram showing the morphological type of the sample galaxies. .	84
4.2	Surface brightness profile and bulge/disk decomposition information for each galaxy. For each galaxy, the top panel presents the surface brightness profile and the bottom panel shows the ellipticity profile. In the surface brightness profile panels, the points with error bars show the major axis surface brightness profile extracted from the image using the MGE method, the dotted line shows the bulge component, the dashed line shows the disk component, and the heavy solid line shows the combined fitted surface brightness profile.	88
4.3	Same as figure 4.2.	89
4.4	Same as figure 4.2.	90
4.5	Same as figure 4.2.	91
4.6	Same as figure 4.2.	92
4.7	Same as figure 4.2.	93
4.8	Same as figure 4.2.	94
4.9	Same as figure 4.2.	95
4.10	Same as figure 4.2.	96
4.11	Same as figure 4.2.	97

4.12	Same as figure 4.2.	98
4.13	Same as figure 4.2.	99
4.14	Rest-frame spectra for galaxies observed at McDonald Observatory (noisy line) and for the template stellar spectrum convolved with the derived LOSVD (smooth line). The derived velocity dispersion and its 68% uncertainty are reported for each galaxy.	106
4.15	Same as figure 4.14 but for galaxies observed at IRTF.	107
4.16	The infrared Fundamental Plane of bulges. The best-fit FP coeffi- cients for the bulges (starred symbols) are shown; the heavy dashed line is the projection of that FP in this plot. The open circles are S0s and the open squares are Es from Silge & Gebhardt (2005). The error bars in the lower right-hand corner show typical sizes of uncertainties for these galaxies. The small points are from the sample of Bernardi et al. (2003a) using <i>K</i> -band photometric data, as detailed in Silge & Gebhardt (2005).	109
4.17	The three projections of the FP viewed in the coordinates of the observed quantities. The symbols are the same as in Figure 4.16. Panel (b) shows the projection closest to edge-on (which is also the Kormendy relation), panel (c) shows the projection closest to face-on, and panel (a) is intermediate.	111
4.18	The Faber-Jackson relation. The open circles are S0s and the open squares are Es from Silge & Gebhardt (2005), and the starred symbols are bulges from this chapter. The error bars in the lower right-hand corner show typical sizes of uncertainties for these galaxies. The solid line shows the slope of $L \propto \sigma^4$ in this plot.	112

4.19	Same as Figure 4.16, but showing differences between the bulge sample by morphological type. Red symbols represent S0/a or Sa galaxies, orange symbols represent Sab galaxies, green symbols represent Sb galaxies, blue symbols show Sbc galaxies, and violet symbols show Sc, Scd, and Sd galaxies.	113
4.20	Same as Figure 4.16, but showing differences between barred, unbarred, and intermediate galaxies. Magenta symbols represent unbarred galaxies, violet symbols present barred galaxies, and teal symbols show galaxies which are intermediate.	114
5.1	Contour map of the 2MASS LGA <i>K</i> -band image of NGC 5128. Overlaid are the contours of the MGE best-fitting model; this model's profiles are shown in Figure 5.2. The contours are logarithmically spaced but arbitrary.	128
5.2	Left panels: comparison between the 2MASS LGA <i>K</i> -band photometry of NGC 5128 (open squares) and the (N=6) Gaussian MGE best-fitting model (solid line). The individual Gaussian components are also shown. The angles noted in the upper right hand corner of each panel are measured relative to the photometric major axis. Right panels: radial variation of the relative error along the profiles.	129
5.3	<i>K</i> -band ellipticity as a function of radius along the major axis for NGC 5128.	130

5.4	<i>K</i> -band surface brightness for NGC 5128. The dashed line is from the MGE fitting of the 2MASS LGA image and the solid line is from the <i>HST</i> data of Schreier et al. (1998). The <i>HST</i> data have been adjusted to match the 2MASS data between 2 and 10". The arrow indicates the radius at which light from the AGN dominates; the profile within this radius has been extrapolated from the <i>HST</i> data outside this radius.	131
5.5	Spectrum for one spatial bin 0."45 from the galaxy center. The left panel shows the spectrum dominated by the AGN emission; the right panel shows the spectrum after this AGN continuum shape has been removed.	134
5.6	Rest-frame spectra for seven example spatial bins (noisy line) and for the template stellar spectrum convolved with the derived LOSVD for that bin (smooth line). The derived second moment of the LOSVD and its 68% uncertainty is reported for each of these bins. The left panels show data from the axis perpendicular to the dust disk; the right panels show data from the axis parallel to the dust disk but offset from the center.	137
5.7	Gauss-Hermite moments of the LOSVDs along the slit perpendicular to the dust disk (filled circles) and along the slit parallel to the dust disk but offset from the center (open circles). The filled squares are from Peng et al. (2004) and are along the same axis as the filled circles.	138

5.8	Two-dimensional plots of χ^2 as a function of BH mass and M/L ratio for both orientations we modeled. The left-hand panel shows models with rotation along the galaxy's photometric major axis (PHOT models) and the right-hand panel shows models with rotation along the dust disk (DUST models). The points represent models. The contours were determined by a two-dimensional smoothing spline interpolated from these models and represent $\Delta\chi^2$ of 1.0, 2.71, 4.0, and 6.63 (corresponding to 68%, 90%, 95%, and 99% for 1 degree of freedom).	144
5.9	The χ^2 goodness of fit obtained by comparing model kinematics to observed kinematic data for NGC 5128, versus model black hole mass. The dashed line and open squares are for the models with the rotation axis along the dust disk (DUST models), and the solid line and filled circles are for the models with the rotation axis along the photometric major axis of the galaxy (PHOT models).	145
5.10	Comparison of observed kinematic data along each slit for NGC 5128 with model kinematics for the two best-fitting edge-on models. The left-hand panel compares to the best-fitting edge-on model with rotation along the photometric major axis (PHOT models) and the right-hand panel compares to the best-fitting edge-on model with rotation along the dust disk (DUST models). The open symbols are the data: circles for the axis parallel to the dust disk but offset from the center and squares for the galaxy photometric major axis. The filled circles are from the model on the axis parallel to the dust disk and the starred squares are from the model on the galaxy photometric major axis.	146

- 5.11 Same as figure 5.8 but for models with PHOT configuration and with inclination of 45° (left-hand panel) and 20° (right-hand panel). . . . 147

Chapter 1

Introduction

Much of our detailed knowledge of local galaxies is based on kinematic measurements made using optical spectroscopy. Such measurements are difficult or nearly impossible, however, for galaxies that contain a significant amount of dust. Dust lanes are normally seen in spiral galaxies and in about half of all ellipticals. Depending on the level of dust obscuration, these kinds of galaxies are often excluded from kinematic samples, introducing bias into our current understanding. Important regions of the parameter space of galaxies are not well-studied because the traditional tools we use are unreliable or even ineffective. In this project, we have developed, calibrated, and applied methods for near-infrared kinematic measurements to address concerns with our current dynamical knowledge of galaxies and expand such knowledge to galaxies that are not well-studied.

Before infrared detectors became available, the amount of dust in a galaxy was estimated from patchy, optically visible obscuration. However, since dust emits in the far infrared, observing in that part of the spectrum gives a better measure of the total amount of dust. More recent far-infrared observations have shown that galaxies, even ellipticals and bulges of galaxies, contain an unexpectedly large amount of dust (Goudfrooij & de Jong 1995). This dust may bias the optical region

by skewing photometric and/or kinematic data through absorption and scattering. Observing in the near infrared allows us to minimize these problems. Previous attempts at studying kinematic dust effects were limited to those galaxies with obvious concerns. There has been no systematic investigation based on a general galaxy population. Our goal here is to quantify these effects by studying a subset of galaxies that are thought to have minimal dust problems (early-type galaxies) and then move on to apply this observational treatment to galaxies which we know are affected by dust.

Observing at these longer wavelengths traces the older, redder stellar population and minimizes effects due to recent star formation. Thus, kinematics in this spectral regime should produce the best measure of the underlying stellar potential of the galaxy. As infrared instrumentation and telescopes become more efficient, this region is quickly becoming very important. As a first step, we must characterize the IR features for kinematic analysis. Furthermore, analysis of these possible biases and problems is important to accurately interpret the data we have from very large optical samples such as SDSS.

Observations using the Infrared Astronomical Satellite (IRAS) have shown that galaxies, even those previously thought to be practically dust-free such as ellipticals and bulges of galaxies, can contain a large amount of dust. Dust masses determined from far infrared IRAS flux densities are about a factor of 10 higher than those estimated from optically visible patches and lanes (Goudfrooij & de Jong 1995). More sophisticated estimates of the dust mass using submillimeter data give values even higher (Kwan & Xie 1992; Wiklind & Henkel 1995). There is much more dust out there than is apparent when observing in the visible. Goudfrooij & de Jong (1995) explain this by suggesting that most of this dust exists as a diffusely distributed component, which would be undetectable in the optical regime.

How does dust affect our measurements of galaxies? Models of elliptical

galaxies considering only dust absorption show effects on both the photometric and kinematic data. The photometric effects include a global attenuation, strong extinction in the central regions, and an increasing apparent core radius (Baes & Dejonghe 2000). The core radius is one of the primary parameters used to study galaxy correlation functions and according to these models appears larger than its true value because the luminosity profile is flattened towards the center by the dust. The core radius can increase by over 25% for an optical depth $\tau \approx 2$ (a moderate amount of dust), an important effect considering the small amount of scatter in the galaxy correlation functions. The effects of absorption on kinematic properties (Baes et al. 2000), calculated by building semi-analytic dusty galaxy models and then modeling the synthetic data assuming no dust, depend on the shape of the velocity dispersion tensor of the input model. For radial and isotropic orbital structures, the inferred dynamical mass is significantly underestimated while the inferred orbital structure is mostly unaffected. For an optical depth $\tau \approx 2$, the dynamical mass appears 20% smaller. For galaxies with tangential orbital structures, the dynamical mass is not affected much but the inferred orbital structure appears more radial, even for small amounts of dust. Both these effects are due to dust preferentially obscuring light from high-velocity regions of the galaxies. Baes et al. (2000) find that dust absorption does not significantly affect the velocity dispersion but that the dynamical structure is not correctly recovered. Baes & Dejonghe (2001, 2002) construct models with both dust absorption and dust scattering (using Monte Carlo methods), and find different effects on the observed kinematics which still depend on the orbital structure of the input galaxy. At small radii, dust causes the central dispersion to appear smaller for radial and isotropic galaxies and to appear larger for tangential galaxies. This effect is small; an optical depth $\tau \approx 2$ causes a change of a few percent. There are dramatic changes at large radii, however. The attenuation by dust, mostly the scattering, results in high-velocity wings in the line-of-sight velocity

distribution (LOSVD) in the outer parts of the galaxy. For $\tau \approx 1$, the projected dispersion at large radii can increase by over 40%. Both these effects (at small and large radii) are caused by the scattering of light from high-velocity stars into lines of sight at which such stars do not exist.

Galaxies which are visibly dusty pose a less subtle problem. Although they, too, may have a diffusely distributed gas component, the high level of obscuration of visible light from patches and lanes hinders optical spectroscopy of the galaxies. There are a significant number of galaxies out there for which the existing kinematic data are suspect and untrustworthy because of visible dust. Dust lanes are normally seen in all spiral galaxies and about half of all ellipticals (Kormendy & Djorgovski 1989; Lauer et al. 1995; van Dokkum & Franx 1995; Rest et al. 2001; Tran et al. 2001), with higher detection rates as search techniques (especially spatial resolution) improve. These galaxies are often not included in kinematic studies because data for them are unreliable, introducing potential bias into current kinematic samples. It is important to observationally constrain how observed galaxy kinematics are being affected or biased by interstellar dust.

Galaxy kinematics are measured in the optical using several different spectral features. The most common include the H and K lines (Ca II) near 4000 Å, the Mg *b* lines near 5175 Å, and the Ca II triplet near 8500 Å. Studies comparing kinematic measurements made using different features, such as Nelson & Whittle (1995), do not find significant differences between them, although Barth et al. (2002) find the Mg *b* lines are sensitive to template mismatch and the details of the fitting procedure while the Ca II triplet is much more robust. All these spectral features may be affected by dust to some extent. Dust is very opaque in the *B* band where the H and K lines are located and absorbs less efficiently at longer wavelengths. At 5000 Å, dust absorption is 75% of that in *B* and decreases to 40% in *I* where the Ca II triplet is located. Moving to a feature like the Ca II triplet certainly reduces

problems associated with extinction, but effects from dust can be further minimized by moving to longer wavelengths. The extinction in the K band is only 7% of that at B (Gaffney et al. 1995; Baes & Dejonghe 2002).

In this project, we measure the stellar kinematics in a sample of nearby early-type galaxies using the K -band CO absorption bandhead. Using wavelengths this long will allow us to avoid dust absorption and gain a more accurate understanding of the kinematics of these galaxies. This sample will provide a check of possible kinematic biases using optical light. Calibrating the CO bandhead for galaxy kinematic measurements is an important goal of this study, as well as applying this treatment to more interesting, dusty galaxies. Working in the near infrared holds great promise for both scientific motivations and future instrumentation. Specifically, adaptive optics, in which the optical system is continually adjusted to compensate for the effects of seeing, work best in the near infrared. The longer wavelengths in this part of the spectrum allow less stringent requirements on optics adjustment. Using the CO bandhead will optimize kinematic analysis for adaptive optics.

This technique can also be extended to other scientific questions. Our current understanding of the kinematics of galaxies has led to the study of relations between different characteristics of galaxies in κ -space (i.e. Fundamental Plane, Faber-Jackson relation, Tully-Fisher relation; e.g. Burstein et al. 1997). These relations have been derived using data from optical stellar emission lines, so dusty, complicated, messy galaxies are not included in the analyses. The galaxy sample itself may be biased because of the exclusion of these galaxies. Also, if bulges and elliptical galaxies have a diffusely distributed dust component, these analyses may suffer from important problems due to internal absorption and extinction. Observing in the K band would avoid these problems. In this project, we calibrate the CO bandhead for kinematic analysis, use CO bandhead kinematics along with K -band photometry to build an all-IR Fundamental Plane, and use these techniques

to measure the central black hole mass of Centaurus A.

Chapter 2

Calibrating the CO Bandhead for Galaxy Kinematics

2.1 The CO Bandhead

The $2.29\ \mu\text{m}$ (2-0) ^{12}CO absorption bandhead from evolved red stars is the strongest absorption feature in galactic spectra in the $1\text{--}3\ \mu\text{m}$ range. This is the optimal range for studying stellar kinematics because it is long enough to minimize extinction from dust but short enough to avoid dilution of the stellar continuum by hot dust (Gaffney et al. 1995). The feature is in a dark part of the infrared sky spectrum and is intrinsically sharp and deep, making it very sensitive to stellar motions (Lester & Gaffney 1994).

The CO bandhead is present in late-type stars, increasing in strength with decreasing effective temperature or increasing radius. The CO bandhead has been used to measure the stellar kinematics of galaxies in recent years, but only in galaxies such as starbursts and mergers where optical kinematic measurements are seriously hindered (Tamura et al. 1991; Gaffney et al. 1993; Doyon et al. 1994; Lester & Gaffney 1994; Shier et al. 1994, 1996; Puxley et al. 1997). Before this study,

there were no velocity dispersion measurements from the CO bandhead for galaxies which are well-studied in the optical, and thus there is no information on possible differences between optical and infrared kinematics.

2.2 Data

2.2.1 The Sample

Table 2.1 shows the 25 galaxies in this section of the project. The sample contains ellipticals and lenticulars, and has redshifts less than 5000 km s^{-1} . Our sample is made largely of galaxies from Tonry et al. (2001). Tonry et al. (2001) present distance moduli for 300 nearby galaxies from surface brightness fluctuations. This presents an ideal sample to draw from for this study; these galaxies are systems with bulges (mostly E and S0, with some S), are essentially complete to a redshift of 1000 km s^{-1} , and have well-determined distances (which are necessary to calculate the dust mass and other physical properties). The galaxy type and heliocentric velocity (from NED), distance modulus (from Tonry et al. 2001), and the calculated distance are listed in Table 2.1. The sample contains about twice as many S0 galaxies as classical ellipticals, which is reflective of the galaxies in the SBF sample at these redshifts. For the few galaxies in this sample that are not in Tonry et al. (2001), the distance is calculated from the recessional velocity using $H_0 = 70 \text{ km s}^{-1} \text{ Mpc}^{-1}$. This is relatively accurate because the few galaxies without distance moduli have redshifts $> 2000 \text{ km s}^{-1}$. These galaxies have a range of IRAS dust characteristics, from no detectable dust to several million solar masses of dust (see Section 3.3). All galaxies have associated IRAS fluxes from Knapp et al. (1989) and the 1994 correction to those data (available at <http://cdsweb.u-strasbg.fr/CDS.html>).

2.2.2 Observations and Data Reduction

Observations were taken during 27 nights in six observing runs between December 2000 and January 2002. We use CoolSpec (Lester et al. 2000), a near-infrared grating spectrometer, on the 2.7-m telescope at McDonald Observatory to measure the stellar kinematics in our sample. CoolSpec has a 256×256 HgCdTe NICMOS III detector array. Using a 240 l/mm grating and $1.8'' \times 90''$ slit, our spectral resolution is 2300, measured from calibration lamp lines. This gives a full width half maximum (FWHM) resolution of approximately 130 km s^{-1} , which allows us to study galaxies with velocity dispersions down to approximately 50 km s^{-1} . Resolving the dispersions of early-type galaxies is easily within reach of this observational set-up. We have obtained spectra for about 40 galaxies, 27 of which are early-type. We have successfully extracted the line-of-sight velocity distribution for 25 of these galaxies, which make up the sample for this project. The other two galaxies were too large on the chip to allow for good sky subtraction.

The spatial and spectral scale are $0''.35 \text{ pixel}^{-1}$ and $24.6 \text{ km s}^{-1} \text{ pixel}^{-1}$, respectively. The latter gives a spectral range of just under $0.05 \mu\text{m}$, which is large enough to provide good coverage of the CO bandhead and continuum on both sides. Technically, the true continuum is not seen redward of $2.29 \mu\text{m}$ because of the long wing of CO absorption that makes the bandhead, but this is not important for our fitting technique.

We observed multiple types of stars along with the galaxies; G and K giants were observed as examples of templates for the velocity fitting and A dwarfs were observed to obtain the shape of a “flat” spectrum. These dwarf stars have nearly featureless spectra in this region (Wallace & Hinkle 1997) and are extremely important to the data reduction. The imager in CoolSpec is cooled separately from the dispersive optics, requiring the use of a filter just in front of the detector to reduce the thermal background incident on the array. This filter shape must be removed

during data reduction. Also, the atmospheric absorption at McDonald Observatory appears to vary on a timescale inconvenient for these observations. Atmospheric transmission calculations (Gaffney et al. 1995) indicate that telluric absorption is dominated by CH_4 , not H_2O , blueward of $2.34\ \mu\text{m}$, implying that atmospheric absorption should not vary much with time. This is not consistent with our experience at McDonald Observatory, however; the shape of a single A star spectrum can change significantly during a night. For both of these reasons, it is very important to take a careful (and frequent) measure of the detailed spectral shape of the filter/sky to be able to remove this shape from the observed spectra. We choose A dwarfs spatially near each galaxy and observe one before and after each galaxy/template observation. We also observe an A dwarf sometime in the middle of long galaxy observations.

The observations are made by dithering the telescope $30''$ across the slit to measure the sky at the same slit position in alternating exposures. Individual exposures are 120 seconds for the galaxies and ten seconds for the stars. Total integration times for the galaxies vary from about one hour to almost five hours. Galaxies that require very long integration times or that are at low declinations are observed during several nights to maintain reasonable airmasses. The slit is rotated to the position angle of the galaxy major axis as quoted in the RC3. Ar and Ne (or Xe for some runs) emission lamps calibrate the wavelengths of the exposures. Calibration exposures are taken every 24 minutes; the wavelength solution drifts significantly with time. The telescope guides on either the galaxy itself or a nearby star (if available) using the optical dichroic mirror autoguider. No attempt is made to flux calibrate the spectra since we are mainly concerned with the kinematic analysis.

Data reduction proceeds in several steps. First, the images are rectified spectrally using the arc lamp emission lines. We find that there is an additive constant across the entire chip which varies from exposure to exposure, so this dark

current is measured for each exposure and then subtracted out. We measure this in the same location for each exposure, in pixels without signal from either slit position. We make a master background image for each galaxy by masking out the object spectrum in each individual exposure— half of which have the object at one position on the slit, and half of which have it at another position— calculating the biweight, a robust estimator of the mean (Beers et al. 1990), of all the exposures. Galaxies observed on different nights, for long periods of time, or during particularly humid nights required the construction of several different background images to get good subtraction. We find that we must choose carefully how much exposure time to average together: long enough to make a smooth, robust background image but short enough to allow for changes in the sky. This background image is then subtracted from each individual exposure. The images are next shifted to the same wavelength solution; we interpolate between the two closest calibrations to find a good estimate of the wavelength solution and then shift all the images from one observing run to the same solution. This step must be done after the background subtraction or the image of the seams between the detector’s four quadrants does not subtract out well. All the images are then shifted so that the center of the galaxy in each image is aligned; we calculate the biweight of all the processed images to make one image for the galaxy. The one-dimensional spectra are extracted from the two-dimensional images for basically the entire galaxy; we choose the number of columns to extract to maximize signal-to-noise. For the sample, this varies between 4'' and 20''. For some high S/N galaxies, we are also able to extract spatially resolved spectra. The stellar spectra are reduced in a similar manner.

To remove telluric absorption and the filter shape, the galaxy and template stellar spectra must be divided by a “flat” spectrum. After trying several approaches, we obtained the best results by using the following procedure. First, all the A dwarfs from a run are averaged together to make a smooth, high S/N

sky spectrum. Figure 2.1 shows such an average spectrum for the December 2001 run. The galaxy, template, and individual “flat” spectra are divided by this smooth spectrum. For some galaxies and template stars, this provides good flattening. For the rest, the spectrum is divided by a version of the A dwarf nearest in time to that observation, smoothed by the resolution element to reduce noise. Dividing by only an individual A star does not give results as good as the smooth sky spectrum made from many A stars because of the fluctuations in the individual spectra. These individual stars change because of fluctuations in the sky, not because of problems with S/N.

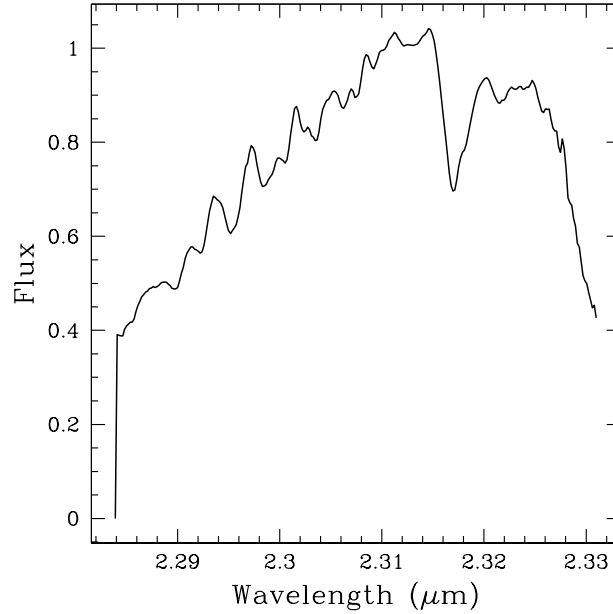


Figure 2.1: Average “flat” spectrum for December 2001 run. This spectrum is constructed from over 60 observations of A stars over the course of the run, as described in the text. The features in this spectrum are real and not due to noise.

2.3 Analysis

2.3.1 Extracting the Velocity Distribution

A galaxy spectrum is the convolution of the line-of-sight velocity distribution (LOSVD) with an average stellar spectrum. Figure 2.2 shows several examples; the dotted spectrum with many small features is that of a typical K giant while the smooth spectra are the stellar spectrum convolved with three Gaussian LOSVDs (with dispersions of 100, 200, and 300 km s^{-1}). This figure shows the smoothing and broadening due to the internal velocities. The bandhead is obviously very broad, but its sharp blue edge allows us to measure accurately the kinematics.

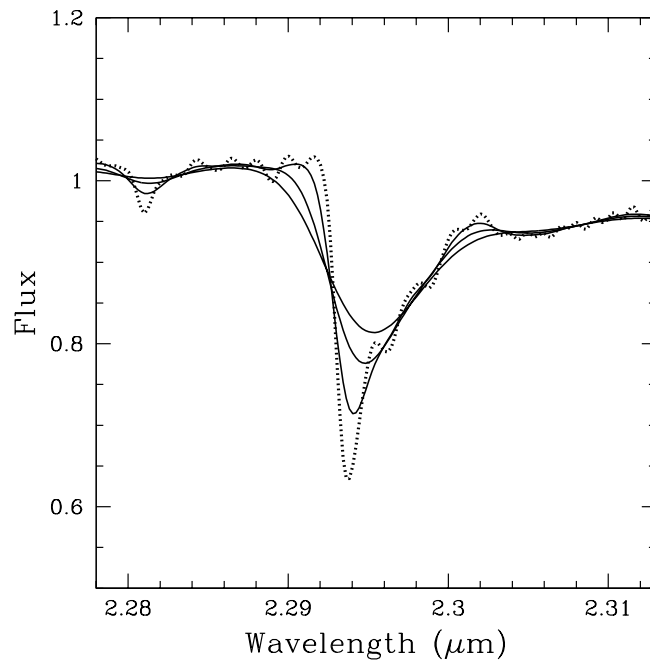


Figure 2.2: CO bandhead in a typical mid-K giant (dotted line with high frequency features) at our resolution and then convolved with Gaussian LOSVDs with dispersions of 100, 200, and 300 km s^{-1} (solid spectra). The equivalent width for this star is 13.4 \AA .

There are several techniques used to obtain the internal kinematic information from a galaxy spectrum. The cross-correlation technique (Tonry & Davis 1979) extracts the velocity dispersion utilizing the cross-correlation function of the galaxy spectrum and template stellar spectrum; the width of the peak of the cross-correlation function provides the dispersion. This technique requires correct subtraction of the continuum and is sensitive to template mismatch. The Fourier quotient technique (Sargent et al. 1977) uses the result of the convolution theorem: the Fourier transform of the LOSVD is the quotient of the Fourier transform of the galaxy spectrum and the Fourier transform of the template spectrum. Both of these techniques fit the kinematics in Fourier space; however, the spectrum can also be fit directly in pixel space, which is the approach taken here.

We use the fitting technique of Gebhardt et al. (2000c), deconvolving the spectrum using a maximum penalized likelihood estimate to obtain a nonparametric LOSVD. An initial velocity profile is chosen and this profile is convolved with a stellar template spectrum. The residuals to the galaxy spectrum are calculated and the velocity profile is changed to minimize the residuals and provide the closest match to the observed galaxy spectrum.

The choice of template star proves to be important for the fitting results. Previous work in the CO bandhead used mostly K and M giant stars as templates, but it is not clear that this is a correct choice. We use the atlas of Wallace & Hinkle (1997) to test the effect of stellar type on the fitting results. The equivalent width of the CO bandhead is a function of the effective temperature and surface gravity of the star; either increasing the surface gravity or decreasing the temperature increases the equivalent width. Figure 2.3 shows our calculations of the equivalent widths of most of the stars of Wallace & Hinkle (1997); these trends are evident.

We have found that the dispersion measured by the fitting program depends on the template spectrum chosen for the fitting. Figure 2.4 illustrates this point

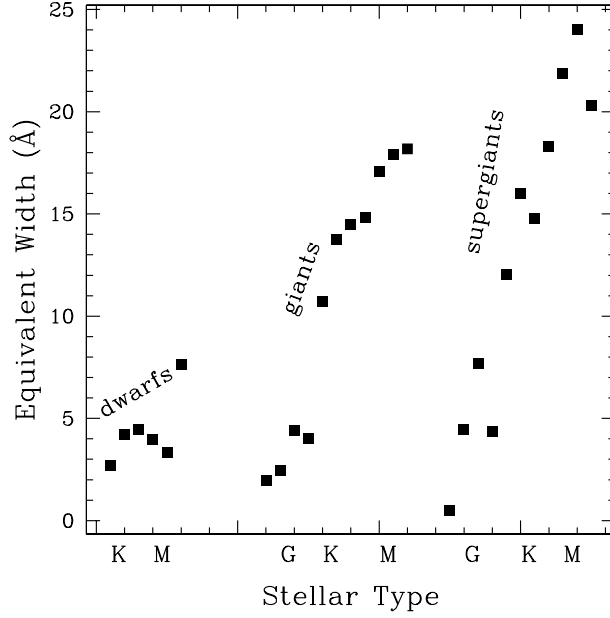


Figure 2.3: Equivalent width of the CO bandhead as a function of spectral type. These are our measurements of equivalent width for the stellar spectra of Wallace & Hinkle (1997).

for NGC 1161. The dispersion measured for this galaxy increases as the equivalent width of the template star’s bandhead increases. The χ^2 for each of these fits is shown as well and is quite high for most, indicating poor fits. One template with an equivalent width near the galaxy’s equivalent width appears to give a significantly better fit. Other galaxies show a similar trend. The shape of the CO bandhead must be a function of equivalent width. To obtain a reliable dispersion measurement, we give the fitting program a variety of template stellar spectra and allow it to vary the weights given to the different stars to obtain the best fit. As a result, along with the LOSVD information, the fitting program also provides stellar population information. We have explored the effect on the fitting of using stars of the same equivalent width but different stellar types; this does not seem to be important. It is

the equivalent width of the template that counts, not the details of the spectral type. We choose eight stars from Wallace & Hinkle (1997) to use as our available templates. These stars have a range of equivalent widths, ranging from less than 5 Å to over 20 Å. The best fit almost always gives most of the weight to a few of the template stars. We have also used template stars observed with the same instrumental setup used for the galaxies. We find similar results using these stars but the better S/N and larger equivalent width variation of Wallace & Hinkle (1997) make that dataset more useful. These spectra have a somewhat higher spectral resolution than ours, so before using them as stellar templates we have carefully convolved them to our spectral resolution.

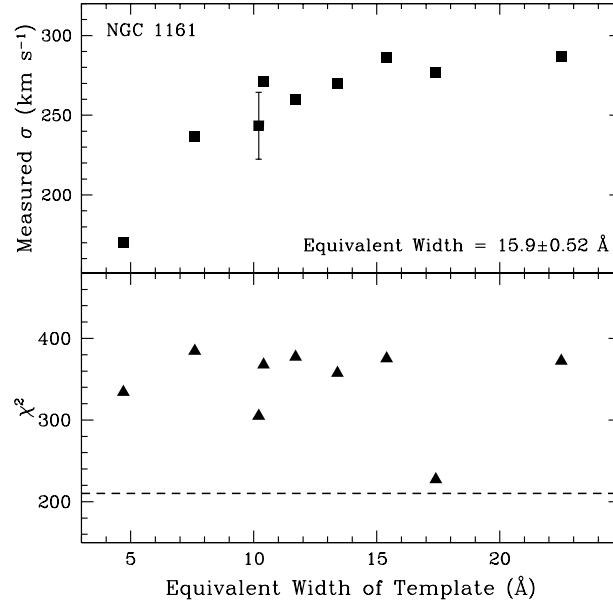


Figure 2.4: Dispersion measured by the fitting program for NGC 1161 as a function of the equivalent width of the input template star and the χ^2 for each fit. The error bar shown is representative for all these dispersions. For comparison, the dispersion measured for NGC 1161 allowing the program to choose templates is 274 km s⁻¹ with $\chi^2 = 211$, lower than any of the fits using individual stars. The dashed line shows the χ^2 for an acceptable fit, given the 210 constraints.

Because of this equivalent width effect, the continuum choice may skew the velocity dispersion measurement. If the red continuum chosen is too blue, i.e. encroaching on the bandhead, the measured equivalent width will be too low and the resulting measured velocity dispersion will be lower than the true dispersion. We have tested the effects of the continuum choice and find that this is not a large source of uncertainty. We convolved a stellar template with Gaussian LOSVDs and made different choices for the red continuum. The effect was as expected but was not large. Only very obviously bad choices for the red continuum cause a 10% decrease in the dispersion; more realistic mistakes in the continuum choice cause decreases of less than 5%, smaller than most of our error bars. We have also examined the effects of changing the continuum definition in the actual galaxy spectra; the changes in the LOSVD fits and velocity dispersions are very small.

This fitting technique obtains a nonparametric LOSVD; no a priori assumptions about the shape of the LOSVD are made (except that it is nonnegative in all bins). To measure a dispersion from this nonparametric LOSVD, we fit a Gauss-Hermite polynomial to it and use the second moment as the dispersion. We can also fit a Gaussian LOSVD directly to the spectrum. Galaxies in the sample with low S/N required the assumption of a Gaussian LOSVD in order to achieve a sensible velocity distribution. The fitting program can get lost in residual space when there are too many free parameters for the level of noise in the spectrum, and this was the case for the lower S/N galaxies in our sample. We compared the derived nonparametric and Gaussian LOSVDs for galaxies with higher S/N and found good agreement between them. Figure 2.5 shows the results for all 25 sample galaxies and the derived velocity dispersion for each galaxy. The noisy line is the observed spectrum for each galaxy and the smooth line is the template stellar spectrum convolved with the derived LOSVD.

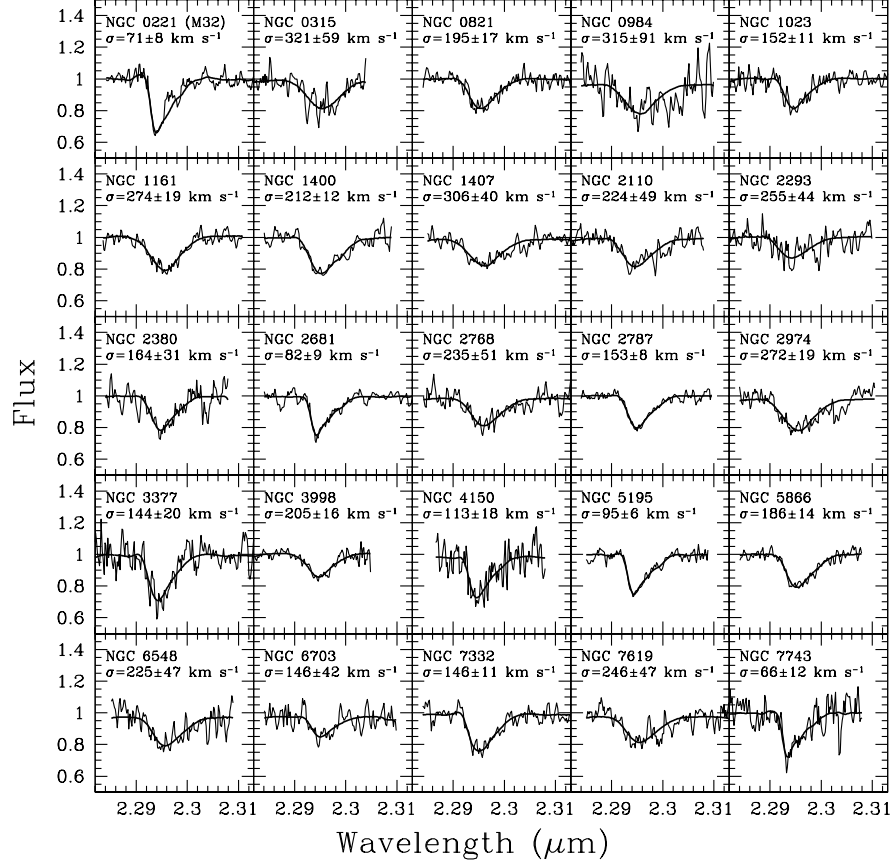


Figure 2.5: Rest-frame spectra for galaxies observed at McDonald Observatory (noisy line) and for the template stellar spectrum convolved with the derived velocity distribution (smooth line). The derived velocity dispersion and its 68% uncertainty are reported for each galaxy.

The uncertainties for these galaxies are determined using the Monte Carlo bootstrap approach of Gebhardt et al. (2000c). For each galaxy, a template spectrum is convolved with the derived LOSVD to make an initial galaxy spectrum. We then generate 100 realizations of the galaxy spectrum by randomly drawing the flux values at each wavelength from a Gaussian distribution. The mean of this distribution is the value of the initial template spectrum convolved with the LOSVD (i.e. the smooth line in Fig. 2.5) and the standard deviation is the root-mean-square of the initial fit. These 100 synthetic galaxy spectra are then deconvolved to determine the LOSVDs. These LOSVDs provide a distribution of values for each velocity bin which allow us to estimate the uncertainty and examine any bias in the dispersion. To generate the 68% confidence bands, we choose the 16% to 84% values from the 100 realizations. The median of the distribution determines any potential bias from the initial fit. Figure 2.6 shows how the S/N of the observed galaxy spectrum affects the percent accuracy to which we can measure the dispersion. Using this technique and spectral feature, 10% accuracy in the velocity dispersion requires S/N per pixel of about 25 or 30.

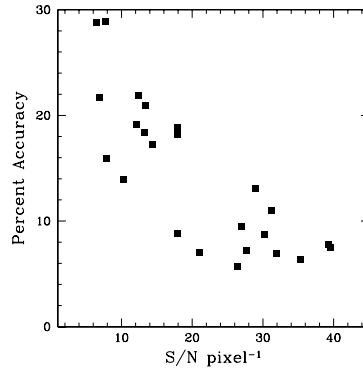


Figure 2.6: Percent accuracy to which we measure the velocity dispersion using the fitting technique described in the text versus measured S/N per pixel of the spectra. Our wavelength scale is 1.9 Å/pixel.

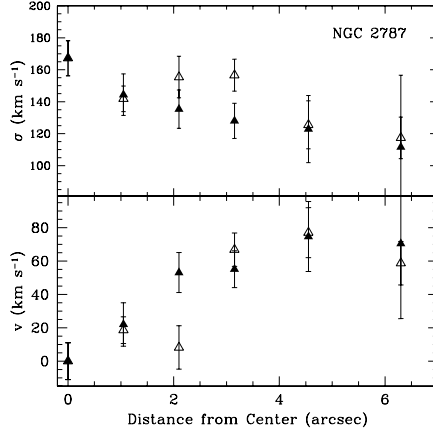


Figure 2.7: Velocity dispersion and velocity curves for NGC 2787. The open and filled triangles are for the opposite sides of the galaxy. The velocity dispersion derived for the entire galaxy as described in the text is $153 \pm 8 \text{ km s}^{-1}$.

It is possible to obtain spatially resolved kinematics from these data as well, when the S/N for the galaxy is high enough. Figure 2.7 shows the variation of velocity and velocity dispersion with distance from the center of the galaxy for NGC 2787. In the center regions, we extract spectra of approximately the width of the seeing disk for that night and in the outer regions, we increase the number of pixels extracted to keep the S/N high enough to derive the LOSVD. The velocity dispersion curve is peaked in the center of the galaxy, and both sides of the galaxy show the same decrease. The velocity dispersion measured for the entire galaxy (extracted to maximize S/N) is $153 \pm 8 \text{ km s}^{-1}$. Figure 2.7 shows that this is the value achieved by the velocity dispersion curve between 0.5 and 1.5 arcseconds away from the center.

2.3.2 Equivalent Widths

The equivalent width of the $2.29 \mu\text{m}$ CO feature can be used to quantify stellar population effects in these galaxies. To measure the equivalent width, we define

continuum on both sides of the feature and fit a straight line between these two points. In the rest frame of the galaxy, the continuum on the blue is defined to be the median between 2.287 and 2.290 μm , and on the red between 2.304 and 2.307 μm (about 15 pixels on each side). We use the velocity information from the LOSVD fitting procedure to shift the galaxy spectra to their rest frames. We measure the area between the continuum line and the observed spectrum between 2.290 and 2.304 μm , and divide by the continuum to find the equivalent width. Since true continuum is not seen redward of the feature, we choose to define the quasi-continuum where the spectrum again becomes nearly horizontal.

We calculate uncertainties for the equivalent width using the same Monte Carlo method used for the velocity dispersion. We generate 100 realizations of each galaxy spectrum from the fit to the observed spectrum found by the LOSVD fitting procedure, with noise chosen to match the S/N of the observed spectrum. We measure the equivalent width of these 100 synthetic galaxy spectra and use this distribution of equivalent widths to estimate the uncertainty and examine bias. We choose the 16% to 84% values from this distribution for our 68% uncertainty, and use the median to look for bias. We also measure the equivalent width of the (noiseless) fit from the LOSVD extraction, which matches the median from the Monte Carlo simulations well.

There does not appear to be any bias for most of these galaxies, i.e. the equivalent width of the observed spectrum is close to (within the uncertainty of) the median from the Monte Carlo simulations. For three galaxies, this is not the case. Messier 32, NGC 984, and NGC 2974 all have features in their spectra that cause a significant difference between the equivalent widths of the observed spectra and the fits (see Fig. 2.5 to see these differences). These features are likely due to variability in sky absorption which was not well-removed by our flattening procedure, combined with low S/N for NGC 984 and NGC 2974. (See later section on Messier

32 for more discussion.) For these galaxies, we choose to use the equivalent width of the fit, basically the same as the median from the Monte Carlo simulations, as our value for the equivalent width. We believe these values are more reliable than the values compromised by sky variability and noise issues.

These measurements of the equivalent width must be corrected for the effect of the galaxy dispersion. The velocity broadening throws equivalent width outside of our chosen measuring region, especially on the sharp blue edge. To calculate this correction, we take spectra for several types of stars, with equivalent widths ranging from about 7 Å to almost 20 Å, and convolve them with Gaussian velocity distributions of different dispersions. We then measure the equivalent widths of these convolved spectra in the same way we measure the galactic spectra in order to see how much we should correct our real equivalent width measurements. The dispersion correction for the CO bandhead agrees well between the different stars used, and we find this correction to be rather large, about 20% for 300 km s⁻¹. This is typical for some features used in optical regions (Trager et al. 1998). The correction we use, found by fitting a cubic polynomial to the data from the convolved stellar spectra, is

$$\frac{EW_{observed}}{EW_{actual}} = 1 - 1.853 \times 10^{-4} \sigma + 1.287 \times 10^{-6} \sigma^2 - 9.695 \times 10^{-9} \sigma^3$$

where $EW_{observed}/EW_{actual}$ is the ratio of observed and actual equivalent widths and σ is the velocity dispersion measured in km s⁻¹. Figure 2.8 illustrates this dispersion correction. The symbols show the fractional change in equivalent width for each star as a function of velocity dispersion, and the line shows the fit mentioned above used to correct our galaxy equivalent width measurements.

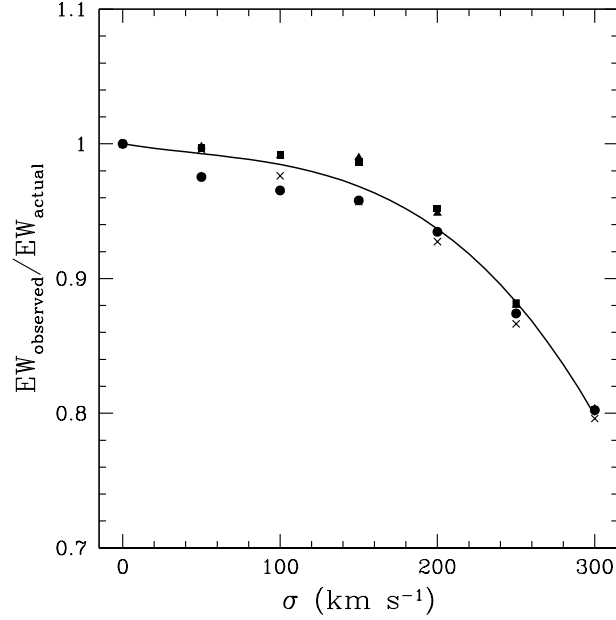


Figure 2.8: Dispersion correction to the equivalent width of the CO bandhead. The different symbols represent the change in measured equivalent width for stars with a range of equivalent widths convolved with Gaussian LOSVDs; the line is a fit to these data (described in the text) used to correct our galaxy equivalent width measurements.

2.3.3 Dust Masses

In order to ascertain the effects of dust on observed kinematics, we need to know how much dust there is in individual galaxies. In this section, we derive dust masses for our sample galaxies from IRAS flux densities according to the technique of Goudfrooij & de Jong (1995). The notation and equations below are identical to those presented in Goudfrooij & de Jong (1995). The 60 and 100 μm flux densities are sensitive mostly to emission from cool (i.e. interstellar) dust, but are contaminated by hot (i.e. circumstellar) dust. Goudfrooij & de Jong (1995) calculated this con-

tribution using data from Galactic Mira stars and found corrections to be

$$S(60)_{corr} = S(60) - 0.020S(12)$$

$$S(100)_{corr} = S(100) - 0.005S(12)$$

where $S(12)$ is the 12 μm IRAS flux density. These corrections are small for the sample galaxies.

The mass of dust M_d in a galaxy is

$$M_d = \frac{D^2 S_\nu}{\kappa_\nu B_\nu(T_d)}$$

where D is the distance to the galaxy, S_ν is the flux density, $B_\nu(T_d)$ is the Planck function for the dust temperature T_d at frequency ν , and κ_ν is the dust opacity

$$\kappa_\nu = \frac{4\pi a^2}{3\pi a^3 \rho_d} Q_\nu$$

where ρ_d is the specific dust grain mass density, a is the average grain radius weighted by grain volume, and Q_ν is the grain emissivity factor. Using the grain size distribution from Mathis et al. (1977) and the values of Q_ν from Hildebrand (1983), the dust mass in solar masses is

$$M_d = 5.1 \times 10^{-11} S_\nu D^2 \lambda^4 (\exp(1.44 \times 10^4 / \lambda T_d) - 1) M_\odot$$

where λ is in μm , D is in Mpc, and S_ν is in mJy.

We calculate the dust temperature as the color temperature determined from the corrected $S(100)/S(60)$ flux ratio using the assumption of a dust grain emissivity law $\propto \lambda^{-1}$, typical of astronomical silicates at wavelengths $\lambda < 200\mu\text{m}$ (Hildebrand

1983; Rowan-Robinson 1986; Mathis & Whiffen 1989):

$$\frac{S(60)}{S(100)} = \left(\frac{\nu_{60}}{\nu_{100}} \right)^4 \frac{\exp(h\nu_{100}/kT_d) - 1}{\exp(h\nu_{60}/kT_d) - 1}$$

where h is the Planck constant, k is the Boltzmann constant, and ν is the frequency in Hz. The temperatures calculated in this way should be regarded as estimates because a temperature distribution is surely more realistic than isothermal dust. Also, IRAS is sensitive to cool dust with $T_d > 25$ K, but it is predicted that much of the dust in a normal galaxy will be colder ($\simeq 10$ -20 K) and will emit more strongly at longer wavelengths. IRAS provides little information on this cold dust. Thus, the masses calculated from the IRAS color temperature are lower limits on the total dust mass in a galaxy and may be over an order of magnitude too low (Kwan & Xie 1992; Goudfrooij & de Jong 1995; Wiklind & Henkel 1995).

Table 2.2 lists the IRAS flux densities from Knapp et al. (1989) and the 1994 correction to those data, calculated dust temperature, and calculated dust mass for each galaxy in this sample. For galaxies which were not detected at both 60 and 100 μm , the dust temperature is assumed to be 30 K. For galaxies that are not detected in either band, the dust mass shown is an upper limit. As expected, the calculated dust temperatures lie between 25 and 50 K, the range of IRAS's greatest sensitivity. The galaxies in this sample have a wide range of dust masses, from no detectable mass to over a million solar masses. This is, of course, a tiny fraction of the total mass of a galaxy and does not affect the potential, but may significantly affect the observed kinematics.

2.4 Results and Discussion

Table 2.3 shows the dispersions measured from the CO bandhead and the optical dispersion measurements from the literature we use as comparisons. We are aware

of the difficulties in making such comparisons; optical stellar kinematic data can vary significantly between authors, especially in the dispersion. For each galaxy, we thoroughly investigate the published kinematic data and carefully choose the measurement which is the most reliable. We make these choices based on S/N ratio, LOSVD-fitting technique, and the concordance between recent published dispersions.

The homogeneous optical sample with the most galaxies in common with this study is that of Trager et al. (1998), a large reliable study of early-type galaxies. Trager et al. (1998) has measurements for 15 of our 25 galaxies. We have worked through the analysis in the following sections using only these galaxies and their dispersions from this paper; we find no significant changes in the results reported below. Our results do not appear to be dependent on author-to-author variations in published kinematics. The reader will notice in table 2.3 that we did not always choose to use the Trager et al. (1998) data when available. In some cases there are more recent measurements which appear to be better. These newer measurements are almost always consistent with Trager et al. (1998). The exception is NGC 3377. We use $145 \pm 7 \text{ km s}^{-1}$ from Kormendy et al. (1998), while Trager et al. (1998) quotes $126 \pm 2 \text{ km s}^{-1}$. We believe this discrepancy is due to the high rotation of NGC 3377, which Kormendy et al. (1998) includes but Trager et al. (1998) appears not to have included.

There are three galaxies in our sample which have particularly unreliable optical measurements. These are galaxies which have especially large differences between reliable published optical dispersions, or which have only very old dispersion measurements. These galaxies are NGC 4150, NGC 5195, and NGC 6548. We repeated the analysis in the following sections without these galaxies in the sample, and again find no significant changes in our results.

For each galaxy, we choose an integrated optical dispersion measured with

a similar extraction window to our measurement. However, the integrated dispersion as a function of extraction window does not vary significantly (Gebhardt et al. 2000b). Thus, any errors made due to uncertainty in the extraction window comparison will be minimal. For example, NGC 3998, which has steeply rising kinematic profiles, shows no variation in the derived velocity dispersion when we use different extraction windows. For optical dispersions without quoted uncertainties, we assume 5% of the measured value. Also, for galaxies with quoted uncertainties less than 5%, we substitute 5% of the measured value, assuming that problems with template mismatch, continuum subtraction, etc. introduce uncertainty of at least that magnitude into the optical uncertainties.

2.4.1 Comparing IR and Optical Dispersions

Figure 2.9 shows the correlation between the CO dispersions and the optical dispersions. The most obvious aspect of this comparison is that most of the CO measurements are lower than the optical dispersions. The dashed line has a slope of unity, showing where the two measurements are equal, and the solid line is a fit by least squares to the data. The slope of the best fit line is 1.189 ± 0.084 , which is a significant difference from unity at a 2.25σ level. The intercept of the best fit line is -8.6 ± 12.4 , not significantly different from zero. The χ^2 of this best fit is 54.4. If we assume that there should be a correlation between the dispersions, then the 24 constraints imply that we have underestimated our uncertainties. To have a χ^2 value of 24 (matching the 24 constraints), all the errors need to be scaled up by 50%. The χ^2 of the dashed line in the plot (i.e. equality between optical and IR dispersions) is 76.2, a markedly worse fit. Increasing our uncertainties by 50% is unrealistic and the large scatter is likely real, possibly reflecting random dust distribution between galaxies.

The true ellipticals are represented in Figure 2.9 as open triangles while the

S0s are filled circles. Our sample does not contain many true Es (because of the make-up of the SBF sample at these redshifts) so it is difficult to make definitive statements, but we examine the differences between the two populations. The true ellipticals appear to be more consistent between the infrared and optical data. The slope of the best fit line to only the ellipticals is 0.994 ± 0.091 , consistent with unity, and the intercept is 4.8 ± 13.4 , consistent with zero. The χ^2 of this best fit is 1.77, which is at least consistent with the seven constraints.

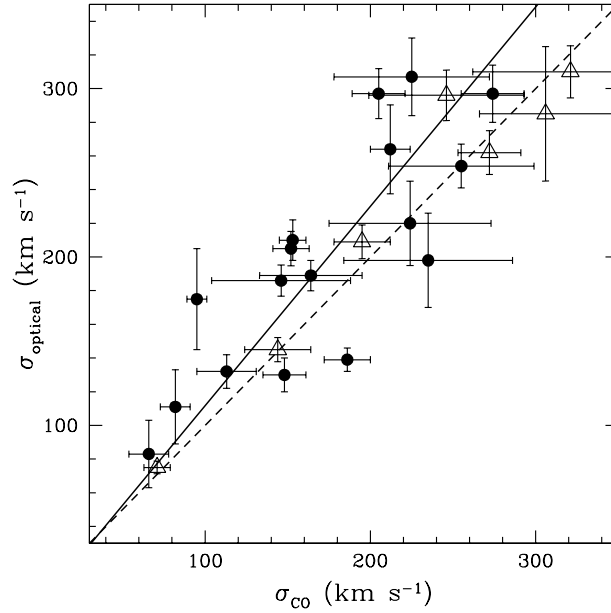


Figure 2.9: Correlation between the dispersion measured from the CO bandhead and the optical dispersion from the literature. The dashed line has a slope of unity, showing where the two measurements are equal. The solid line is the best fit to the data, as described in the text. Here and in following plots, the filled circles are S0 galaxies while the open triangles are true Es.

Figure 2.10 shows the distribution of galaxies in bins of fractional difference between the infrared and optical measurements. The dispersions measured with the CO bandhead are as much as 30% and 40% lower than their optical counterpart

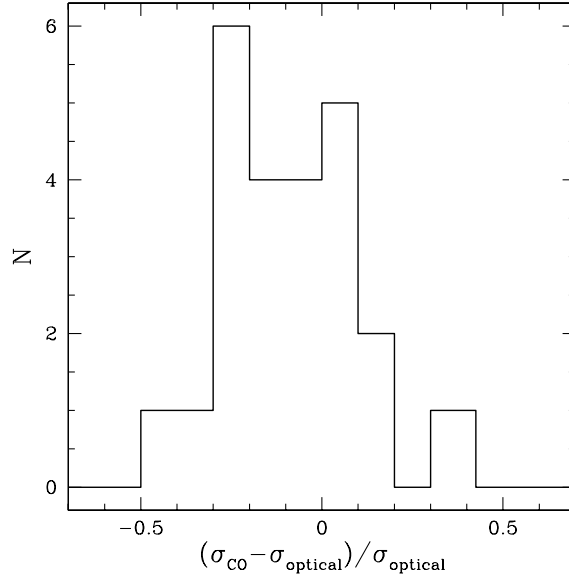


Figure 2.10: Histogram showing the number of galaxies in each bin of fractional difference between infrared and optical measurements of dispersion. The median difference is 11% smaller.

measurements, with the median difference being 11% lower. This is in the opposite sense to the predictions of Baes & Dejonghe (2002). Those authors’s models show that dust decreases the velocity dispersion in central regions for radial and isotropic galaxies. Only for their tangential orbital structures does dust increase the central dispersion, but early-type galaxies are not usually thought to be dominated by tangential orbits. Also, the magnitude of this effect seems to be larger than predicted by Baes & Dejonghe (2002). They predict an effect of a few percent for modest amounts of dust, and these results show an effect of up to 30% for many galaxies. Baes & Dejonghe (2002) do find an effect similar to these results (a significant decrease in the velocity dispersion) due to dust scattering, but only at several effective radii.

2.4.2 Dust, Equivalent Widths, and Template Make-up

In Figure 2.11, we examine the relationship between the fractional difference between the two measurements of the dispersion and the dust mass calculated from IRAS flux densities. If it is dust which is causing the difference between the infrared and optical dispersions, then surely it is the relative amount of dust in a galaxy, not the absolute amount, which is important. To examine this, we plot the fractional difference versus the ratio of IRAS dust mass to B -band total luminosity, as quoted in RC3. This gives a rough estimate of the relative importance of dust for each galaxy. Using a K -band magnitude would be better here because dust attenuation affects the B band strongly, but some of the galaxies in our sample do not have near-IR photometric measurements in the same filter system, or even at all.

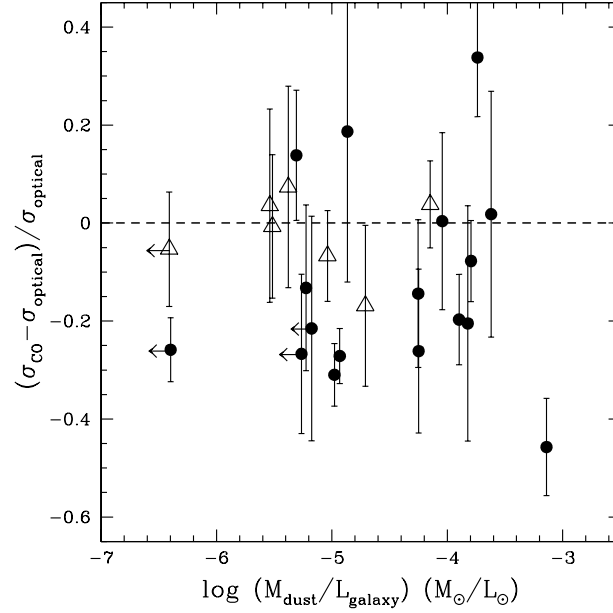


Figure 2.11: Fractional difference between infrared and optical dispersions as a function of the ratio of dust mass to B -band luminosity. The arrows indicate upper limits on the dust mass-to-light. The dashed line represents equality between the infrared and optical measurements.

We calculate the Spearman rank-order correlation coefficient (r_s) and the probability (P_{r_s}) to examine any statistical correlation here. $P_{r_s} = 1$ indicates that the data are completely uncorrelated, while $P_{r_s} = 0$ indicates complete correlation; the sign of r_s indicates correlation or anticorrelation. For the whole sample, $P_{r_s} = 0.985$ and $r_s = -0.0045$; for the sample minus the four galaxies for which the dust mass is an upper limit, $P_{r_s} = 0.369$ and $r_s = -0.212$. These results imply that the dust mass-to-light ratio and the fractional difference are not likely to be correlated. There is a slight hint of an anticorrelation in the sample minus the excluded galaxies, but the evidence is not strong. The dust may be important in these differences, but there must be other effects at work besides the relative amount of dust in a galaxy. According to the models described earlier, the effect of dust depends on the orbital structure, which could vary for the galaxies in this sample. The radial dust distribution also will change these effects and may be important in these fractional differences.

In addition, stellar population differences between the two wavelength regimes could cause such an effect. If the $V - K$ colors of the galaxies were bluer toward their centers, the K -band light would sample less central, lower-velocity regions of the galaxy and the K -band dispersion would be lower, as found here. To test this, we are measuring K -band surface photometry of these galaxies using the recently available data of the *Two Micron All Sky Survey* (*2MASS*). This surface photometry has already been obtained for one galaxy in our sample, which has good agreement between its infrared and optical dispersions: M32. Peletier (1993) reports surface photometry for several optical and infrared colors and finds that M32's profile is practically flat in all colors, including the optical-infrared colors. This is consistent with negligible dust and matching optical and infrared kinematics, but does not help us understand the systematic differences between optical and infrared dispersions. Early-type galaxies are redder in their centers in optical colors, which, if also true

in optical-infrared colors, would result in a change in dispersion opposite to what we find.

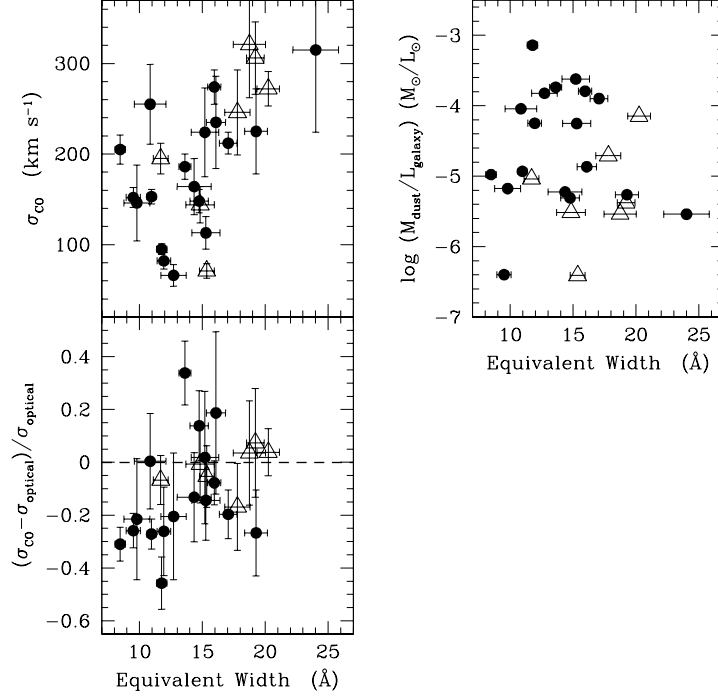


Figure 2.12: Properties of the sample galaxies as they relate to the measured CO bandhead equivalent width. Shown are the relationships between equivalent width and CO bandhead dispersion, IRAS dust mass, and fractional difference between infrared and optical dispersions.

We can examine the relationship between equivalent width and these quantities. Table 2.3 shows the measured equivalent widths for the sample galaxies. In stars, the CO bandhead equivalent width increases from warmer, younger stars to cooler, older stars, with a typical early K giant having an equivalent width on the order of $\sim 10 \text{ Å}$ (Kleinmann & Hall 1986; Förster Schreiber 2000). Figure 2.12 shows the distribution of equivalent widths for this sample and how the sample properties depend on this quantity. The measured CO bandhead dispersion seems

to be correlated with equivalent width, which is reasonable considering other known metallicity-dispersion relations. The probability $P_{r_s} = 0.036$ indicates a high probability of a correlation ($r_s = 0.438$). In addition, there appears to be correlation between the measured equivalent width of the galaxy and the fractional difference between the two dispersion measurements. For these quantities, $P_{r_s} = 0.054$ and $r_s = 0.436$.

Also interesting is the distribution of equivalent widths of the galaxies. Almost all of the galaxies have equivalent widths over 10 Å, to over 20 Å. K giants have equivalent widths between 10 and 15 Å, and the only stars with equivalent widths higher than about 15 Å are M giants and K and M supergiants. The stellar population in the infrared must have a large fraction of very cool stars to match the measured equivalent widths. According to these data, the light at these wavelengths is largely dominated by M stars (probably giants). This was suggested by Rieke & Lebofsky (1979) decades ago based on near-IR photometric measurements, and provides important information about where the light is coming from at these wavelengths. By number, the effect is not as extreme. A typical M star (dwarf, giant, or supergiant) is 6 or 7 times brighter than its K star counterpart in the K band, so while finding the light dominated by M giants does imply that there is a significant population there, there is still room for other stellar types. This information must be taken into account when measuring kinematics in the near-infrared. Previous work has often used K giants for stellar templates, which easily could be the wrong choice and will effect the derived kinematics in a template-sensitive feature like the CO bandhead.

We also have information about the relative weights given to the different template stars by the fitting program. The LOSVD fitting is free to choose from eight different template stars to achieve the best fit. The different galaxies usually use only two or three of these stars. Figure 2.13 shows how these weights are related

to other galaxy characteristics. We quantify the make-up of the average stellar template chosen by the fitting program by the fraction of the weight given to low equivalent width (low-EW) stars. These are the template stars with an equivalent width below 10 Å; moderate changes in the choice of cut-off do not affect the results. The galaxies in our sample vary from giving all the weight to low-EW stars to using none of these stars. The correlation between the equivalent width of the galaxy and the weight given to templates of a certain equivalent width (upper right-hand quadrant) is expected; galaxies with high equivalent widths require templates of high equivalent width to achieve a good fit. The apparent correlation between the fractional difference between optical and IR dispersions and the fraction of low-EW templates used (upper left-hand quadrant) is just that expected from the previously mentioned correlation and the relationship between galaxy equivalent width and dispersion differences.

Different spectral indices have been used to study the chemical history of galaxies. The Mg₂ index is perhaps the most widely studied for this purpose; it is a measurement of the flux deficit in the lines compared to the neighboring continuum. Comparing this index with our infrared data may give us useful information on these aspects of galaxies. Twenty of the galaxies in our sample have Mg₂ indices in the compilation of Golev & Prugniel (1998) and the updates to that compilation available on HYPERCAT (<http://www-obs.univ-lyon1.fr/hypercat/>). This catalog of published absorption-line Mg₂ indices has been zero-point corrected and transformed to a homogeneous system. This facilitates comparison between different authors' measurements. We used measurements from Trager et al. (1998) when available; table 2.3 shows the Mg₂ indices used and their sources in the literature. The actual values are taken from HYPERCAT where they have been transformed to a standard system. Figure 2.14 illustrates the relationships between the Mg₂ index and the CO bandhead equivalent width, our velocity dispersion measurement,

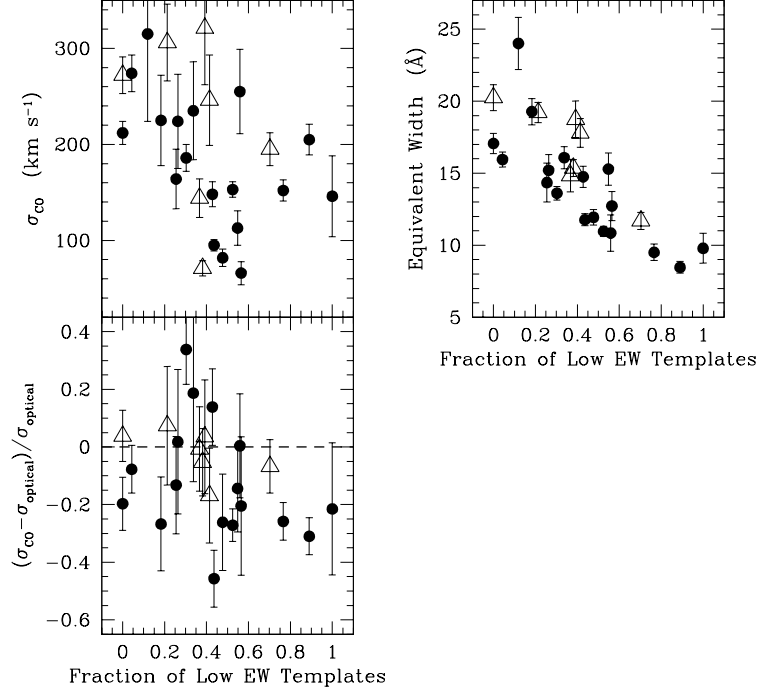


Figure 2.13: Same as Fig. 2.12, but for the fractional weight given to low equivalent width templates.

and the fractional difference between the optical and infrared dispersions. The Mg₂ index appears to be tightly correlated with velocity dispersion ($P_{r_s} = 0.105$, $r_s = 0.383$); this is the familiar and well-studied Mg- σ relation. Further investigation into the scatter, slope, etc. of this relation using infrared velocity dispersion measurements (rather than optical, as is currently done) may reveal important information about this scaling relation. The CO bandhead equivalent width is not very likely correlated with the Mg₂ index ($P_{r_s} = 0.290$, $r_s = -0.249$). This is perhaps surprising because both the CO equivalent width and the Mg₂ index appear to be significantly correlated with the velocity dispersion, which could cause them to be correlated with each other. We do not see such a relationship, which could be due to our small

sample size.

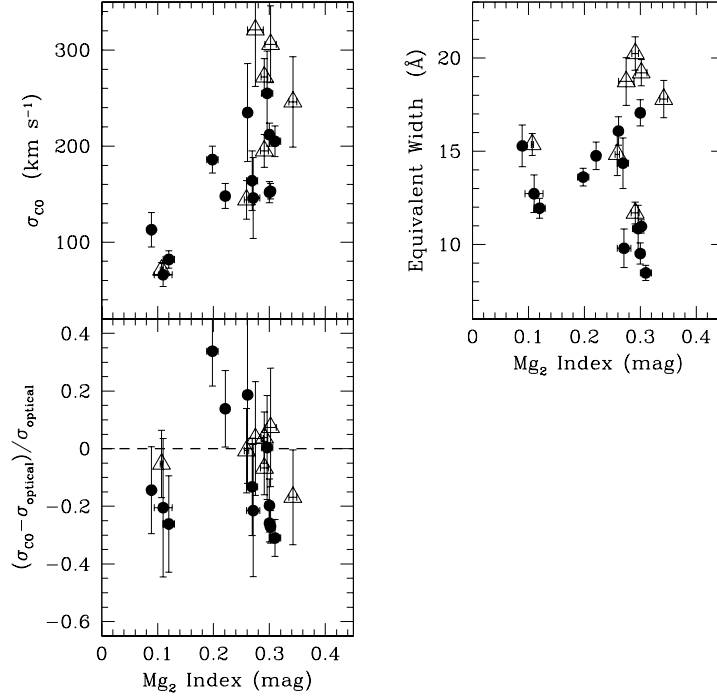


Figure 2.14: Properties of the sample galaxies as they relate to the Mg_2 index (from the literature). Shown are the Mg_2 index versus CO bandhead dispersion, CO bandhead equivalent width, and fractional difference between infrared and optical dispersions.

2.4.3 Messier 32

Messier 32 (NGC 221) is an important galaxy which is part of this sample. It is the compact elliptical companion of the Andromeda Galaxy here in the Local Group, and is extremely well-studied. It was not detected by IRAS and has an upper limit on the dust mass of less than $100 M_{\odot}$. Thus, it should be an excellent candidate for calibrating this technique and exploring the case of minimal dust. It is important to keep in mind, however, that in the infrared we are looking at what may be a different

stellar population with perhaps different kinematic properties. For example, if the infrared population is more centrally concentrated relative to the whole potential than the optical population, the infrared dispersion would be higher than the optical dispersion because it samples more central, higher-velocity stars.

Unfortunately, there has been some observational difficulty with this galaxy. It is at nearly zero redshift ($cz = -145 \text{ km s}^{-1}$) and thus the CO bandhead falls exactly in a region of troublesome variability in atmospheric absorption. This feature was not well removed by the flattening process described above. The main reason is that NGC 221 is far brighter than any other galaxy in this sample, and thus its total integration time was less than 30 minutes. Such a short integration time made this galaxy vulnerable to problems with sky fluctuations. The other galaxies in the sample required longer exposure times which allowed these sky fluctuations to average out. Also, this particular atmospheric feature is not a problem for galaxies with any considerable redshift, as the feature is moved away from this region. The problem area is visible in Figure 2.5; it is the “bump” between 2.296 and $2.298 \mu\text{m}$. This region was ignored during the LOSVD fitting (a happy benefit of fitting the LOSVD directly in pixel space) and is located on the red edge (rather than the sharp blue edge which dominates the fit) but it does make it worrisome to make strong statements based on the results for this galaxy. Despite these observational difficulties, we measure a velocity dispersion of $71 \pm 8 \text{ km s}^{-1}$, which is very close to the value of 75 km s^{-1} from van der Marel et al. (1994). For the equivalent width of this galaxy, we choose to use the equivalent width of the fit made by the LOSVD extraction rather than of the observed spectrum, as explained in a previous section. This removes the rather large effect ($\sim 20\%$) of the sky feature from the equivalent width measurement.

2.5 Conclusions

In this project, we have observed 25 nearby early-type galaxies and measured their stellar kinematics using the $2.29\mu\text{m}$ (2-0) ^{12}CO absorption bandhead. We compare the infrared velocity dispersions of these galaxies to optical dispersions from the literature and find that the IR dispersions are generally shifted to lower values relative to the optical dispersions, between 5 and 30% for most galaxies. However, this effect is mainly driven by the S0 galaxies; pure ellipticals tend to have nearly zero offset, on average. If dust in S0 galaxies exists mainly in a disk which is cospatial with the stellar disk, optical dispersions will be biased against measuring light from this cold component and hence will come from the hot bulge component. This may explain the effect we see, since we find lower CO dispersions for lenticular galaxies, but it is currently unclear how dust is distributed in galaxies. We do see some evidence for dust disks in S0 galaxies. For example, NGC 2787, which has a 20% offset between its optical and near-IR dispersions, has a dramatic dust disk in the central regions visible in HST imaging (Erwin & Sparke 2003). The differences may be due to other dust features, however. For instance, NGC 5195, the strongest outlier in this sample with a 45% offset between its optical and near-IR dispersions, has a significant amount of clumpy dust visible in HST imaging available from the online HST archive; the clumpy distribution of dust may be the cause of the offset. However, NGC 3998, a galaxy with a 30% offset between the two measures of the dispersion, shows no signs of clumpy dust or a dust disk. More data is needed on the dust content and distribution of galaxies to fully understand these issues.

We have calculated the dust masses implied by IRAS flux densities for these galaxies and examined the relationship between the differences in optical versus infrared dispersions and the amount of dust in a galaxy. We do not find a strong relationship, but dust may still be an important contributor to these differences. Both the amount and distribution of the dust can affect any differences in the

mean dispersion. We have also calculated the equivalent width of this feature and compared it to other galaxy properties. The equivalent widths of the galaxies are quite high, indicating that the light is dominated by very cool (i.e. M) stars.

Table 2.1: Basic properties of sample galaxies

Galaxy	Type	v (km s ⁻¹)	$(m - M)$	D (Mpc)	M_B (mag)
NGC 0221	cE2	-145	24.55	0.813	-15.52
NGC 0315	E (LINER)	4942	—	70.600	-22.04
NGC 0821	E6	1735	31.91	24.099	-20.24
NGC 0984	S0	4352	—	62.171	-20.17
NGC 1023	S0	637	30.29	11.429	-19.94
NGC 1161	S0	1954	—	27.914	-20.18
NGC 1400	S0	558	32.11	26.424	-20.19
NGC 1407	E0	1779	32.30	28.840	-21.59
NGC 2110	S0 (Sy2)	2335	—	33.357	-18.62
NGC 2293	S0 pec	2037	31.16	17.061	-18.88
NGC 2380	S0	1782	32.05	25.704	-19.78
NGC 2681	S0/a	692	31.18	17.219	-20.09
NGC 2768	S0	1373	31.75	22.387	-20.91
NGC 2787	S0 (LINER)	696	29.37	7.482	-17.55
NGC 2974	E4	2072	31.66	21.478	-19.79
NGC 3377	E5-6	665	30.25	11.220	-19.01
NGC 3998	S0 (Sy1)	1040	30.75	14.125	-19.14
NGC 4150	S0	226	30.69	13.740	-18.25
NGC 5195	S0 pec (LINER)	465	29.42	7.656	-18.97
NGC 5866	S0 (LINER)	672	30.93	15.346	-20.19
NGC 6548	S0	2174	31.81	23.014	-19.08
NGC 6703	S0	2461	32.13	26.669	-19.81
NGC 7332	S0 pec	1172	31.81	23.014	-19.79
NGC 7619	E	3762	33.62	52.966	-21.52
NGC 7743	S0+ (Sy2)	1710	31.58	20.701	-19.20

Table 2.2: IRAS fluxes and dust characteristics of sample galaxies

Galaxy	$S(60)$ (mJy)	$S(100)$ (mJy)	T_d (K)	$\log M_d$ (M_\odot)	$\log (M_d/L_{galaxy})$ (M_\odot/L_\odot)
NGC 0221	<85	<1412	–	<1.99	<-6.41
NGC 0315	310	400	42.3	5.47	-5.54
NGC 0821	<41	500	–	5.25	-5.04
NGC 0984	140	140	48.0	4.72	-5.54
NGC 1023	<32	<75	–	<3.77	<-6.40
NGC 1161	1945	<9358	–	6.47	-3.79
NGC 1400	740	3280	27.2	6.37	-3.90
NGC 1407	140	480	29.2	5.45	-5.38
NGC 2110	4129	5676	41.1	6.02	-3.62
NGC 2293	380	2810	–	5.70	-4.04
NGC 2380	60	<388	–	4.88	-5.22
NGC 2681	6186	11770	35.9	5.98	-4.25
NGC 2768	390	1370	29.1	5.69	-4.87
NGC 2787	600	1180	35.5	4.28	-4.93
NGC 2974	420	1900	27.0	5.96	-4.15
NGC 3377	140	350	32.4	4.28	-5.52
NGC 3998	550	1150	34.6	4.87	-4.98
NGC 4150	1220	2670	34.1	5.24	-4.25
NGC 5195	38010	<511	–	6.64	-3.14
NGC 5866	5070	18680	28.7	6.53	-3.74
NGC 6548	<35	<119	–	<4.56	<-5.26
NGC 6703	<66	<200	–	<4.94	<-5.18
NGC 7332	210	410	35.5	4.80	-5.31
NGC 7619	<37	710	–	6.09	-4.71
NGC 7743	920	3400	28.7	6.05	-3.82

Table 2.3: Derived quantities from observed spectra and properties gathered from the literature

Galaxy	Total Exposure Time (minutes)	S/N (pixel ⁻¹)	Extraction Window	Equivalent Width (Å)	σ_{co} (km s ⁻¹)	$\sigma_{optical}$ (km s ⁻¹)	Mg ₂ Index (mag)
NGC 0221	24	27	1.8'' × 14.0''	15.4 ± 0.59	71 ± 8	75 ± 4 ^a	0.107 ± 0.002 ^b
NGC 0315	160	13	1.8'' × 15.4''	18.7 ± 1.3	321 ± 59	310 ± 16 ^b	0.275 ± 0.014 ^b
NGC 0821	96	30	1.8'' × 11.9''	11.7 ± 0.58	195 ± 17	209 ± 10 ^c	0.291 ± 0.007 ^b
NGC 0984	168	8	1.8'' × 14.7''	24.0 ± 1.8	315 ± 91	–	–
NGC 1023	48	28	1.8'' × 17.5''	9.5 ± 0.57	152 ± 11	205 ± 10 ^d	0.340 ± 0.005 ^b
NGC 1161	72	32	1.8'' × 14.0''	15.9 ± 0.52	274 ± 19	297 ± 17 ^e	–
NGC 1400	40	26	1.8'' × 10.5''	17.1 ± 0.70	212 ± 12	264 ± 26 ^b	0.300 ± 0.007 ^b
NGC 1407	240	29	1.8'' × 17.5''	19.2 ± 0.70	306 ± 40	285 ± 40 ^b	0.302 ± 0.010 ^b
NGC 2110	120	12	1.8'' × 12.6''	15.2 ± 1.1	224 ± 49	220 ± 25 ^f	–
NGC 2293	120	14	1.8'' × 14.0''	10.8 ± 1.3	255 ± 44	254 ± 13 ^g	0.296 ± 0.010 ^m
NGC 2380	96	18	1.8'' × 10.5''	14.4 ± 1.4	164 ± 31	189 ± 9 ^h	0.269 ± 0.010 ^m
NGC 2681	120	31	1.8'' × 17.5''	11.9 ± 0.54	82 ± 9	111 ± 22 ^b	0.120 ± 0.010 ⁿ
NGC 2768	120	7	1.8'' × 11.2''	16.0 ± 0.77	235 ± 51	198 ± 28 ^b	0.261 ± 0.006 ^b
NGC 2787	72	48	1.8'' × 17.5''	11.0 ± 0.35	153 ± 8	210 ± 12 ^b	0.302 ± 0.007 ^b
NGC 2974	144	21	1.8'' × 14.0''	20.2 ± 0.89	272 ± 19	262 ± 13 ^g	0.291 ± 0.006 ^b
NGC 3377	166	10	1.8'' × 10.5''	14.8 ± 1.1	144 ± 20	145 ± 7 ⁱ	0.259 ± 0.004 ^b
NGC 3998	72	39	1.8'' × 10.5''	8.5 ± 0.41	205 ± 16	297 ± 15 ^j	0.310 ± 0.010 ^o
NGC 4150	72	8	1.8'' × 7.0''	15.3 ± 1.1	113 ± 18	132 ± 10 ^k	0.089 ± 0.005 ^b
NGC 5195	72	35	1.8'' × 7.0''	11.8 ± 0.42	95 ± 6	175 ± 30 ^l	–
NGC 5866	128	40	1.8'' × 14.0''	13.6 ± 0.47	186 ± 14	139 ± 7 ^j	0.198 ± 0.010 ^o
NGC 6548	296	13	1.8'' × 6.3''	19.3 ± 0.91	225 ± 47	307 ± 23 ^e	–
NGC 6703	208	7	1.8'' × 9.1''	9.8 ± 1.0	146 ± 42	186 ± 9 ^j	0.271 ± 0.012 ^b
NGC 7332	96	18	1.8'' × 6.3''	17.8 ± 0.73	148 ± 13	130 ± 10 ^b	0.221 ± 0.007 ^b
NGC 7619	96	12	1.8'' × 14.0''	17.8 ± 1.0	246 ± 47	296 ± 15 ^g	0.342 ± 0.007 ^b
NGC 7743	120	18	1.8'' × 4.2''	12.7 ± 1.0	66 ± 12	83 ± 20 ^f	0.110 ± 0.016 ^p

References: (a) van der Marel et al. (1994); (b) Trager et al. (1998); (c) Gebhardt et al. (2003); (d) Bower et al. (2001); (e) Tonry & Davis (1981); (f) Nelson & Whittle (1995); (g) Jorgensen et al. (1995); (h) Davies et al. (1987); (i) Kormendy et al. (1998); (j) Fisher (1997); (k) di Nella et al. (1995); (l) White et al. (1983); (m) Faber et al. (1989); (n) Burstein et al. (1988); (o) Fisher et al. (1996); (p) Huchra et al. (1996)

Chapter 3

An All-Infrared Fundamental Plane of Early-Type Galaxies

3.1 Moving the Fundamental Plane Redward

Mass growth history of galaxies is one of the most important issues being addressed in extragalactic astronomy today. We want to know how galaxies form and/or grow their components such as a bulge, disk, black hole, dark matter halo, etc. Pure bulge galaxies (i.e. ellipticals) may or may not form differently from the bulges of disk galaxies, and the relative importance of violent merging versus slow secular evolution is unclear. Crucial tools we use to explore such questions are the scaling relations in local galaxies. Galaxies exhibit relationships among their different measured properties, early-type galaxies having the tightest relationships. In the three-dimensional space made up of effective radius (or total luminosity), mean surface brightness, and velocity dispersion, early-type galaxies inhabit a two-dimensional surface, the Fundamental Plane (FP) (Djorgovski & Davis 1987; Dressler et al. 1987). The FP provides important clues and constraints for how galaxies form and evolve (i.e. evolution of FP with redshift, galaxy type, etc.). However, its current incarnations

based on visible-wavelength data may suffer from problems of bias and/or internal extinction due to dust. We have constructed an all-infrared FP using both *K*-band photometry and kinematics which addresses these problems and widens the galaxy parameter space within which the FP is a useful tool.

A relationship among the quantities of the FP is predicted by the virial theorem, but the observed FP has coefficients which are significantly different from simple virial predictions. The tilt of the FP varies with the observational passband, generally increasing as one moves to redder bands (Bernardi et al. 2003a). The detailed shape of the FP in different passbands can differentiate between the relative importance of different effects in galaxy evolution. Also, although the FP has been largely used to study pure bulge galaxies, the bulges of disk galaxies lend themselves to such an analysis. The change (or lack thereof) in the FP with galaxy type can hold important information on the histories and formation mechanisms for galaxies of different morphologies. Previous studies of the FP of bulges (Bender et al. 1992; Falc3n-Barroso et al. 2002) prove that it is more difficult and less reliable than for elliptical galaxies. The more complicated structure of disk galaxies and the important effects of dust present problems for such analysis.

Moving to the infrared for both kinematics and photometry holds promise in addressing important concerns with the FP. Observing in the near infrared traces the older, redder stellar population whose kinematics are a more accurate reflection of the actual potential of the galaxy. Effects from recent star formation are lessened. Also, near-infrared wavelengths are long enough to minimize extinction from dust. *K*-band observations allow us to look through the dust to a large extent and observe the unobscured starlight. It is argued that dust may be important even in early-type galaxies, assumed to be largely free of dust (Knapp et al. 1989; Wiklind & Henkel 1995; Kwan & Xie 1992; Goudfrooij & de Jong 1995). Furthermore, this dust may have a significant effect on both the observed structure and kinematics of these

galaxies (Baes & Dejonghe 2000; Baes et al. 2000; Baes & Dejonghe 2001, 2002). It is known that IR photometry and morphology are different than in the optical (Pahre et al. 1998; Jarrett et al. 2003), but galaxy kinematics may be dust-affected as well (Silge & Gebhardt 2003).

Distributed dust may be a concern for current kinematic studies, but perhaps more important is the issue of selection bias. Galaxies which are difficult to observe are often not included in kinematic studies. For instance, it is difficult to observe optical spectra of galaxies with dust patches and lanes. There are a significant number of galaxies for which the existing kinematic data is considered unreliable because of visible dust. Such galaxies are often not included in kinematic studies, introducing bias into current kinematic samples. This concern does apply to some ellipticals, many of which contain dust lanes and features (Kormendy & Djorgovski 1989; Lauer et al. 1995; van Dokkum & Franx 1995; Rest et al. 2001; Tran et al. 2001), but is even more significant with later-type galaxies which contain large amounts of dust.

In this paper, we have combined new stellar kinematic measurements with 2MASS photometry to build the first all-infrared FP. We present work on a sample of early-type galaxies (E and S0) to calibrate the infrared FP and to address the issues raised above for a sample made up of the kind of galaxies traditionally used in FP studies. We can also use these techniques to study the bulges of later-type galaxies. We can expand the parameter space within which galaxies are well-studied and address issues critical for galaxy evolution. This paper is organized as follows: Section 2 presents the data, Section 3 discusses the FP for these galaxies, Section 4 presents our discussion of these results.

3.2 Data

3.2.1 Sample

Table 3.1 includes the 35 galaxies in this paper. The sample is made up of ellipticals and lenticulars chosen from the surface brightness fluctuation study of Tonry et al. (2001). Tonry et al. (2001) present distance moduli for 300 nearby galaxies from surface brightness fluctuations. This presents an ideal sample to draw from for this study; these galaxies are systems with bulges (mostly E and S0, with some S) and have well-determined distances, necessary for the FP analysis. The galaxy type and heliocentric velocity (from NED), distance modulus (from Tonry et al. 2001), calculated distance, and the absolute K magnitude (calculated using the total apparent K magnitude from the 2MASS XSC) are listed in Table 3.1. For NGC 315, which is not in Tonry et al. (2001), the distance is calculated assuming Hubble flow, with $H_0 = 70 \text{ km s}^{-1} \text{ Mpc}^{-1}$. NGC 4467, an M32 analog in the Virgo cluster, is assumed to be at the distance to Virgo, $D = 16.5 \text{ Mpc}$. We also include NGC 5128 (Centaurus A), which is assumed to be at 3.5 Mpc Israel (1998); Rejkuba (2004). Since beginning this near-infrared kinematic study in December 2000, we have obtained spectra for over 80 galaxies. Thirty-three of these galaxies are early-type (E or S0) and make up the sample presented here.

3.2.2 2MASS Photometric Quantities

To construct the FP, we need photometric measurements (effective or half-light radius r_{eff} and mean surface brightness within the effective radius I_{eff}) as well as kinematic measurements (velocity dispersion σ). The Two Micron All Sky Survey (2MASS) has imaged the entire sky in the J , H , and K bands and makes this data publicly available through the Infrared Science Archive (Cutri et al. 2003). This is an excellent resource, proffering a large, homogeneous, accessible imaging dataset.

The sensitivity and angular resolution of 2MASS are more than adequate to study the nearby galaxies in our sample. We choose to utilize the K -band images since this light is the best tracer of the old stellar population and is most reflective of the potential of the galaxy.

For the elliptical galaxies, we utilize the Extended Source Catalog (Jarrett et al. 2000), which contains 1.65 million galaxies and Galactic extended sources, to measure r_{eff} and I_{eff} . The XSC reports the half-light, or de Vaucouleurs “effective”, radius for each entry, as well as the total K -band magnitude. The FWHM seeing varied between $2.5''$ and $3''$, good enough to measure the effective radii of these nearby galaxies. Table 3.3 includes the effective radius in arcseconds, the effective radius in kiloparsecs calculated using the distance modulus from Tonry et al. (2001), and the effective surface brightness (calculated using m_K and r_{eff} from the XSC). The XSC does not report uncertainties for the effective radius or surface brightness, so in our FP fitting procedure we assume the uncertainties are 5% of the values. In any case, uncertainties in these quantities due to various photometric fitting procedures have little effect on the FP. Kelson et al. (2000) find that differences cause galaxies to move along the plane, not away from the plane, and thus cannot change the coefficients of the FP. We checked the XSC quantities by fitting deVaucouleurs profiles to 2MASS images for several of the elliptical galaxies and find good agreement.

For the lenticular galaxies, we perform a bulge/disk decomposition on the 2MASS images to find r_{eff} and I_{eff} for the bulge component. Neglecting such a step would bias our results for the photometric quantities for these galaxies, attributing light to the bulge which properly belongs to the disk. We utilize images from the 2MASS Large Galaxy Atlas (LGA) (Jarrett et al. 2003) when available. These authors construct large mosaics for each of the 100 largest galaxies as seen in the near-infrared. Jarrett et al. (2003) join 2MASS scans and iteratively remove the

sky background, resulting in carefully constructed, well-calibrated images of these galaxies. For galaxies not included in the LGA, we use the regular 2MASS Atlas image. Of the fifteen S0 galaxies in our sample, seven are in the LGA. We have compared the results of our photometric fitting using both LGA and Atlas images; we do not find significant differences although the LGA images are easier to use and better calibrated. We use the multi-Gaussian expansion (MGE) method of Cappellari (2002) to fit the surface brightness profile to the 2MASS image. The MGE method is a simple parametrization flexible enough to model realistic multicomponent objects. This method uses a series expansion of two-dimensional Gaussian functions to represent galaxy images. For most of the galaxies, we obtain a good fit by holding the position angle constant, but five galaxies (NGC 1023, NGC 2768, NGC 2787, NGC 5195, and NGC 6548) required varying the position angle to obtain a good fit.

We fit

$$I(r) = I_b \exp \left[-b_n \left(\left(\frac{r}{r_{eff}} \right)^{1/n} - 1 \right) \right] + I_d \exp \left(-\frac{r}{r_d} \right)$$

to the galaxy images using the two-dimensional fitting algorithm GALFIT (Peng et al. 2002). The first term represents the bulge with a Sérsic function, where I_b is the central bulge intensity, r_{eff} is the effective (or half-light) radius, n determines the variation with radius ($n = 1$ for an exponential disk, $n = 4$ for a deVaucouleurs profile), and $b_n \sim 2n - 0.324$. We fit both a Sérsic profile ($r^{1/n}$) and a deVaucouleurs profile ($r^{1/4}$). For some galaxies, the Sérsic index n is not well-determined; this quantity is quite sensitive to the background sky. Changes in n can affect the measured r_{eff} but also affect the measured I_b in such a way that galaxies move along the FP, not away from it, again as indicated by Kelson et al. (2000). We use the Sérsic profile when it is well-determined and the deVaucouleurs profile for the other cases; the uncertainty in the actual value for n does not affect our FP

results. The second term represents the disk with an exponential profile, where I_d is the central disk intensity and r_d is the disk scale length. Table 3.2 presents the results for the bulge/disk decomposition for the 15 lenticular galaxies in the sample, and figures 3.1 through 3.4 illustrate these fits. Each panel presents the data for one galaxy: the major axis surface brightness profile extracted from the image using the MGE method (points with error bars) along with the fitted profiles from GALFIT and the ellipticity profile. In the surface brightness profile plots, the dotted line shows the bulge component, the dashed line shows the disk component, and the heavy solid line shows the combined fitted surface brightness profile.

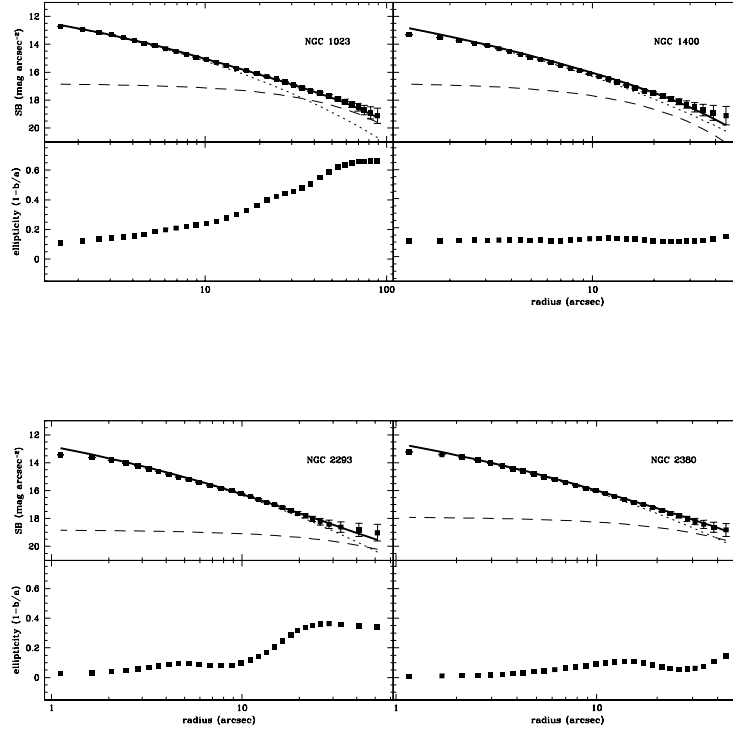


Figure 3.1: Surface brightness profile and bulge/disk decomposition information for each SO galaxy. For each galaxy, the top panel presents the surface brightness profile and the bottom panel shows the ellipticity profile. In the surface brightness profile panels, the points with error bars show the major axis surface brightness profile extracted from the image using the MGE method, the dotted line shows the bulge component, the dashed line shows the disk component, and the heavy solid line shows the combined fitted surface brightness profile.

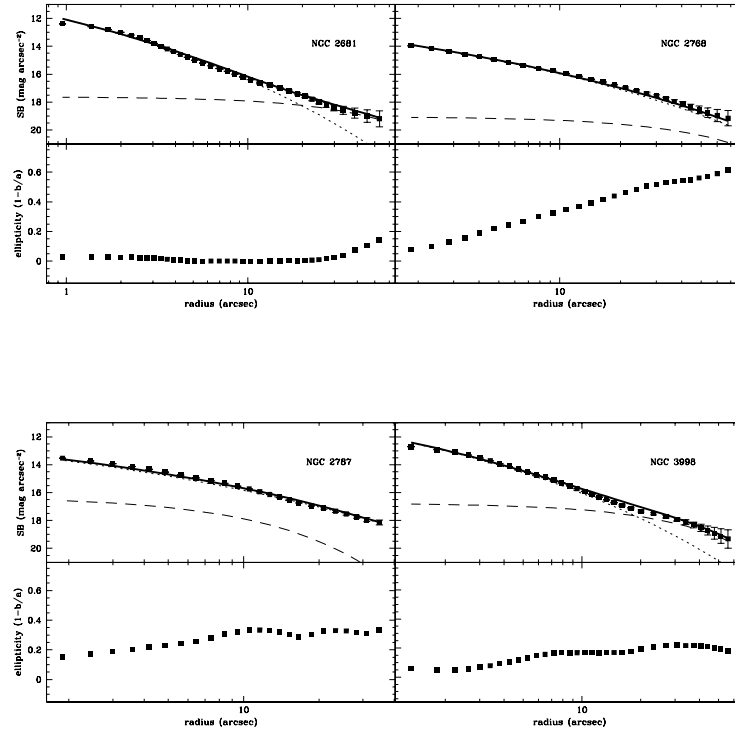


Figure 3.2: Same as figure 3.1.

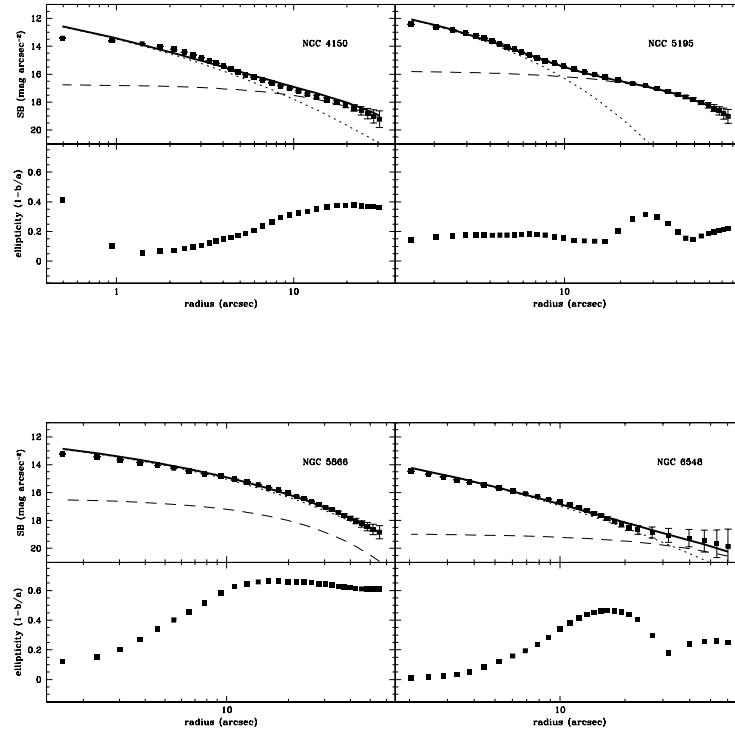


Figure 3.3: Same as figure 3.1.

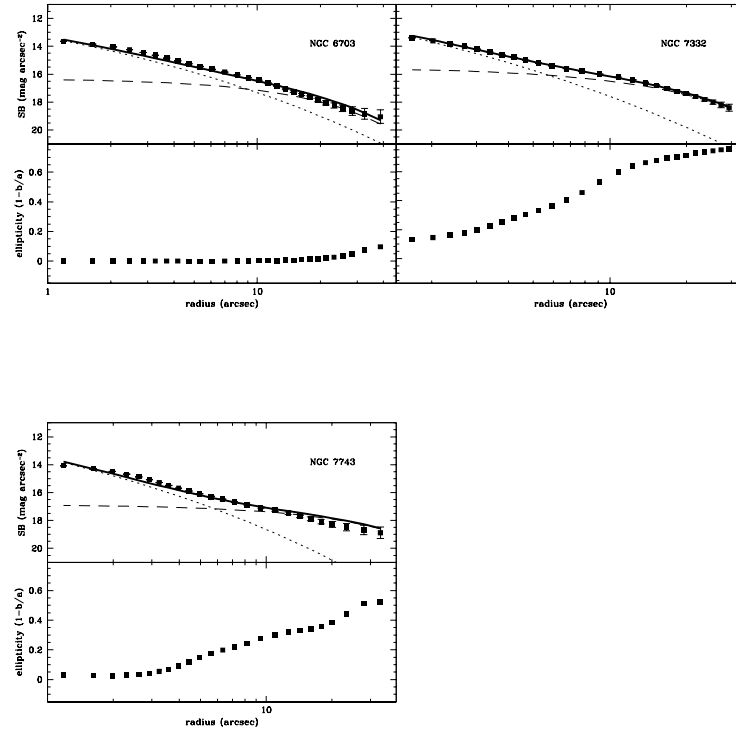


Figure 3.4: Same as figure 3.1.

3.2.3 Kinematic Observations

The kinematic observations for NGC 5128 are described in detail in Silge et al. (2005). For all other galaxies, spectroscopic observations presented in this paper were taken during 40 nights in eight observing runs between December 2000 and March 2003 at McDonald Observatory and during a three-night run in April 2004 at the NASA Infrared Telescope Facility (IRTF). We utilize the $2.29\ \mu\text{m}$ (2-0) ^{12}CO absorption bandhead from evolved red stars to measure the stellar kinematics in our sample. This feature is in a dark part of the infrared sky spectrum and is intrinsically sharp and deep, making it very sensitive to stellar motions (Lester & Gaffney 1994). It is located in an optimal range for studying stellar kinematics where wavelengths are long enough to minimize extinction from dust but short enough to avoid emission from hot dust (Gaffney et al. 1995). Silge & Gebhardt (2003) present a detailed calibration of stellar kinematics measured using the CO bandhead.

At McDonald Observatory, we use CoolSpec (Lester et al. 2000), a near-infrared grating spectrometer, on the 2.7-m telescope. CoolSpec has a 256×256 HgCdTe NICMOS III detector array with a spatial scale of $0''.35\ \text{pixel}^{-1}$. Using a $240\ \text{l/mm}$ grating and $1.8'' \times 90''$ slit, our spectral resolving power is 2300, measured from calibration lamp lines. With this resolution, we can study galaxies with velocity dispersions down to approximately $50\ \text{km s}^{-1}$. Resolving the dispersions of the early-type galaxies presented here is easily within reach of this observational set-up. The spectral scale is $24.6\ \text{km s}^{-1}\ \text{pixel}^{-1}$ and the spectral range is just under $0.05\ \mu\text{m}$, large enough to provide good coverage of the first CO bandhead and continuum on both sides.

At the IRTF, we use SpeX (Rayner et al. 2003), another medium-resolution near-IR spectrograph. SpeX has a Raytheon 1024×1024 InSb array with a spatial scale of $0''.15\ \text{pixel}^{-1}$. Using the $0''.30 \times 60''$ slit in single-order long-slit mode, we obtain spectral resolving power of 2000, measured from calibration lamp lines. The

spectral range of SpeX is much larger than that of CoolSpec; use an order-sorting filter, we obtain the spectrum from $1.96\ \mu\text{m}$ to $2.52\ \mu\text{m}$ with a spectral scale of $\sim 70\ \text{km s}^{-1}\ \text{pixel}^{-1}$. With this spectral range, we can use several of the CO bandheads for the kinematic fitting.

We observe A dwarfs, which have nearly featureless spectra in this region (Wallace & Hinkle 1997), along with the galaxies to obtain the shape of the telluric absorption spectrum. Silge & Gebhardt (2003) present more details on this aspect of the observations, explaining why it is very important to take a careful (and frequent) measure of this spectral shape, particularly at McDonald using CoolSpec. We choose A dwarfs spatially near each galaxy and observe one before and after (and sometimes in the middle of) each galaxy observation. The observations are made by dithering the object across the slit to measure the sky at the same slit position in alternating exposures. Individual exposures are 120 seconds for the galaxies and ten seconds for the stars. Total integration times for the galaxies vary from about one hour to almost five hours. Galaxies that require very long integration times or that are at low declinations are observed during several nights to maintain reasonable airmasses. The slit is rotated to the position angle of the galaxy major axis as quoted in the RC3. Ar and Ne emission lamps calibrate the wavelengths of the exposures; at McDonald, calibration exposures are taken every 24 minutes because we find the wavelength solution drifts significantly with time. The telescope guides on either the galaxy itself or a nearby star (if available) using the optical dichroic mirror autoguider at McDonald. At the IRTF, the autoguider uses spillover near-IR light from the slit. No attempt is made to flux calibrate the spectra since we are mainly concerned with the kinematic analysis.

3.2.4 Data Reduction

Data reduction proceeds as described in Silge & Gebhardt (2003), in generally the same manner for both the McDonald and IRTF data; we more briefly describe the process here. We rectify the images in the spectral direction using the arc lamp lines and subtract an additive constant measured in each individual exposure. We make background images for groups of exposures and subtract them, then shift all the images to the same wavelength solution. The images are then shifted in the spatial direction so that the center of the galaxy in each image is aligned; we calculate the biweight (Beers et al. 1990) of all the processed images to make one image for the galaxy. The one-dimensional spectra are extracted from the two-dimensional images for basically the entire galaxy; we choose the number of columns to extract to maximize signal-to-noise. This varies between $4''$ and $20''$; the extraction windows are presented in Table 3.3. The extraction windows are $\leq r_{eff}$ of the bulge for each galaxy, and for the lenticular galaxies are less than the radius where the bulge dominates the light. Thus our kinematic measurements reflect the dynamics of the bulge only and are not significantly contaminated by disk light. For some high S/N galaxies, we are also able to extract spatially resolved spectra, although we do not present this data here. The stellar spectra are reduced in a similar manner.

To remove the telluric absorption spectrum, the galaxy spectra must be divided by a “flat” spectrum, obtained from the A dwarfs. We obtain the best results by averaging together all the A dwarf spectra from a run to make a smooth, high S/N sky spectrum. Dividing by only an individual A star does not give results as good as the smooth sky spectrum made from many A stars because of the fluctuations in the individual spectra. The galaxy spectra are taken over long periods of time (≥ 1 hour) which average over many such fluctuations while each individual A dwarf spectra takes a very short time (~ 1 minute). These individual stars change because of fluctuations in the sky, not because of problems with S/N; telluric absorption is

removed from the galaxies better when we divide by a “master” A dwarf spectrum.

3.2.5 Extracting the Velocity Distribution

Once we have the spectrum for each galaxy, we extract the kinematic information from it. A galaxy spectrum is the convolution of the line-of-sight velocity distribution (LOSVD) with an average stellar spectrum. There are several techniques used to obtain the internal kinematic information from a galaxy spectrum, such as the cross-correlation technique and the Fourier quotient technique (Tonry & Davis 1979; Sargent et al. 1977). We use the fitting technique of Gebhardt et al. (2000c), deconvolving the spectrum directly in pixel space using a maximum penalized likelihood estimate to obtain a nonparametric LOSVD. An initial velocity profile is chosen and this profile is convolved with a stellar template spectrum. The residuals to the galaxy spectrum are calculated and the velocity profile is changed to minimize the residuals and provide the closest match to the observed galaxy spectrum.

The choice of template star proves to be important for the fitting results (Silge & Gebhardt 2003). We find that the dispersion measured by the fitting program depends on the template spectrum chosen for the fitting, so we give the fitting program a variety of template stellar spectra and allow it to vary the weights given to the different stars to obtain the best fit. As a result, along with the LOSVD information, the fitting program also provides stellar population information. We use the near-IR stellar spectral atlas of Wallace & Hinkle (1997) as our templates, choosing eight stars with CO equivalent widths ranging from less than 5 Å to over 20 Å. These spectra have a somewhat higher spectral resolution than either the McDonald or IRTF observations, so before using them as stellar templates we have carefully convolved them to the relevant spectral resolution. The best fit almost always gives most of the weight to a few of the template stars.

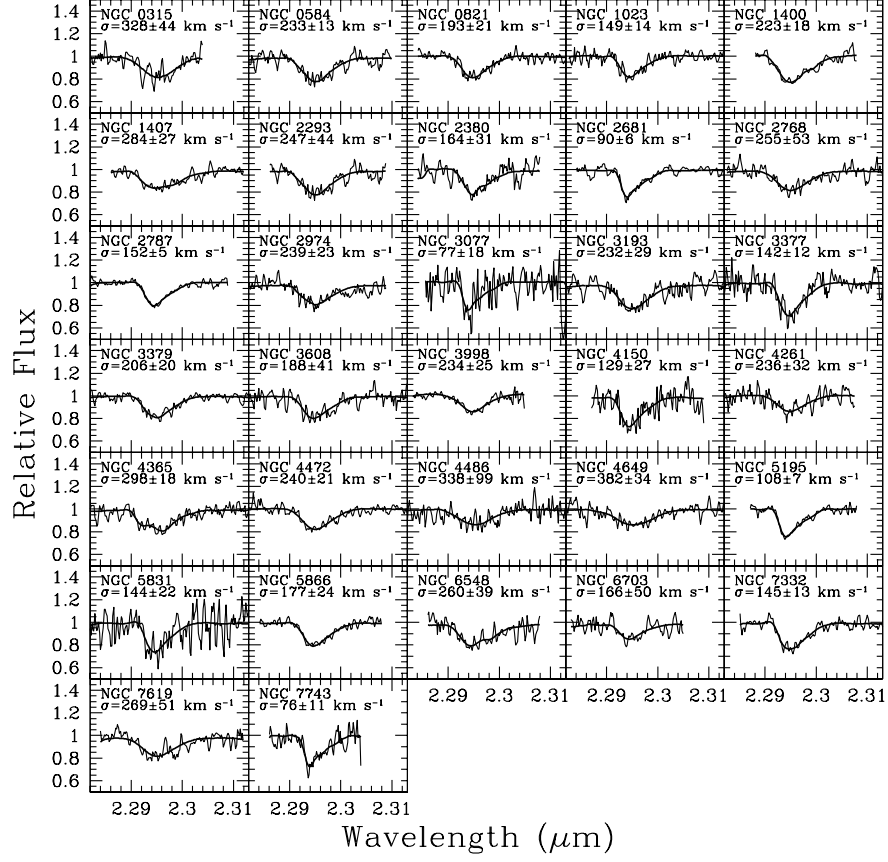


Figure 3.5: Rest-frame spectra for galaxies observed at McDonald Observatory (noisy line) and for the template stellar spectrum convolved with the derived LOSVD (smooth line). The derived velocity dispersion and its 68% uncertainty are reported for each galaxy.

Most LOSVD fitting techniques make some assumption about the shape of the LOSVD, i.e. it is Gaussian or a Gauss-Hermite polynomial. Our technique obtains a nonparametric LOSVD; no a priori assumptions about the shape of the LOSVD are made except that it is nonnegative in all bins. To measure a dispersion from this nonparametric LOSVD, we fit a Gauss-Hermite polynomial to it and use the second moment as the dispersion. Some of the galaxies in this sample with the lowest S/N ratios required the assumption of a Gaussian LOSVD in order to achieve a sensible velocity distribution. We compared the derived nonparametric and Gaussian LOSVDs for galaxies with higher S/N and found good agreement between them. Figures 3.5 and 3.6 show the results for the 34 sample galaxies observed at McDonald or the IRTF and the derived velocity dispersion for each galaxy. The noisy line is the observed spectrum for each galaxy and the smooth line is the template stellar spectrum convolved with the derived LOSVD.

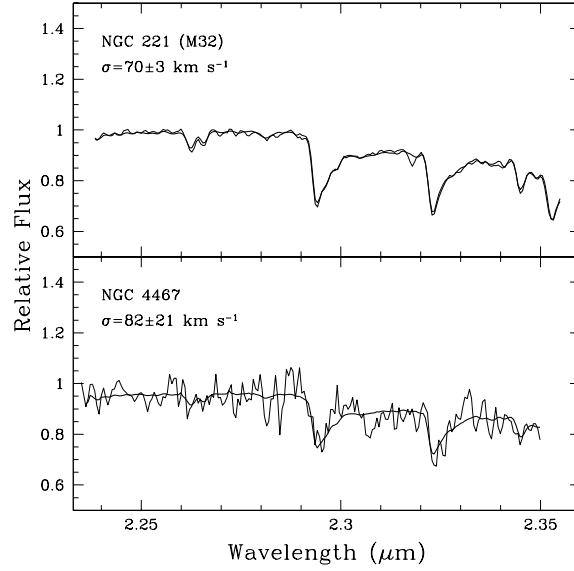


Figure 3.6: Same as figure 3.5 but for galaxies observed at IRTF.

We determine the uncertainties for the velocity dispersions using the Monte Carlo bootstrap approach of Gebhardt et al. (2000c). The initial fit to the observed galaxy spectrum is used to generate 100 simulated spectra with noise chosen to match that of the observed spectrum. These 100 synthetic galaxy spectra are then deconvolved to determine their LOSVDs in the same way the original observed spectrum is deconvolved. These LOSVDs provide a distribution of values for each velocity bin which allows us to estimate the uncertainty and examine any bias in the dispersion. The median of the distribution determines any potential bias from the initial fit, and the spread of the distribution determines the uncertainty. In order to generate the 68% confidence bands, we choose the 16% to 84% values from the 100 realizations. Using this technique and spectral feature, we find 10% accuracy in the velocity dispersion requires S/N per pixel of about 25 or 30.

Table 3.3 includes the velocity dispersions and uncertainties for our sample galaxies. We have repeated the LOSVD analysis for the galaxies of Silge & Gebhardt (2003), most of which appear here. Due to some small changes in procedure, we are now reporting different velocity dispersions for some of those galaxies. While these new measurements do supersede those of Silge & Gebhardt (2003), the differences are small (almost always within the reported uncertainties) and do not affect the conclusions of that paper.

To examine these velocity dispersions in the context of other measurements for these galaxies, we take the twenty-four of our sample galaxies that have dispersions in Trager et al. (1998). Figure 3.7 compares σ in Trager et al. (1998) with the dispersion we measure here using the CO bandhead. Fitting a line by least squares to these data, we find the slope of the best-fit line is 1.038 ± 0.050 , consistent with unity, and the intercept is 3.2 ± 6.7 , consistent with zero, indicating there are no systematic differences between the two dispersion measurements. This is consistent with the conclusions of Silge & Gebhardt (2003); these 24 galaxies are almost all

ellipticals, which appear to have consistent IR and optical kinematics. The scatter of this relation is high, however. The χ^2 of this best fit is 62.3. If we assume there should be a correlation between the dispersions, this implies that either the errors are underestimated or the scatter is real. A χ^2 of 24 (matching the 24 constraints) implies all errors would have to be scaled up by 60%, an unrealistic possibility. This high scatter is likely a combination of the low uncertainties quoted by Trager et al. (1998) and galaxy-to-galaxy differences in stellar population differences and/or dust.

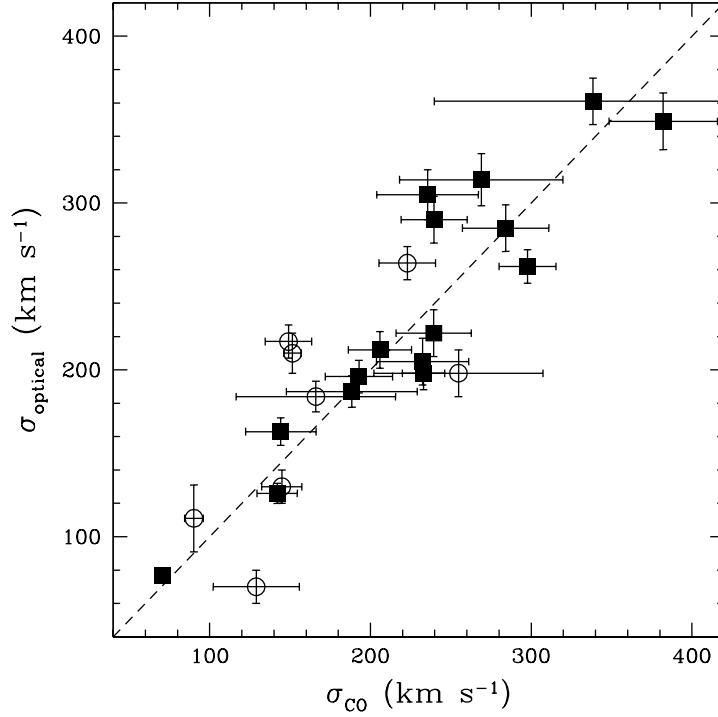


Figure 3.7: Correlation between the dispersion measured from the CO bandhead and the optical dispersion from Trager et al. (1998). The dashed line has a slope of unity. The open circles are S0s and the filled squares are Es.

3.3 The Fundamental Plane

A relationship among the quantities of the FP is predicted by the virial theorem, but the observed FP

$$r_{eff} \propto \sigma^a I_{eff}^b$$

where r_{eff} is the effective radius, σ is the velocity dispersion, and I_{eff} is the mean surface brightness within the effective radius, has coefficients which are significantly different from the simplest virial prediction. The observed relation has a ranging from less than 1.2 to more than 1.5 (the virial prediction is 2) and $b \approx -0.8$ (the virial theorem predicts -1). There is a relatively large spread in published values of a , as pointed out in Bernardi et al. (2003a) and the references cited there, with a generally larger at longer wavelengths. The highest values for a are found in FP studies combining near-infrared imaging and optical kinematics, such as the K -band FP study of mostly rich clusters of Pahre et al. (1998) with $a = 1.53 \pm 0.08$, although the K -band FP study of Coma galaxies of Mobasher et al. (1999) has a somewhat lower value with a large uncertainty ($a = 1.38 \pm 0.26$). The values for b are more consistent between different authors, hovering around -0.8.

Whatever the heterogeneity between authors, the FP is found to be different from the simplest virial prediction at all wavelengths. There are several explanations for these differences. One is that the mass-to-light ratio of a galaxy varies with luminosity (or equivalently, mass). Another is that galaxy families are not dynamically and/or spatially homologous. A still further possibility is that the observed properties are not the relevant ones which enter into the virial theorem. For instance, it is generally assumed that the kinetic energy of the virial theorem is proportional to the square of the observed velocity dispersion. Busarello et al. (1997) find that this is not the case, however; these authors find that the kinetic energy of the galaxies in their sample is proportional to $\sigma^{1.6}$, closer to the measured scaling relations.

The differences from the simplest virial predictions for the FP may be due to any combination of these possibilities, or others not yet considered. Fortunately, the detailed shape of the FP in different passbands can differentiate between the relative importance of these effects in galaxy evolution. For instance, if the tilt of the FP is due to breakdown of homology it must persist at all wavelengths, while the tilt would likely change significantly with wavelength if it is due to metallicity and/or age (i.e. M/L ratio) effects.

3.3.1 Fitting the Fundamental Plane

The observed FP is defined by

$$\log r_{eff} = a \log \sigma + b \log I_{eff} + c$$

where the coefficients a , b , and c determine where the plane lies in the three-dimensional space made up of the observed parameters. These coefficients are found by minimizing the residuals from the plane for a given dataset. This is done generally in two ways, either by minimizing the scatter orthogonal to the plane or by minimizing the scatter in the r_{eff} -direction. The FP has been used as a distance indicator, for which one would want the r_{eff} scatter minimized, but for most applications the desired fit is the more physically meaningful orthogonal fit. The coefficients found using the two approaches can be quite different (Bernardi et al. 2003a). To minimize the scatter orthogonal to the plane, we take

$$\Delta \equiv \frac{\log r_{eff} - a \log \sigma - b \log I_{eff} - c}{(a^2 + b^2 + 1)^{1/2}}$$

and summing up Δ^2 over all the galaxies in the dataset, find the values of a , b , and c which minimizes the sum. In principle, this can be solved analytically but we choose instead to minimize this function numerically using the downhill simplex

method.

We use an larger sample to compare to our all-IR data to further understand the behavior of the FP. We take galaxies from the sample of Bernardi et al. (2003a), a FP study of nearly 9000 early-type SDSS galaxies. Bernardi et al. (2003b) present effective radii and surface brightnesses in four optical bands for these galaxies along with velocity dispersions. We then gather infrared photometric measurements for each galaxy from the 2MASS XSC, completing the data we need to build an IR FP. Of the 8692 galaxies used by Bernardi et al. (2003a), 5757 have K -band total magnitudes and effective radii in the 2MASS XSC. These galaxies are smaller than those in our main sample, and are likely affected by the limited spatial resolution of 2MASS ($2.5''$ to $3''$). Of the 5421 galaxies, only 316 have $r_{eff,K} > 5''$. To determine any bias from the seeing, we repeat the K -band FP analysis described below for galaxies from this sample which have $r_{eff,K} > 5''$ and $r_{eff,K} > 4''$. Table 3.4 presents the data for the comparison sample with both optical and IR photometry and optical kinematics.

We first fit an optical FP to the whole SDSS sample of ~ 9000 galaxies to compare our fitting procedure with that of Bernardi et al. (2003a). These authors present several different fits for each band but in the end quote their maximum likelihood fit; this procedure accounts for the magnitude limit, velocity dispersion cut, and other statistical details of their sample. Their maximum likelihood fit for the r^* band is

$$a = 1.49 \pm 0.05, b = -0.75 \pm 0.01, c = -8.778 \pm 0.020$$

while the result for our fitting procedure is

$$a = 1.51 \pm 0.07, b = -0.76 \pm 0.02, c = -8.99 \pm 0.03.$$

These coefficients are in excellent agreement, especially considering the differences in fitting procedure. The intrinsic orthogonal scatter with respect to our fit (measured by subtracting the measurements errors in quadrature from the observed scatter) is 0.053 while the reported intrinsic scatter with respect to the fit of Bernardi et al. (2003a) is 0.052, in good agreement.

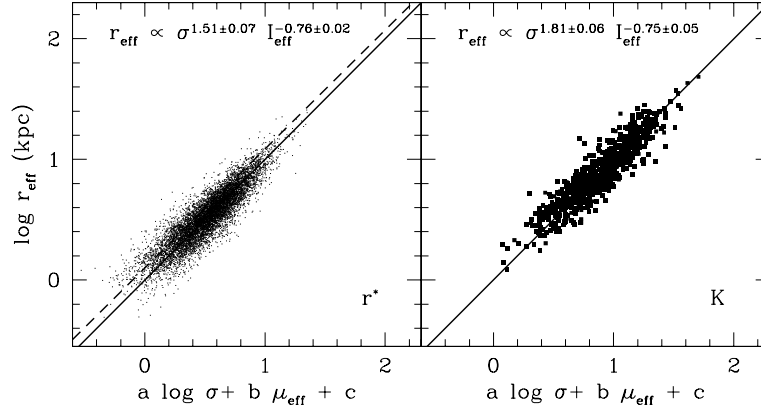


Figure 3.8: The r^* -band (left-hand panel) and K -band (right-hand panel) Fundamental Plane for the sample of Bernardi et al. (2003a). The best-fit FP coefficients for each band are shown; the heavy solid line is the projection of that FP in this plot. The dashed line in the r^* -band plot is the projection of the orthogonal fit of Bernardi et al. (2003a).

We can then fit a FP to the data with IR photometry using the same method. We find for this sample with IR photometry and optical kinematics that

$$a = 1.79 \pm 0.05, b = -0.87 \pm 0.03, c = -9.23 \pm 0.04.$$

The intrinsic scatter is 0.052, very similar to that of the r^* -band FP. This sample includes many galaxies for which the measure of $r_{eff,K}$ is biased high by the seeing.

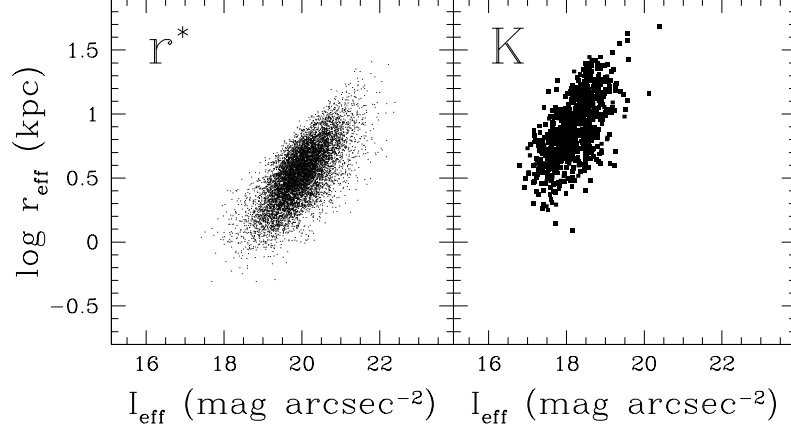


Figure 3.9: The r^* -band (left-hand panel) and K -band (right-hand panel) Kormendy relation for the sample of Bernardi et al. (2003a).

We fit a FP to a subset of these galaxies which have $r_{eff,K} > 4''$ ($N = 786$) and find

$$a = 1.81 \pm 0.06, b = -0.75 \pm 0.05, c = -8.43 \pm 0.08.$$

We repeated this for the galaxies with $r_{eff,K} > 5''$ and find similar results. The intrinsic scatter for this fit is 0.042. This subset has a similar distribution in $r_{eff,K}$ and $I_{eff,K}$ as the sample as a whole. The seeing apparently does not affect a much but does bias b and c significantly. Figure 3.8 presents the FP results for these fits. The left-hand panel shows the r^* -band data; the solid line is our fit and the dashed line is the fit of Bernardi et al. (2003a); the right-hand panel shows the K -band data and our FP fit for the galaxies with $r_{eff,K} > 4''$. Table 3.4 presents the FP quantities for the $N = 5727$ comparison sample. The table in its entirety is available from the authors; a portion is shown here for guidance regarding form and content. R.A. and declination are in J2000.0 coordinates, m_K and $r_{eff,K}$ are from the 2MASS XSC, and r_{eff,r^*} , I_{eff,r^*} , and σ_0 are from Bernardi et al. (2003b).

Since the velocity dispersions which go into these two FPs are the same, the difference in the tilt of these planes comes from the difference in the photometry, i.e. the difference between the r^* -band and K -band Kormendy relation (Kormendy 1977). The Kormendy relation, one projection of the FP, is shown in figure 3.9 for this comparison sample. The K -band Kormendy relation is significantly steeper than the r^* -band relation; larger galaxies have lower densities, and this relationship is stronger in the near-IR than the optical.

Having examined this larger comparison sample, we can turn to the 35 galaxies in our all-IR sample. We find

$$a = 1.72 \pm 0.09, b = -0.62 \pm 0.06, c = -7.44 \pm 0.33.$$

Figure 3.10 presents these FP results. The open circles are lenticular galaxies and the filled squares are elliptical galaxies. The error bars in the lower right-hand corner show typical sizes of uncertainties for these galaxies; the uncertainties are dominated by the velocity dispersion uncertainties. The heavy dashed line is the projection of our fitted FP in these coordinates. The small points are from our comparison sample using K -band photometry and optical kinematics. The intrinsic scatter around this fit is 0.069, somewhat larger than that of the Bernardi et al. (2003b). This FP fit is in agreement with the comparison sample discussed above (except for the zero-point offset). It is somewhat steeper than the FP of Pahre et al. (1998) using K -band photometry and optical kinematics. A fit to only the true elliptical galaxies in the sample gives coefficients in good agreement with the sample as a whole:

$$a = 1.78 \pm 0.07, b = -0.60 \pm 0.05, c = -7.69 \pm 0.34.$$

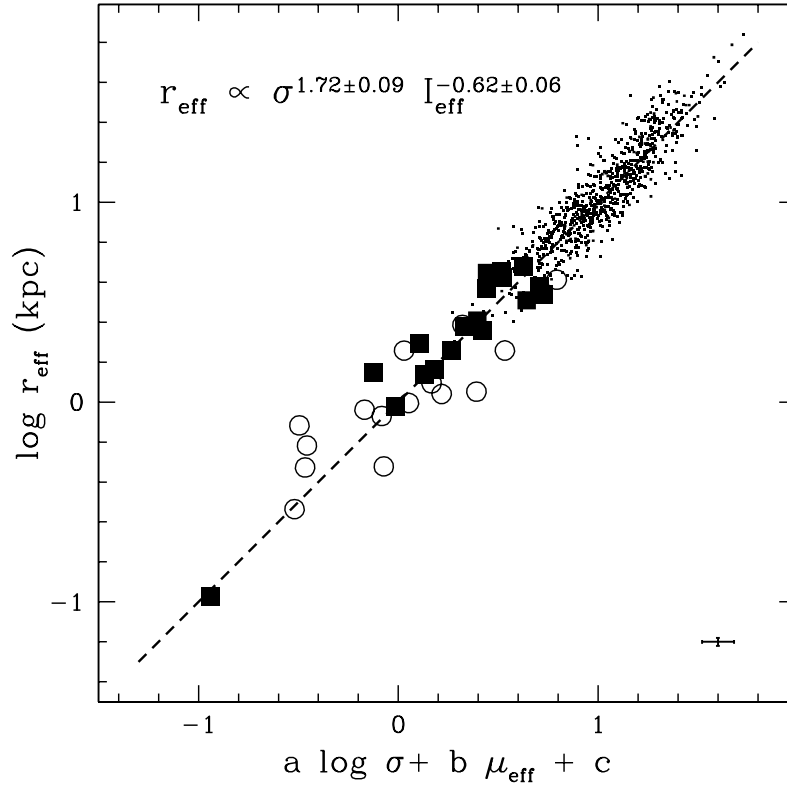


Figure 3.10: The all-infrared Fundamental Plane. The best-fit FP coefficients for our main sample (large squares and circles) are shown; the heavy dashed line is the projection of that FP in this plot. The open circles are S0s and the filled squares are Es. The error bars in the lower right-hand corner show typical sizes of errors for the galaxies of this sample. The small points are from the comparison sample of Bernardi et al. (2003a) using K -band photometric data, as in the right-hand panel of figure 3.8.

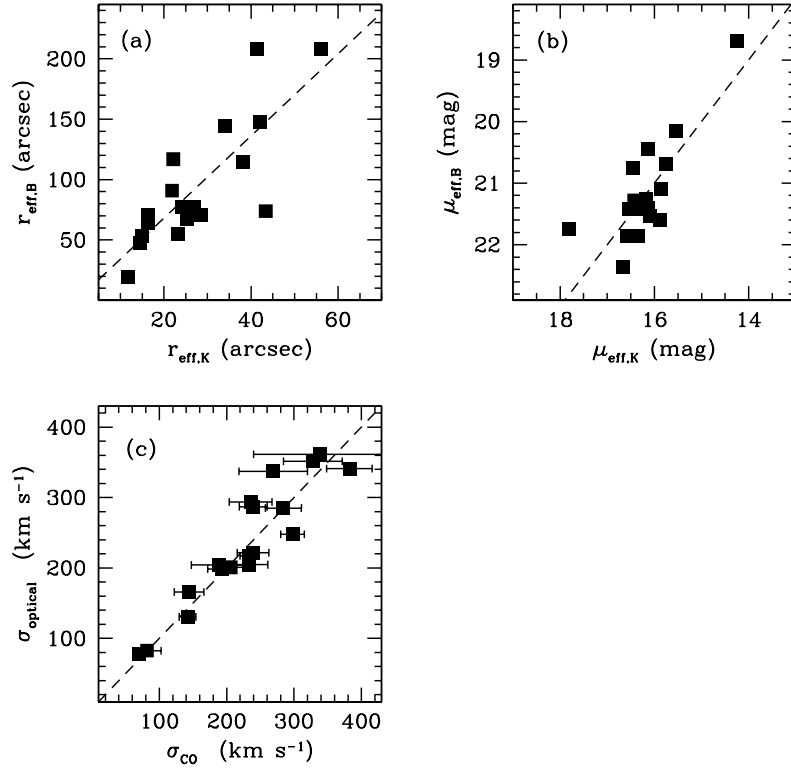


Figure 3.11: Infrared versus optical quantities from Faber et al. (1989) for sample elliptical galaxies. (a) K -band effective radius versus B -band effective radius. The dashed line shows the location of the relation $r_{\text{eff},B} = 3.4r_{\text{eff},K}$. (b) K -band effective surface brightness versus B -band effective surface brightness. The dashed line shows the location of $\mu_{\text{eff},B} = \mu_{\text{eff},K} + 5$. (c) Velocity dispersion measured using infrared wavelengths versus optical velocity dispersion. The dashed line shows where the two measurements are equal.

We can construct a different kind of comparison sample using just the elliptical galaxies. These are well-studied, nearby galaxies which have been included in previous kinematic studies. We can fit a FP to just these galaxies using optical data for the photometry and kinematics, and compare this result to the FP fit just described for the elliptical galaxies only. Faber et al. (1989) include all the ellipticals

(except NGC 3077, a dusty, irregular E0) in their sample and present the necessary data for a comparison. Figure 3.11 presents the three observed quantities that go into the FP for this sample of elliptical galaxies. Each panel shows the infrared quantity plotted versus the optical quantity. The dashed lines in each panel are not fits to the data but rather relations to illustrate the general trends. Panel (a) shows the K -band effective radius versus the B -band effective radius; the dashed line shows the relation $r_{eff,B} = 3.4r_{eff,K}$, the mean scaling for this sample. Panel (b) shows the K -band effective surface brightness plotted against the B -band effective surface brightness. The dashed line here shows the relation $\mu_{eff,B} = \mu_{eff,K} + 5$, which again is the mean relation for these galaxies. Panel (c) shows the velocity dispersion measured using the CO bandhead versus the optical velocity dispersion from Faber et al. (1989). The dashed line here shows where the two measurements are equal. As with the comparison with Trager et al. (1998) shown in Figure 3.7, we see no differences between optical and infrared dispersions for elliptical galaxies.

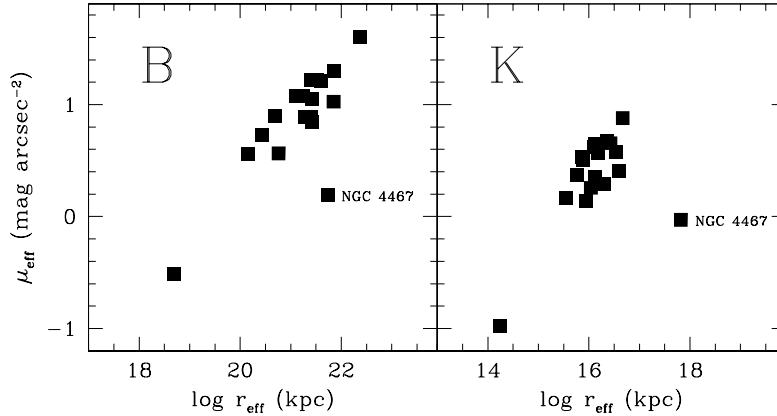


Figure 3.12: The B -band (left-hand panel) and K -band (right-hand panel) Kormendy relation for the sample elliptical galaxies.

There are significant differences between the infrared and optical photometry, however. We can view this in a different way by looking at the Kormendy relation for this sample in a similar way to Figure 3.9. Figure 3.12 present these results. These galaxies are significantly smaller and brighter in K than in B .

We can fit a FP to these galaxies using B -band photometry and optical kinematics from Faber et al. (1989); we find

$$a = 1.39 \pm 0.08, b = -0.73 \pm 0.06, c = -8.67 \pm 0.35.$$

Remember that the FP fit for this same sample of elliptical galaxies using CO band-head kinematics (which are consistent with optical kinematics for these galaxies) and K -band photometry is

$$a = 1.78 \pm 0.07, b = -0.60 \pm 0.05, c = -7.69 \pm 0.34.$$

This result fits with the rest of our FP results. The coefficient a appears to increase with measured waveband, and this steepening is due to changes in the surface brightness profiles with observed color.

3.4 Discussion

Our results here concur with other data in that the slope of the FP departs from the expected virial values at all measured wavelengths. The two assumptions underlying the virial prediction for the FP are that M/L is the same for all elliptical galaxies and that elliptical galaxies form a homologous family in both their photometric and kinematic properties. If departure from homology is the origin of the slope of the FP, the FP should be identical at all wavelengths. If systematic variations in M/L with L are the origin, then a FP using infrared photometry should be quite different from an optical FP. We find the second case to be true; the all-IR FP for our main sample

and the FP of the comparison sample using IR photometry are both steeper than optical FPs. Since our dispersions are consistent with optical measurements, the source of this steepening is the photometric quantities. This steepening indicates that systematic variations in M/L with L must play a role in the form of the FP. We have other evidence that M/L varies with galaxy luminosity; for instance, Drory et al. (2004) derive stellar masses and K -band M/L ratios for more than 5000 galaxies and find that M/L increases with stellar mass and Kauffmann et al. (2003) present a similar result for more than 10^5 galaxies, finding that optical M/L increases with galaxy luminosity. Another possibility more recently put forth is that M/L varies with σ ; Cappellari et al. (2005) find that almost all of the tilt away from the simple virial prediction for the FP can be explained by such a relation in a sample of early-type galaxies.

Although M/L variations seem to be important in the slope of the FP, homology effects may still play a role. Trujillo et al. (2004) study the B -band FP and find that the tilt away from the virial prediction can be explained by the combination of the two effects; they find one-quarter of the tilt is due to variation of stellar population and thus M/L , while the remaining three-quarters of the tilt is due to breakdown of homology. They assert that all the difference between the observed K -band FP and the virial prediction is due to nonhomology. Ciotti et al. (1996) use analytical galaxy models to show that breakdown in homology in the surface brightness profiles could, under specific circumstances, be the cause of the slope. It is also found that dynamical nonhomology can have a strong effect on the slope of the FP (Graham & Colless 1997; Busarello et al. 1997). Busarello et al. (1997), mentioned earlier, use spatially resolved kinematics and simplified dynamical models to find that the kinetic energy of a galaxy does not scale with σ_0^2 (where σ_0 is the central velocity dispersion) but rather with $\sigma_0^{1.6}$. Our results are not exactly comparable with theirs, since we use a global measure of σ which includes rotation.

Studying a sample of galaxies with spatially resolved kinematics would allow us to further address this question of dynamical nonhomology but these first results seem to indicate that the difference between the virial prediction and the observed FP at K may be due to systematic breakdown in homology while the variation in the slope of the FP with observed wavelength may be explained by variation of M/L with L .

It has been found in previous studies that the FP has a small amount of intrinsic scatter. Pahre et al. (1998) find that the scatter for a near-IR FP is similar to that of optical FPs. Our findings agree with this; the scatter is very similar for the FPs for our larger comparison sample using optical ($\text{rms} = 0.053$) or IR ($\text{rms} = 0.052$) photometry. The intrinsic scatter for our main sample is somewhat larger ($\text{rms} = 0.069$), similar to the scatter reported for local optical FP samples such as that of Jorgensen et al. (1996). The similarity of this intrinsic scatter across observed wavelength indicates that the source of the scatter in the FP is not galaxy-to-galaxy differences in dust content, star formation history, metallicity, etc. If this were the case, the intrinsic scatter in K would be less than at optical wavelengths. Pahre et al. (1998) find no correlation between residuals of the near-IR FP and the $\text{Mg}_2\text{-}\sigma_0$ relation, indicating that age and metallicity are not the controlling parameters in the thickness of these relations. Bernardi et al. (2003b) find that the residuals correlate weakly with local environment but this effect is not enough to explain all the scatter. The source of this intrinsic scatter remains an open question, perhaps due to combined effects of environment, stellar populations, and nonhomology. Distance errors are another possible source of FP scatter.

Our result for the K -band FP is somewhat different than the result of Pahre et al. (1998) with $a = 1.53 \pm 0.08$. One significant difference between our studies is that the sample of Pahre et al. (1998) is mainly galaxies from rich clusters while our sample is made up of local galaxies, all of which are considered field galaxies. There

is other evidence that the FP depends on environment. Treu et al. (2005) find a different evolution in the FP for field galaxies at higher z than previously found for higher- z cluster galaxies (van Dokkum et al. 1998). Also, Bernardi et al. (2003b) find, as stated above, that residuals from the FP correlate with environment, with the residuals increasing with increasing local density. Although it seems likely that the FP does depend on environment, further study is needed to understand how (i.e. variation in slope and/or offset).

3.5 Conclusions

In this project, we have built an all-infrared FP, using both near-IR imaging and kinematics. We have observed 35 nearby early-type galaxies and measured their stellar kinematics using the $2.29\mu\text{m}$ (2-0) ^{12}CO absorption bandhead, combining these new measurements with published 2MASS K -band photometric quantities for these galaxies to examine the tight relationship among the structural and kinematic properties of galaxies known as the FP. This technique allows us to effectively deal with such problems as dust extinction, effects of recent star formation, and sample bias. We also study the FP for a comparison sample using infrared photometry and optical kinematics. For our main sample, we find

$$r_{eff} \propto \sigma^{1.72 \pm 0.09} I_{eff}^{-0.62 \pm 0.06}.$$

This is a markedly steep FP relationship, with larger values for the scaling with σ than found using data from optical wavelengths. These differences imply that although nonhomology may play a role in the shape of the FP, systematic variation of M/L ratio with some galaxy characteristic (such as L or σ) must play a role. The intrinsic scatter for our FP relation ($\text{rms} = 0.069$) is similar to local optical samples, implying that galaxy-to-galaxy differences in dust content, star formation history,

or metallicity are not the driving force behind the thickness of the FP. The source of the scatter in the FP relation remains an open question.

Using both infrared photometry and kinematics opens up new possibilities for studying the FP of galaxies of diverse types. If we come to understand the infrared FP of early-type galaxies, we can move on to study the FP of later-type galaxies. The problems of dust, bias, and star formation are only more severe for these galaxies, and our knowledge of the bulges of disk galaxies is currently limited because of these effects. We can apply the techniques described in this paper to study the FP of bulges more accurately and reliably than ever before. We will be able to study spheroids of all masses in an unbiased way.

Table 3.1: Basic properties of FP sample galaxies

Galaxy	Type	v (km s ⁻¹)	$(m - M)^1$ (mag)	D (Mpc)	M_K^2 (mag)
NGC 221	cE2	-200	24.55	0.813	-19.46
NGC 315	E+ LINER	4942	—	70.6	-26.29
NGC 584	E4	1802	31.52	20.137	-24.22
NGC 821	E6	1735	31.91	24.099	-24.01
NGC 1023	SB(rs)0-	637	30.29	11.429	-24.05
NGC 1400	SA0-	558	32.11	26.424	-24.30
NGC 1407	E0	1779	32.30	28.840	-25.60
NGC 2293	SAB(s)0+ pec	2037	31.16	17.061	-23.65
NGC 2380	SAB0	1782	32.05	25.704	-24.60
NGC 2681	(R')SAB(rs)0/a Sy	692	31.18	17.219	-23.73
NGC 2768	S0	1373	31.75	22.387	-24.75
NGC 2787	SB(r)0+ LINER	696	29.37	7.482	-22.11
NGC 2974	E4	2072	31.66	21.478	-25.40
NGC 3077	I0 pec	14	28.03	4.036	-20.73
NGC 3193	E2	1399	32.66	34.041	-24.68
NGC 3377	E5-6	665	30.25	11.220	-22.81
NGC 3379	E1	911	30.12	10.568	-23.85
NGC 3608	E2	1253	31.80	22.909	-23.70
NGC 3998	SA(r)0 Sy1,LINER	1040	30.75	14.125	-23.38
NGC 4150	SA(r)0	226	30.69	13.740	-21.70
NGC 4261	E2-3	2238	32.50	31.623	-25.24
NGC 4365	E3	1243	31.55	20.417	-24.91
NGC 4467	E2	1423	—	16.5	-20.60
NGC 4472	E2/S0 Sy2	997	31.06	16.293	-25.66
NGC 4486	E0-1 pec Sy	1307	31.03	16.069	-25.22
NGC 4649	E2	1117	31.13	16.827	-25.39
NGC 5128	E0 pec	547	—	3.5	-23.78
NGC 5195	SB0 pec LINER	465	29.42	7.656	-23.17
NGC 5831	E3	1656	32.17	27.164	-23.73
NGC 5866	S0 LINER	672	30.93	15.346	-24.06
NGC 6548	SB0	2174	31.81	23.014	-23.22
NGC 6703	SA0-	2461	32.13	26.669	-23.88
NGC 7332	S0 pec	1172	31.81	23.014	-23.80
NGC 7619	E	3762	33.62	52.966	-25.59
NGC 7743	(R)SB(s)0+ Sy2	1710	31.58	20.701	-23.16

References: (1) from Tonry et al. (2001); (2) calculated using m_K from 2MASS XSC

Table 3.2: Disk/bulge decomposition parameters for lenticular galaxies

galaxy	image source ¹	total bulge flux (mag)	r_{eff} (arcsec)	Sérsic n	axis ratio	total disk flux (mag)	r_d (arcsec)	axis ratio	bulge/total ratio
NGC 1023	LGA	7.01	16.52	3.46	0.77	6.95	56.25	0.28	0.49
NGC 1400	A	8.31	9.68	4.00	0.81	8.75	16.32	0.96	0.60
NGC 2293	LGA	8.17	13.62	4.00	0.81	8.32	45.56	0.62	0.53
NGC 2380	LGA	7.80	14.52	4.00	0.93	8.42	37.55	0.83	0.64
NGC 2681	LGA	8.49	9.15	4.00	0.85	8.04	21.67	0.94	0.40
NGC 2768	LGA	7.48	37.73	4.00	0.67	7.99	43.60	0.32	0.62
NGC 2787	A	7.20	30.29	4.00	0.67	9.52	22.43	0.28	0.89
NGC 3998	A	7.92	6.96	3.50	0.82	8.22	23.31	0.82	0.57
NGC 4150	A	8.92	4.37	4.00	0.72	9.10	14.37	0.65	0.54
NGC 5195	LGA	7.35	12.67	2.04	0.76	6.83	22.14	0.96	0.38
NGC 5866	LGA	6.98	32.67	2.59	0.50	9.00	22.53	0.11	0.87
NGC 6548	A	8.20	16.24	4.00	0.68	9.09	43.58	0.65	0.69
NGC 6703	A	9.03	6.58	4.00	0.91	8.83	12.97	0.94	0.45
NGC 7332	A	9.34	8.87	4.00	0.59	8.42	18.37	0.27	0.30
NGC 7743	A	10.06	6.04	4.00	0.83	8.69	22.27	0.67	0.22

References: (1) LGA = Large Galaxy Atlas (Jarrett et al. 2003), A = 2MASS Atlas image;

Table 3.3: Properties of observed spectra and K -band Fundamental Plane quantities

Galaxy	Total Exposure Time (minutes)	S/N (pixel ⁻¹)	Extraction Window	σ (km s ⁻¹)	r_{eff} (arcsec)	r_{eff} (kpc)	μ_{eff} (mag)
NGC 221	40	125	$0.3'' \times 3.8''$	70 ± 3	26.95	0.106	14.24
NGC 315	160	26	$1.8'' \times 15.4''$	328 ± 44	22.15	7.581	16.67
NGC 584	120	28	$1.8'' \times 10.5''$	233 ± 13	23.27	2.272	16.13
NGC 821	96	33	$1.8'' \times 11.9''$	193 ± 21	21.87	2.555	16.59
NGC 1023	48	28	$1.8'' \times 17.5''$	149 ± 14	16.52	0.915	15.09
NGC 1400	40	32	$1.8'' \times 10.5''$	223 ± 18	9.68	1.240	15.23
NGC 1407	240	37	$1.8'' \times 17.5''$	284 ± 27	34.03	4.758	16.35
NGC 2293	120	19	$1.8'' \times 14.0''$	247 ± 44	13.62	1.127	15.83
NGC 2380	96	18	$1.8'' \times 10.5''$	164 ± 31	14.52	1.809	15.60
NGC 2681	120	56	$1.8'' \times 10.5''$	90 ± 6	9.15	0.764	15.29
NGC 2768	120	24	$1.8'' \times 11.2''$	255 ± 53	37.73	4.095	17.36
NGC 2787	72	67	$1.8'' \times 17.5''$	152 ± 5	30.29	1.099	16.60
NGC 2974	144	26	$1.8'' \times 14.0''$	239 ± 23	43.38	4.517	16.43
NGC 3077	120	12	$1.8'' \times 5.6''$	77 ± 18	48.52	0.950	17.72
NGC 3193	100	23	$1.8'' \times 6.3''$	232 ± 29	14.40	2.376	15.76
NGC 3377	166	19	$1.8'' \times 10.5''$	142 ± 12	25.35	1.379	16.45
NGC 3379	160	45	$1.8'' \times 10.5''$	206 ± 20	28.53	1.462	15.54
NGC 3608	120	21	$1.8'' \times 7.7''$	188 ± 41	16.24	1.804	16.14
NGC 3998	72	45	$1.8'' \times 10.5''$	234 ± 25	6.96	0.477	14.13
NGC 4150	72	13	$1.8'' \times 7.0''$	129 ± 27	4.37	0.291	14.11
NGC 4261	136	21	$1.8'' \times 14.0''$	236 ± 32	24.20	3.710	16.18
NGC 4365	144	28	$1.8'' \times 9.1''$	298 ± 18	38.10	3.771	16.54
NGC 4467	120	27	$0.3'' \times 2.6''$	82 ± 21	11.70	0.936	17.82
NGC 4472	176	42	$1.8'' \times 16.8''$	240 ± 21	56.11	4.432	16.13
NGC 4486	144	19	$1.8'' \times 15.4''$	338 ± 99	41.46	3.230	15.89
NGC 4649	120	30	$1.8'' \times 14.0''$	382 ± 34	42.14	3.438	15.86
NGC 5128	36	83	$3.0'' \times 60''$	138 ± 10	82.6	1.401	14.86
NGC 5195	72	52	$1.8'' \times 7.0''$	108 ± 7	12.67	0.470	14.86
NGC 5831	96	12	$1.8'' \times 2.8''$	144 ± 22	14.90	1.962	16.30
NGC 5866	128	40	$1.8'' \times 14.0''$	177 ± 24	32.67	2.431	16.54
NGC 6548	296	19	$1.8'' \times 6.3''$	260 ± 39	16.24	1.812	16.25
NGC 6703	208	20	$1.8'' \times 9.1''$	166 ± 50	6.58	0.851	15.11
NGC 7332	96	32	$1.8'' \times 6.3''$	145 ± 13	8.87	0.990	16.07
NGC 7619	96	30	$1.8'' \times 14.0''$	269 ± 51	16.39	4.209	16.10
NGC 7743	120	18	$1.8'' \times 4.2''$	76 ± 11	6.04	0.606	15.96

Table 3.4: Fundamental Plane quantites for comparison sample

RA ¹ (°)	dec ¹ (°)	m_K^2 (mag)	$(m - M)^3$ (mag)	$r_{eff,K}^2$ (kpc)	$I_{eff,K}^4$ (mag)	$r_{eff,r*}^3$ (kpc)	$I_{eff,r*}^3$ (mag)	σ^3 (km s ⁻¹)
3.791	-0.031	13.37±0.16	37.389	3.51	17.272	4.08±0.04	20.063±0.012	127±8
3.985	-0.750	13.55±0.21	40.376	21.56	18.404	11.59±0.59	20.701±0.066	266±35
4.159	-0.399	13.91±0.27	37.309	2.77	17.376	2.13±0.04	19.453±0.022	138±8
4.197	-0.644	12.39±0.10	37.371	6.98	17.800	6.10±0.07	20.365±0.015	184±8
4.299	0.854	14.07±0.20	39.824	13.55	18.473	5.14±0.34	19.643±0.056	193±19
4.386	0.557	14.13±0.12	39.559	8.19	17.702	5.06±0.26	19.629±0.038	198±15
4.460	-0.615	13.68±0.20	40.083	16.37	18.231	8.04±0.33	20.297±0.054	223±24
4.555	0.215	13.94±0.19	39.588	11.75	18.265	6.73±0.22	20.326±0.041	210±17
4.589	-0.608	13.84±0.22	40.228	13.46	17.826	7.05±0.19	19.756±0.035	306±31
4.619	-0.334	13.58±0.19	39.582	14.20	18.320	6.50±0.19	19.900±0.038	257±18

References: (1) J2000.0 coordinates; (2) from 2MASS XSC; (3) from Bernardi et al. (2003b); (4) calculated using m_K and $r_{eff,K}$ from 2MASS XSC

Chapter 4

Bulges on the Fundamental Plane of Galaxies

4.1 Understanding Bulges

Recent years have seen a new richness in our knowledge of the bulges of spiral galaxies. These bulges seem similar to elliptical galaxies in many respects and have often been considered elliptical galaxies which just happen to also contain a disk (Renzini 1999). However, as we learn more through improved observations, some characteristics of bulges are inconsistent with such an approach. If bulges (or at least some bulges) are not ellipticals, we would like to know what they are. We want to understand how such a component formed and evolved, and how it is similar or different from an elliptical galaxy. These are difficult galactic components to study, however; they are small compared to an elliptical galaxy, the presence of the disk complicates observations, and they can contain significant amounts of dust which hamper optical observations. These problems only worsen as we attempt to understand galaxies later in the Hubble sequence.

HST observations have allowed a significant step forward in our understand-

ing of bulges. The increased spatial resolution reveals new details in these small bulges. Many of them exhibit spiral structure within the “bulge” region of the galaxy, shallow surface brightness profiles more reminiscent of a disk than an elliptical galaxy, and other characteristics indicative of a non-E identity (Andredakis & Sanders 1994; Andredakis et al. 1995; Carollo et al. 1997, 1998; Carollo 1999; Carollo et al. 2001, 2002; Kormendy & Kennicutt 2004). These recent observations have adjusted the way we think about bulge galaxies and show that we have much to learn about what exactly they are.

One way we study and understand galaxies is through their scaling relations. One such relation is the Fundamental Plane (FP). In the three-dimensional space made up of effective radius (or total luminosity), mean surface brightness, and velocity dispersion, early-type galaxies inhabit a two-dimensional surface, the FP (Djorgovski & Davis 1987; Dressler et al. 1987). A relationship among the quantities of the FP is predicted by the virial theorem, but the observed FP

$$r_{eff} \propto \sigma^a I_{eff}^b$$

where r_{eff} is the effective radius, σ is the velocity dispersion, and I_{eff} is the mean surface brightness within the effective radius, has coefficients which are significantly different from the simplest virial prediction. The observed relation has a ranging from less than 1.2 to more than 1.5 (the virial prediction is 2) and $b \approx -0.8$ (the virial theorem predicts -1). There is a relatively large spread in published values of a , as pointed out in Bernardi et al. (2003a) and the references cited there, with a generally larger at longer wavelengths. The highest values for a are found in FP studies combining near-infrared imaging and optical kinematics, such as the K -band FP study of mostly rich clusters of Pahre et al. (1998) with $a = 1.53 \pm 0.08$ and our value of $a = 1.72 \pm 0.09$ from the previous chapter and Silge & Gebhardt (2005). The values for b are more consistent between different authors, hovering around -0.8.

Whatever the heterogeneity between authors, the FP is found to be different from the simplest virial prediction at all wavelengths. This difference can likely be attributed to variation of mass-to-light ratio with galaxy luminosity, breakdown of dynamical and/or spatial homology, or some combination of these effects. The change of a with observed passband indicates that M/L variation must play a role.

If we come to understand the infrared FP of early-type galaxies, we can move on to study the FP of later-type galaxies. The change (or lack thereof) in the FP with galaxy type can hold important information on the histories and formation mechanisms for galaxies of different morphologies. The locus of bulges in the three-dimensional space of the FP will provide a link between them and ellipticals and is one of the best ways to study the mass growth history of galaxies. The FP of bulges can give us information on the stellar populations, internal structure, and kinematics of bulges in comparison with early-type galaxies. As pointed out by Kormendy & Kennicutt (2004), deviations from the FP are a sensitive test of the relative structure of an elliptical galaxy compared to a bulge component. However, the problems of dust, bias, and star formation are more severe for these galaxies, and our knowledge of the bulges of disk galaxies is currently limited because of these effects.

Previous studies of the FP of bulges (Moriondo et al. 1999; Falc3n-Barroso et al. 2002; Balcells et al. 2004) demonstrate that it is more difficult and than for elliptical galaxies. The more complicated structure of disk galaxies and the important effects of dust present problems for such analysis. Falc3n-Barroso et al. (2002) place 19 bulges on the FP and find that they lie in a slightly different part of parameter space than the elliptical FP; they are slightly below the FP of early-type galaxies, which could be attributed to the bulges being brighter than otherwise similar Es. Moriondo et al. (1999) fit a FP to 40 bulges and find a significantly shallower FP relation than for early-type galaxies, with $a = 0.97 \pm 0.13$ and $b =$

-0.61 ± 0.08 . This shallower FP could indicate a different M/L variation with luminosity for bulges with disks than those without (i.e. elliptical galaxies). These results hold promise in understanding the relationship between bulges and elliptical galaxies; however, their methods may have problems due to dust extinction or bias. Both studies rely on optical spectroscopy. Many disk galaxies are too dusty to be good targets for optical spectroscopy; it is possible that the kinematic measurements are suspect because of the dust or that dusty galaxies have been artificially excluded from the study.

Utilizing kinematic measurements from the CO bandhead, we are uniquely able to look through the dust to a large extent and more accurately understand the FP of diverse morphological types. We can apply these methods to study the FP of bulges more accurately and reliably than ever before. Using infrared wavelengths for both kinematics and photometry holds promise in understanding the FP of bulges. Observing in the near infrared traces the older, redder stellar population whose kinematics are a more accurate reflection of the actual potential of the galaxy. Effects from recent star formation, often a problem for kinematic analysis of late-type galaxies, are lessened. Also, near-infrared wavelengths are long enough to minimize extinction from dust. K -band observations allow us to look through the dust to a large extent and observe the unobscured starlight. Dust lanes and other features are normally seen in late-type galaxies, and this dust can have a significant effect on both the observed structure and kinematics of these galaxies (Baes & Dejonghe 2000; Baes et al. 2000; Baes & Dejonghe 2001, 2002). It is known that IR photometry and morphology are different than in the optical (Pahre et al. 1998; Jarrett et al. 2003), but galaxy kinematics may be dust-affected as well (Silge & Gebhardt 2003).

In this paper, we have combined new stellar kinematic measurements with 2MASS photometry to study the FP of bulges. We can expand the parameter space within which galaxies are well-studied and address issues critical for galaxy

evolution. This paper is organized as follows: Section 2 presents the data, Section 3 discusses the FP for these galaxies, Section 4 presents our discussion of these results and conclusions.

4.2 Data

4.2.1 Sample

Table 4.1 includes the 45 galaxies in this paper. The sample is made up of spiral galaxies from type S0/a to Sd. Figure 4.1 presents a histogram of the sample by type; the bulk of galaxies are of type Sbc or earlier. Twenty-four of the galaxies show signs of nuclear activity, i.e. are classified as Seyfert galaxies or LINERs. Since beginning this near-infrared kinematic study in December 2000, we have obtained spectra for over 80 galaxies. Forty-five of these galaxies are of type S0/a or later and make up the sample presented here.

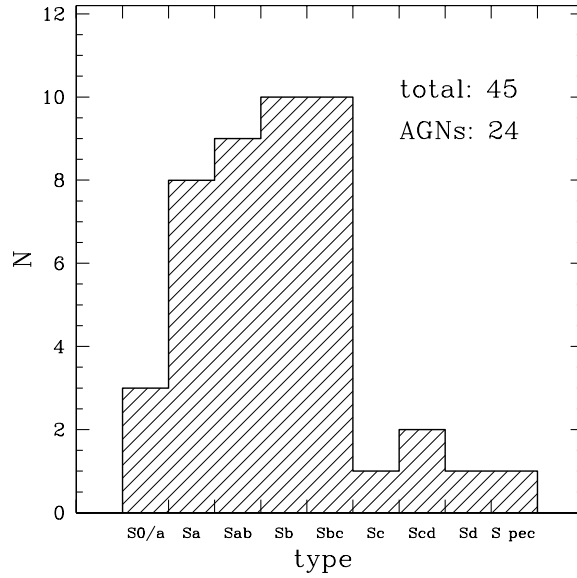


Figure 4.1: Histogram showing the morphological type of the sample galaxies.

In order to construct a FP, we need reliable distances to each galaxy to transform the observed sizes to physical sizes. Ten of the 45 galaxies are part of the sample of Tonry et al. (2001), who report distances based on surface brightness fluctuations. For the other galaxies, we use the Virgocentric flow model of Kraan-Korteweg (1986) as implemented by Kormendy & Freeman (2004). We use the distance from Tonry et al. (2001) when available and the distance from the Virgocentric flow model for the other galaxies. Fortunately, we have distances based on surface brightness fluctuations for most of the nearest galaxies, which are the least well-described by the Virgocentric flow model. NGC 4438, an S0/a in the Virgo cluster with a particularly low velocity, is assumed to be at the distance to the Virgo cluster, $D = 16.5$ Mpc.

The galaxy type and heliocentric velocity (from NED), distance modulus (from Tonry et al. 2001 when available), calculated distance (either from the distance modulus or the Virgocentric flow model), and the absolute K magnitude (calculated using the total apparent K magnitude from the 2MASS XSC) are listed in Table 4.1.

4.2.2 2MASS Photometric Quantities

To construct the FP, we need photometric measurements (effective or half-light radius r_{eff} and mean surface brightness within the effective radius I_{eff}) as well as kinematic measurements (velocity dispersion σ). The Two Micron All Sky Survey (2MASS) has imaged the entire sky in the J , H , and K bands and makes this data publicly available through the Infrared Science Archive (Cutri et al. 2003). This is an excellent resource, proffering a large, homogeneous, accessible imaging dataset. The sensitivity and angular resolution of 2MASS are more than adequate to study the nearby galaxies in our sample. We choose to utilize the K -band images since this light is the best tracer of the old stellar population and is most reflective of the

potential of the galaxy.

For these spiral galaxies, we perform a bulge/disk decomposition on the 2MASS images to find r_{eff} and I_{eff} for the bulge component. Neglecting such a step would bias our results for the photometric quantities for these galaxies, attributing light to the bulge which properly belongs to the disk. We utilize images from the 2MASS Large Galaxy Atlas (LGA) (Jarrett et al. 2003) when available. These authors construct large mosaics for the largest galaxies as seen in the near-infrared. Jarrett et al. (2003) join 2MASS scans and iteratively remove the sky background, resulting in carefully constructed, well-calibrated images of these galaxies. For galaxies not included in the LGA, we use the regular 2MASS Atlas image. Of the 45 galaxies in our sample, 35 are in the LGA. We have compared the results of our photometric fitting using both LGA and Atlas images; we do not find significant differences although the LGA images are easier to use and better calibrated. We use the multi-Gaussian expansion (MGE) method of Cappellari (2002) to fit the surface brightness profile to the 2MASS image. The MGE method is a simple parametrization flexible enough to model realistic multicomponent objects. This method uses a series expansion of two-dimensional Gaussian functions to represent galaxy images. For most of the galaxies, we obtain a good fit by holding the position angle constant, but fifteen galaxies required varying the position angle to obtain a good fit.

We fit

$$I(r) = I_b \exp \left[-b_n \left(\left(\frac{r}{r_{eff}} \right)^{1/n} - 1 \right) \right] + I_d \exp \left(-\frac{r}{r_d} \right)$$

to the galaxy images using the two-dimensional fitting algorithm GALFIT (Peng et al. 2002). The first term represents the bulge with a Sérsic function, where I_b is the central bulge intensity, r_{eff} is the effective (or half-light) radius, n determines the variation with radius ($n = 1$ for an exponential disk, $n = 4$ for a deVaucouleurs profile), and $b_n \sim 2n - 0.324$. We fit both a Sérsic profile ($r^{1/n}$) and a deVaucouleurs

profile ($r^{1/4}$). For some galaxies, the Sérsic index n is not well-determined; this quantity is quite sensitive to the background sky. Changes in n can affect the measured r_{eff} but also affect the measured I_b in such a way that galaxies move along the FP, not away from it, as indicated by Kelson et al. (2000). We use the Sérsic profile when it is well-determined and the deVaucouleurs profile for the other cases; the uncertainty in the actual value for n does not affect our FP results. The second term represents the disk with an exponential profile, where I_d is the central disk intensity and r_d is the disk scale length. Table 4.2 presents the results for the bulge/disk decomposition for the 45 spiral galaxies in the sample, and figures 4.2 through 4.13 illustrate these fits. Each panel presents the data for one galaxy: the major axis surface brightness profile extracted from the image using the MGE method (points with error bars) along with the fitted profiles from GALFIT and the ellipticity profile. In the surface brightness profile plots, the dotted line shows the bulge component, the dashed line shows the disk component, and the heavy solid line shows the combined fitted surface brightness profile. We assume 5% uncertainties on these photometric quantities in order to be consistent with our procedure for the early-type galaxies in the previous chapter.

In general, uncertainties in photometric quantities due to the details various fitting procedures have little effect on the FP. Kelson et al. (2000) find that differences cause galaxies to move along the plane, not away from the plane, and thus cannot change the coefficients of the FP. We find this as well, for example, in comparing a deVaucouleurs versus Sérsic profile.

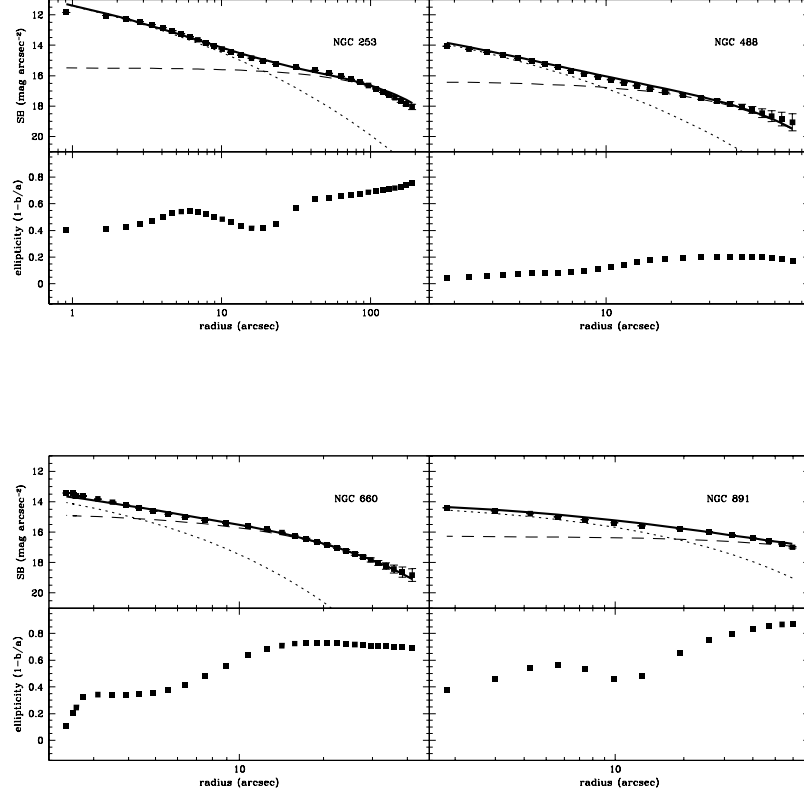


Figure 4.2: Surface brightness profile and bulge/disk decomposition information for each galaxy. For each galaxy, the top panel presents the surface brightness profile and the bottom panel shows the ellipticity profile. In the surface brightness profile panels, the points with error bars show the major axis surface brightness profile extracted from the image using the MGE method, the dotted line shows the bulge component, the dashed line shows the disk component, and the heavy solid line shows the combined fitted surface brightness profile.

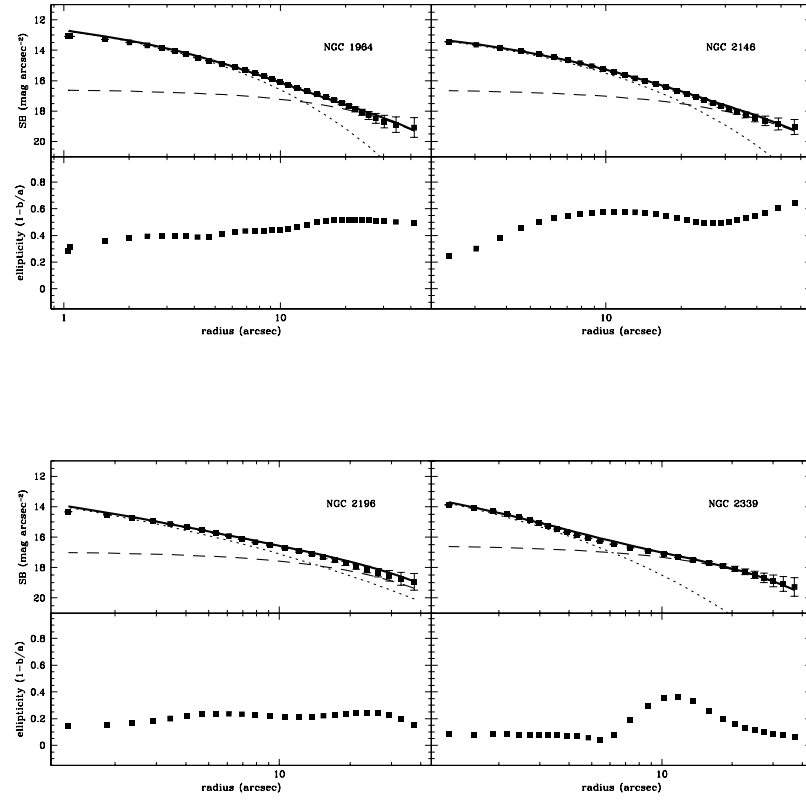


Figure 4.3: Same as figure 4.2.

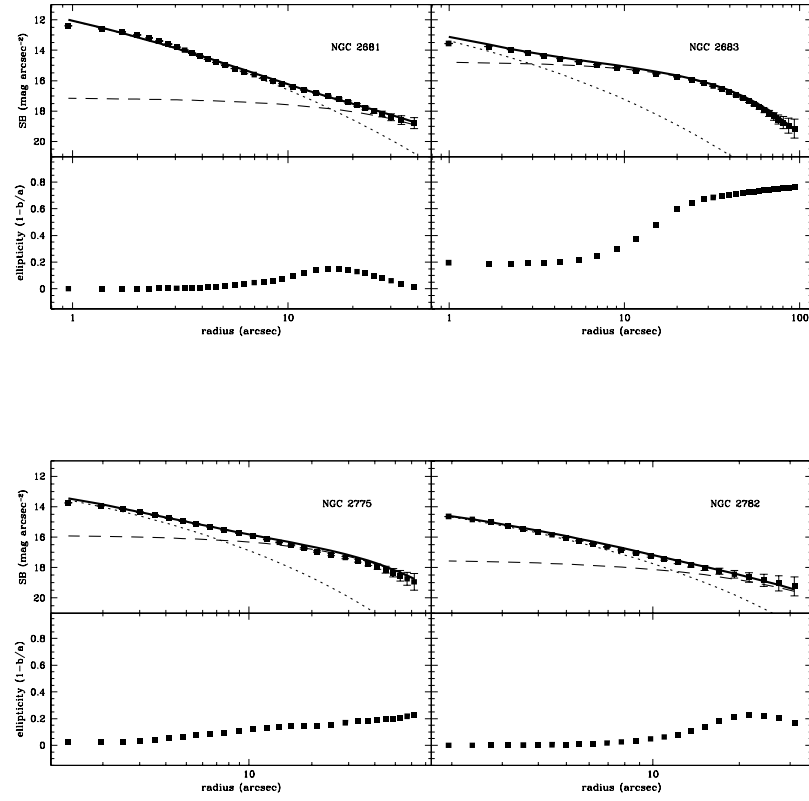


Figure 4.4: Same as figure 4.2.

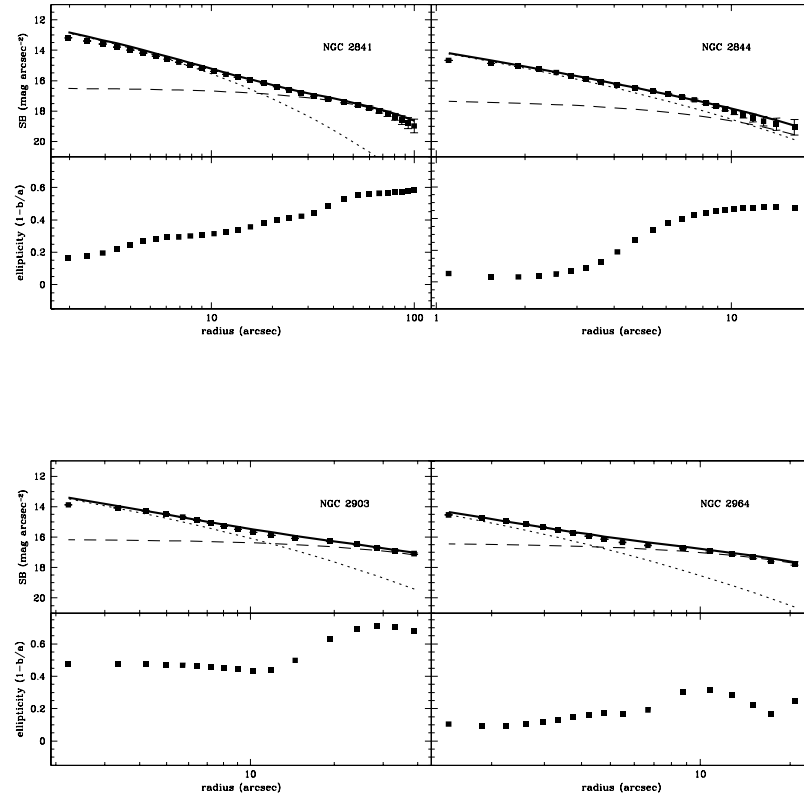


Figure 4.5: Same as figure 4.2.

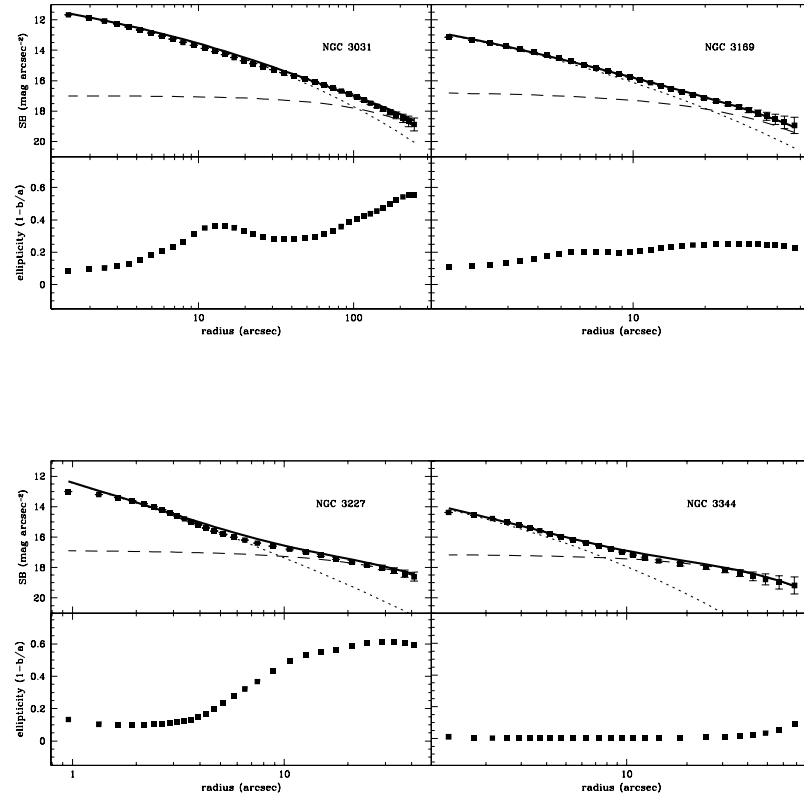


Figure 4.6: Same as figure 4.2.

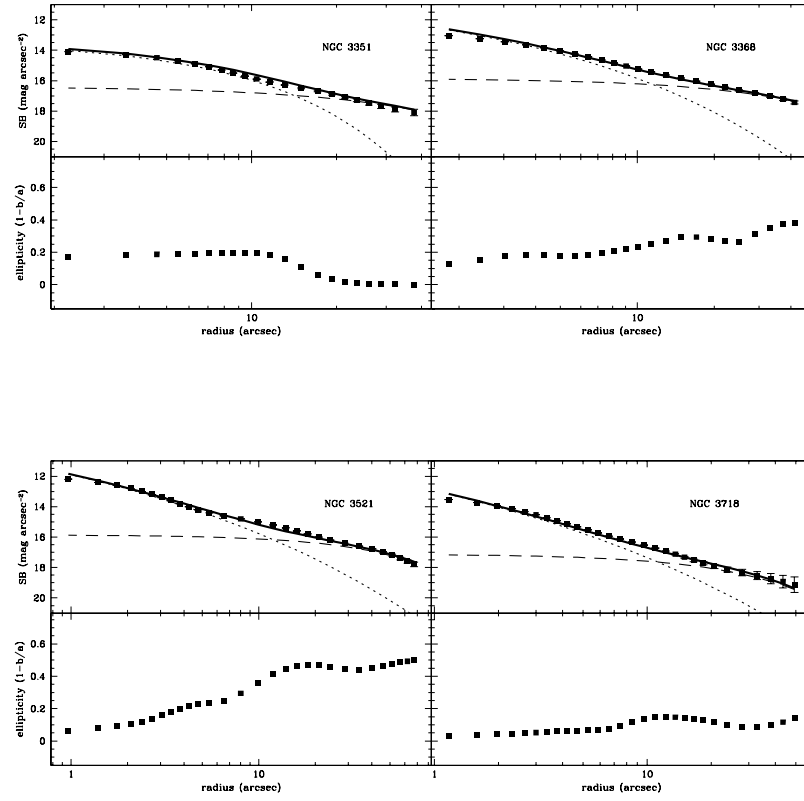


Figure 4.7: Same as figure 4.2.

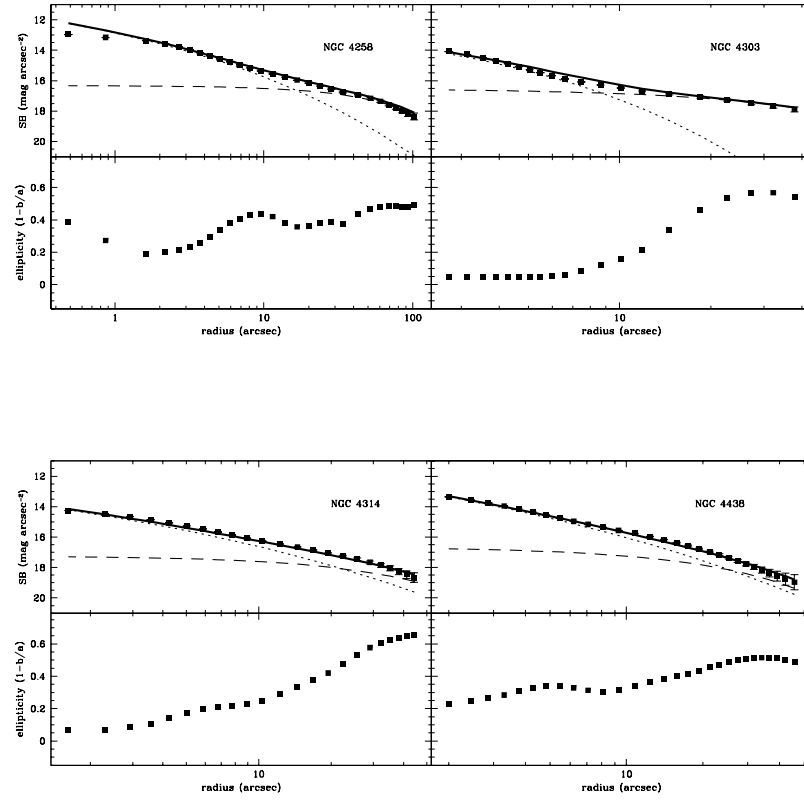


Figure 4.8: Same as figure 4.2.

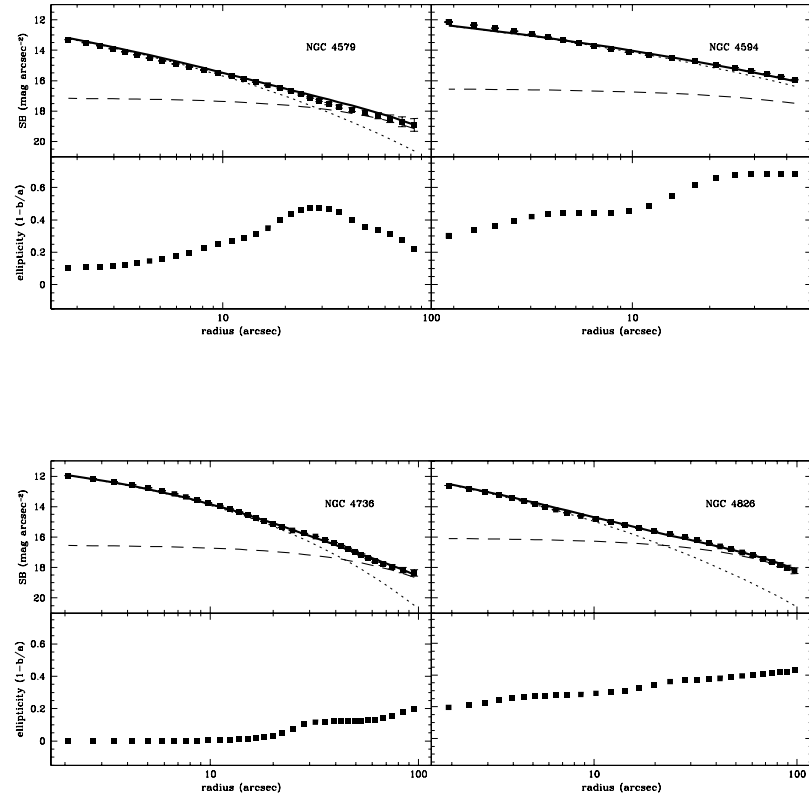


Figure 4.9: Same as figure 4.2.

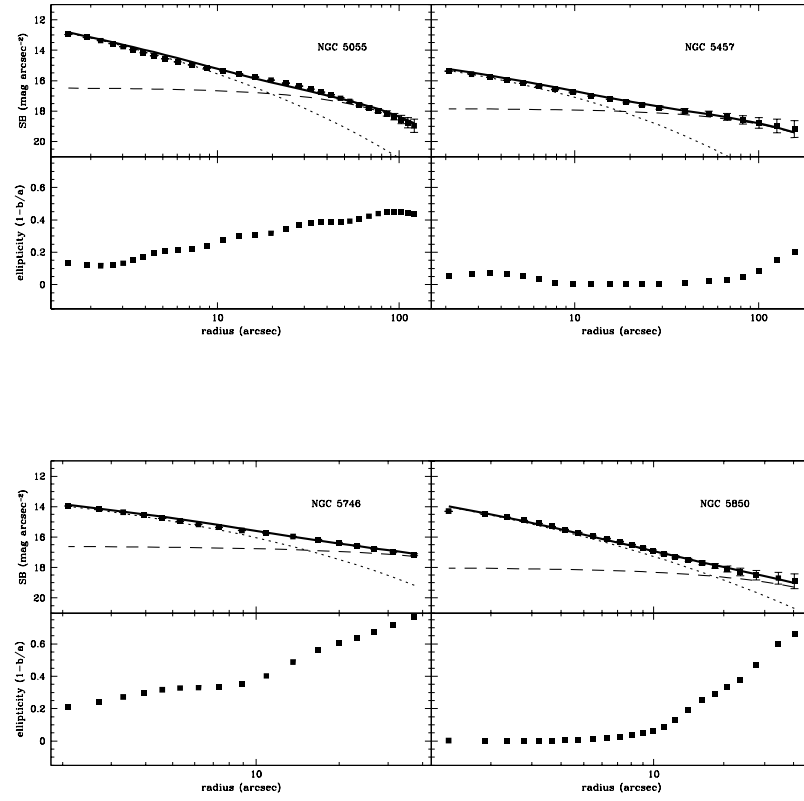


Figure 4.10: Same as figure 4.2.

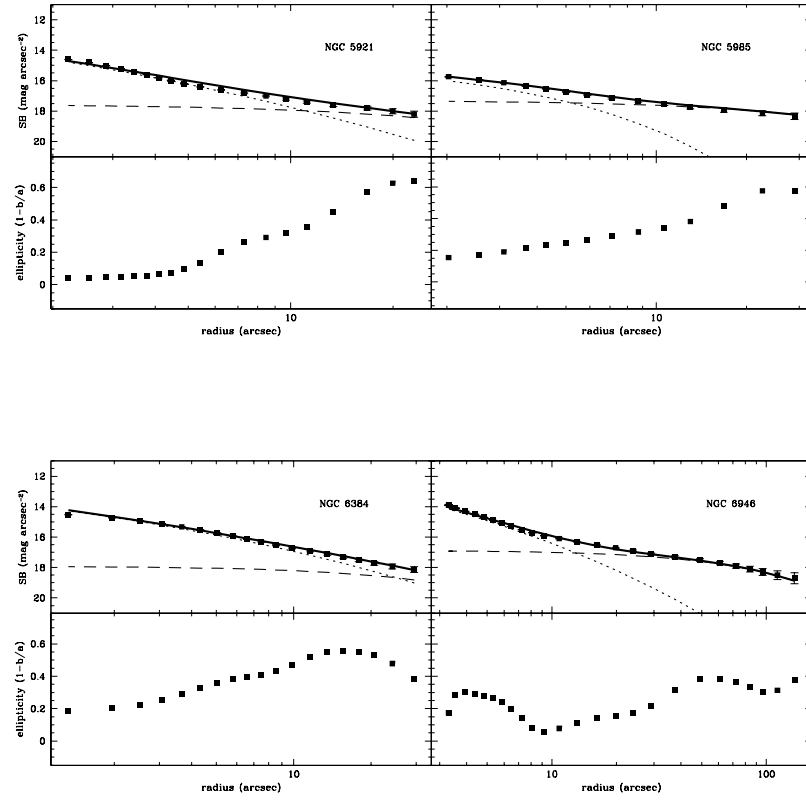


Figure 4.11: Same as figure 4.2.

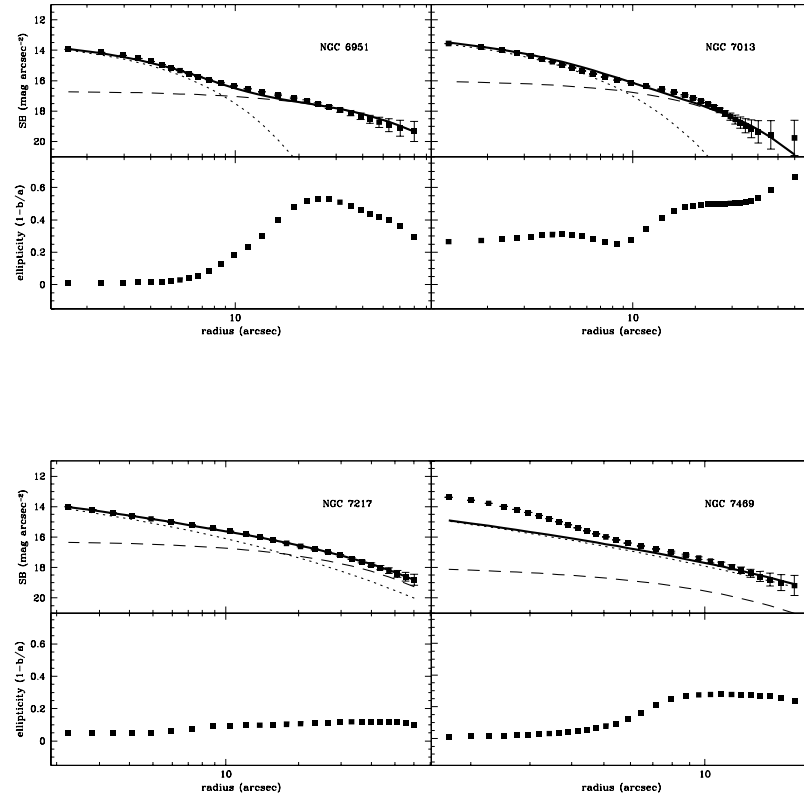


Figure 4.12: Same as figure 4.2.

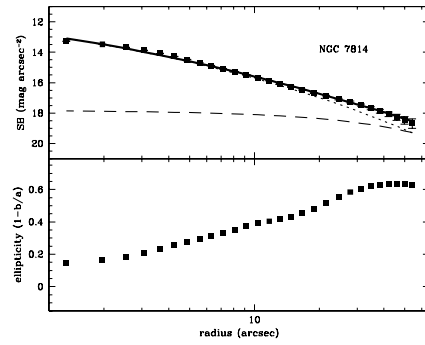


Figure 4.13: Same as figure 4.2.

The FWHM seeing varied between $2.5''$ and $3''$, good enough to measure the effective radii of the bulges of these nearby galaxies. About half of these galaxies are classified as Seyfert and/or LINER galaxies; it is possible that the surface brightness profile is significantly affected by light from the AGN. We tested this by fitting a three-component model (disk, bulge, and unresolved source) to the images of the AGN galaxies and find no significant change in the fitted bulge or disk quantities. The one exception is NGC 7469, which is dominated by an unresolved source within the central few arcseconds. For this galaxy, we include an unresolved source in the GALFIT procedure along with the bulge and disk component.

Table 4.3 includes the bulge effective radius in arcseconds, the bulge effective radius in kiloparsecs calculated using the distance from Table 4.1, and the bulge effective surface brightness (calculated using the bulge m_K from Table 4.2 and r_{eff}).

4.2.3 Kinematic Observations

Spectroscopic observations presented in this paper were taken during 54 nights in twelve observing runs between December 2000 and April 2004 at McDonald Observatory and during a three-night run in April 2004 at the NASA Infrared Telescope Facility (IRTF). We utilize the $2.29\ \mu\text{m}$ (2-0) ^{12}CO absorption bandhead from evolved red stars to measure the stellar kinematics in our sample. This feature is in a dark part of the infrared sky spectrum and is intrinsically sharp and deep, making it very sensitive to stellar motions (Lester & Gaffney 1994). It is located in an optimal range for studying stellar kinematics where wavelengths are long enough to minimize extinction from dust but short enough to avoid emission from hot dust (Gaffney et al. 1995). Silge & Gebhardt (2003) present a detailed calibration of stellar kinematics measured using the CO bandhead.

At McDonald Observatory, we use CoolSpec (Lester et al. 2000), a near-infrared grating spectrometer, on the 2.7-m telescope. CoolSpec has a 256×256

HgCdTe NICMOS III detector array with a spatial scale of $0''.35 \text{ pixel}^{-1}$. Using a 240 l/mm grating and $1.8'' \times 90''$ slit, our spectral resolution is 2300, measured from calibration lamp lines. With this resolution, we can study galaxies with velocity dispersions down to approximately 50 km s^{-1} . Resolving the dispersions of the early-type galaxies presented here is easily within reach of this observational set-up. The spectral scale is $24.6 \text{ km s}^{-1} \text{ pixel}^{-1}$ and the spectral range is just under $0.05 \mu\text{m}$, large enough to provide good coverage of the first CO bandhead and continuum on both sides.

At the IRTF, we use SpeX (Rayner et al. 2003), another medium-resolution near-IR spectrograph. SpeX has a Raytheon 1024×1024 InSb array with a spatial scale of $0''.15 \text{ pixel}^{-1}$. Using the $0''.30 \times 60''$ slit in single-order long-slit mode, we obtain spectral resolution of 2000, measured from calibration lamp lines. The spectral range of SpeX is much larger than that of CoolSpec; use an order-sorting filter, we obtain the spectrum from $1.96 \mu\text{m}$ to $2.52 \mu\text{m}$ with a spectral scale of $\sim 70 \text{ km s}^{-1} \text{ pixel}^{-1}$. With this spectral range, we can use several of the CO bandheads for the kinematic fitting.

We observe A dwarfs, which have nearly featureless spectra in this region (Wallace & Hinkle 1997), along with the galaxies to obtain the shape of the telluric absorption spectrum. Silge & Gebhardt (2003) present more details on this aspect of the observations, explaining why it is very important to take a careful (and frequent) measure of this spectral shape, particularly at McDonald using CoolSpec. We choose A dwarfs spatially near each galaxy and observe one before and after (and sometimes in the middle of) each galaxy observation. The observations are made by dithering the object across the slit to measure the sky at the same slit position in alternating exposures. Individual exposures are 120 seconds for the galaxies and ten seconds for the stars. Total integration times for the galaxies vary from about one hour to almost five hours. Galaxies that require very long integration times or that

are at low declinations are observed during several nights to maintain reasonable airmasses. The slit is rotated to the position angle of the galaxy major axis as quoted in the RC3. Ar and Ne emission lamps calibrate the wavelengths of the exposures; at McDonald, calibration exposures are taken every 24 minutes because we find the wavelength solution drifts significantly with time. The telescope guides on either the galaxy itself or a nearby star (if available) using the optical dichroic mirror autoguider at McDonald. At the IRTF, the autoguider uses spillover near-IR light from the slit. No attempt is made to flux calibrate the spectra since we are mainly concerned with the kinematic analysis.

4.2.4 Data Reduction

Data reduction proceeds as described in Silge & Gebhardt (2003), in generally the same manner for both the McDonald and IRTF data; we more briefly describe the process here. We rectify the images in the spectral direction using the arc lamp lines and subtract an additive constant measured in each individual exposure. We make background images for groups of exposures and subtract them, then shift all the images to the same wavelength solution. The images are then shifted in the spatial direction so that the center of the galaxy in each image is aligned; we calculate the biweight (Beers et al. 1990) of all the processed images to make one image for the galaxy. The one-dimensional spectra are extracted from the two-dimensional images for basically the entire galaxy; we choose the number of columns to extract to maximize signal-to-noise. This varies between $3''$ and $20''$; the extraction windows are presented in Table 4.3. The extraction windows are $\leq r_{eff}$ of the bulge for most galaxies, and less than the radius where the bulge dominates the light for all the galaxies. Thus our kinematic measurements reflect the dynamics of the bulge only and are not significantly contaminated by disk light. The stellar spectra are reduced in a similar manner.

To remove the telluric absorption spectrum, the galaxy spectra must be divided by a “flat” spectrum, obtained from the A dwarfs. We obtain the best results by averaging together all the A dwarf spectra from a run to make a smooth, high S/N sky spectrum. Dividing by only an individual A star does not give results as good as the smooth sky spectrum made from many A stars because of the fluctuations in the individual spectra. The galaxy spectra are taken over long periods of time (1 hour) which average over many such fluctuations while each individual A dwarf spectra takes a very short time (~ 1 minute). These individual stars change because of fluctuations in the sky, not because of problems with S/N; telluric absorption is removed from the galaxies better when we divide by a “master” A dwarf spectrum.

4.2.5 Extracting the Velocity Distribution

Once we have the spectrum for each galaxy, we extract the kinematic information from it. A galaxy spectrum is the convolution of the line-of-sight velocity distribution (LOSVD) with an average stellar spectrum. There are several techniques used to obtain the internal kinematic information from a galaxy spectrum, such as the cross-correlation technique and the Fourier quotient technique (Tonry & Davis 1979; Sargent et al. 1977). We use the fitting technique of Gebhardt et al. (2000c), deconvolving the spectrum directly in pixel space using a maximum penalized likelihood estimate to obtain a nonparametric LOSVD. An initial velocity profile is chosen and this profile is convolved with a stellar template spectrum. The residuals to the galaxy spectrum are calculated and the velocity profile is changed to minimize the residuals and provide the closest match to the observed galaxy spectrum.

The choice of template star proves to be important for the fitting results (Silge & Gebhardt 2003). We find that the dispersion measured by the fitting program depends on the template spectrum chosen for the fitting, so we give the fitting program a variety of template stellar spectra and allow it to vary the weights

given to the different stars to obtain the best fit. As a result, along with the LOSVD information, the fitting program also provides stellar population information. We use the near-IR stellar spectral atlas of Wallace & Hinkle (1997) as our templates, choosing eight stars with CO equivalent widths ranging from less than 5 Å to over 20 Å. These spectra have a somewhat higher spectral resolution than either the McDonald or IRTF observations, so before using them as stellar templates we have carefully convolved them to the relevant spectral resolution. The best fit almost always gives most of the weight to a few of the template stars.

Most LOSVD fitting techniques make some assumption about the shape of the LOSVD, i.e. it is Gaussian or a Gauss-Hermite polynomial. Our technique obtains a nonparametric LOSVD; no a priori assumptions about the shape of the LOSVD are made except that it is nonnegative in all bins. To measure a dispersion from this nonparametric LOSVD, we fit a Gauss-Hermite polynomial to it and use the second moment as the dispersion. Some of the galaxies in this sample with the lowest S/N ratios required the assumption of a Gaussian LOSVD in order to achieve a sensible velocity distribution. We compared the derived nonparametric and Gaussian LOSVDs for galaxies with higher S/N and found good agreement between them. Figures 4.14 and 4.15 show the results for all 45 sample galaxies and the derived velocity dispersion for each galaxy. The noisy line is the observed spectrum for each galaxy and the smooth line is the template stellar spectrum convolved with the derived LOSVD.

The spectrum of NGC 7469 is contaminated by emission from the central AGN, just as its *K*-band surface brightness profile has a significant contribution from the AGN. The CO bandheads are somewhat filled in by this emission; since this region is sensitive to template mismatch (Silge & Gebhardt 2003), we must remove the AGN emission from the spectrum to recover accurate stellar kinematics. The chapter on Centaurus A illustrates a similar approach. Since we do not know

the true equivalent width of the CO bandhead in this galaxy, we have chosen to take a “typical” equivalent width as seen in our sample as a whole for NGC 7469. Our velocity dispersion may thus be biased low or high by our assumption about the true equivalent width. Depending on the actual equivalent width, the velocity dispersion may be biased up to $\sim 20 \text{ km s}^{-1}$, about twice the uncertainty we quote. This uncertainty does not affect any of our conclusions; the FP fits do not change if we exclude NGC 7469 from our sample.

We determine the uncertainties for the velocity dispersions using the Monte Carlo bootstrap approach of Gebhardt et al. (2000c). The initial fit to the observed galaxy spectrum is used to generate 100 simulated spectra with noise chosen to match that of the observed spectrum. These 100 synthetic galaxy spectra are then deconvolved to determine their LOSVDs in the same way the original observed spectrum is deconvolved. These LOSVDs provide a distribution of values for each velocity bin which allows us to estimate the uncertainty and examine any bias in the dispersion. The median of the distribution determines any potential bias from the initial fit, and the spread of the distribution determines the uncertainty. In order to generate the 68% confidence bands, we choose the 16% to 84% values from the 100 realizations. Using this technique and spectral feature, we find 10% accuracy in the velocity dispersion requires S/N per pixel of about 25 or 30. Table 4.3 includes the velocity dispersions and uncertainties for our sample galaxies, along with CO bandhead equivalent widths calculated as described in Silge & Gebhardt (2003). We do not report an equivalent width for NGC 7469 since we have assumed some typical value for this galaxy to remove the AGN contribution to the spectrum.

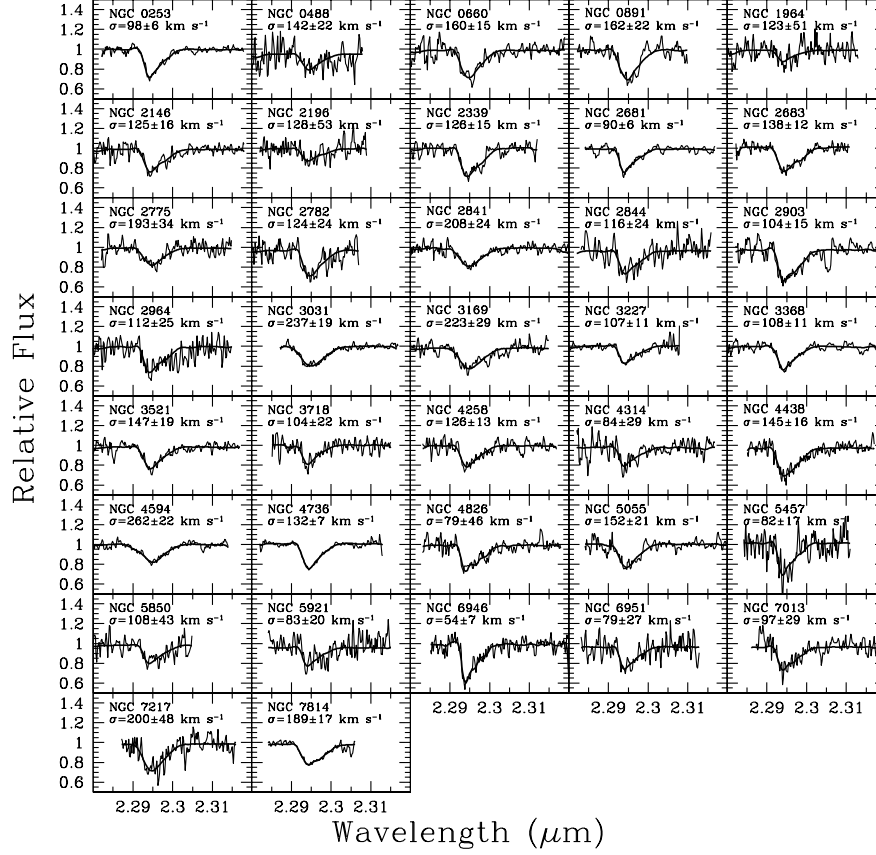


Figure 4.14: Rest-frame spectra for galaxies observed at McDonald Observatory (noisy line) and for the template stellar spectrum convolved with the derived LOSVD (smooth line). The derived velocity dispersion and its 68% uncertainty are reported for each galaxy.

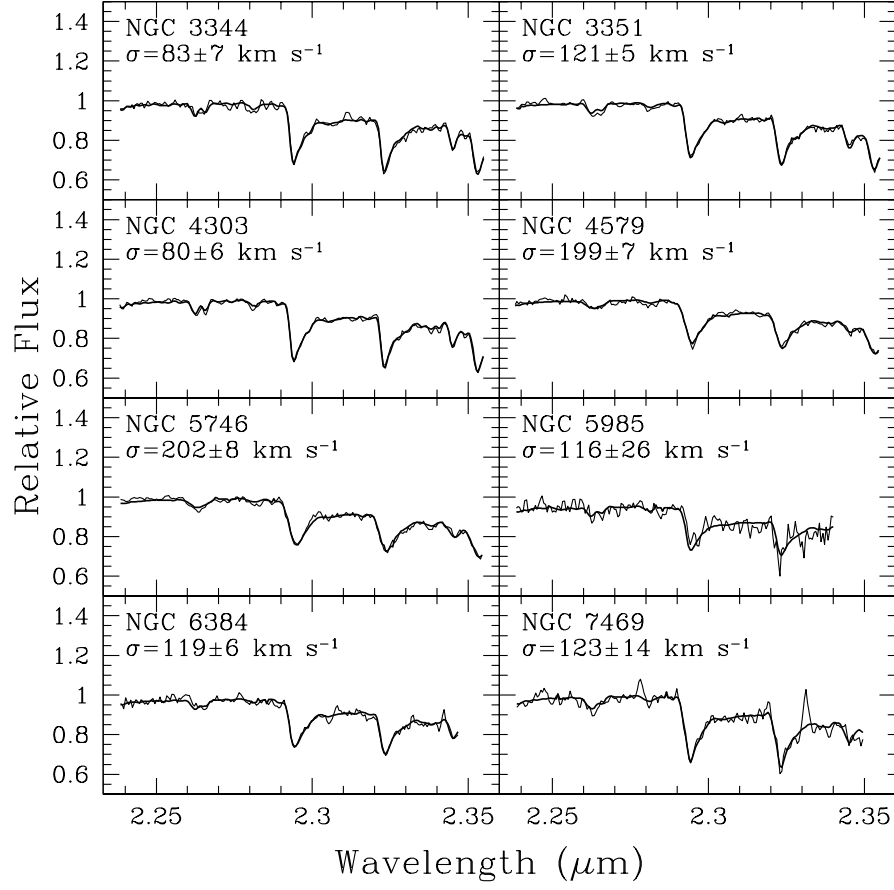


Figure 4.15: Same as figure 4.14 but for galaxies observed at IRTF.

4.3 Fitting the Fundamental Plane

The observed FP is defined by

$$\log r_{eff} = a \log \sigma + b \log I_{eff} + c$$

where the coefficients a , b , and c determine where the plane lies in the three-dimensional space made up of the observed parameters. These coefficients are found by minimizing the residuals from the plane for a given dataset. To minimize the scatter orthogonal to the plane, we take

$$\Delta \equiv \frac{\log r_{eff} - a \log \sigma - b \log I_{eff} - c}{(a^2 + b^2 + 1)^{1/2}}$$

and summing up Δ^2 over all the galaxies in the dataset, find the values of a , b , and c which minimizes the sum. In principle, this can be solved analytically but we choose instead to minimize this function numerically using the downhill simplex method.

For the 45 spiral galaxies in this sample, we find

$$a = 1.94 \pm 0.12, b = -0.51 \pm 0.09, c = -7.41 \pm 0.58.$$

Figure 4.16 presents these FP results. The starred symbols are the bulge galaxies of this sample. The open circles are lenticular galaxies and the open squares are elliptical galaxies from the previous chapter and Silge & Gebhardt (2005). The error bars in the lower right-hand corner show typical sizes of uncertainties for these galaxies; the velocity dispersion uncertainties dominate over the photometric uncertainties. The heavy dashed line is the projection of our FP for the bulges in these coordinates. The small points are from a comparison sample based on Bernardi et al. (2003a) using K -band photometry and optical kinematics as detailed in the

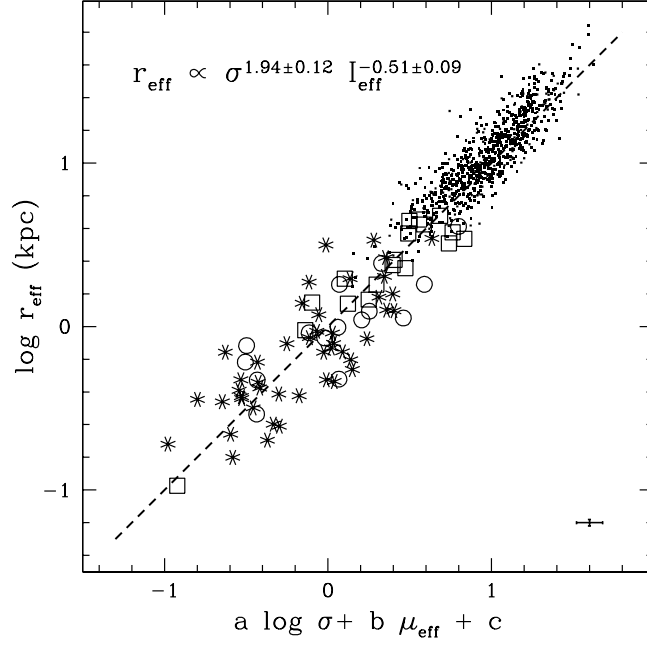


Figure 4.16: The infrared Fundamental Plane of bulges. The best-fit FP coefficients for the bulges (starred symbols) are shown; the heavy dashed line is the projection of that FP in this plot. The open circles are S0s and the open squares are Es from Silge & Gebhardt (2005). The error bars in the lower right-hand corner show typical sizes of uncertainties for these galaxies. The small points are from the sample of Bernardi et al. (2003a) using K -band photometric data, as detailed in Silge & Gebhardt (2005).

previous chapter and Silge & Gebhardt (2005). The intrinsic scatter, measured by subtracting the measurements errors in quadrature from the observed scatter, around this fit is 0.088.

Plotting the three observed quantities (r_{eff} , I_{eff} , and σ) shows us three projections of the FP. Figure 4.17 does just that; panel (b) is the projection closest to edge-on and also the Kormendy relation, panel (c) is the projection closest to edge-on, and panel (a) is intermediate. The symbols in these plots are the same as in Figure 4.16. Another important scaling relation is the Faber-Jackson relation,

the correlation between total luminosity and velocity dispersion (Faber & Jackson 1976). This scaling relation has been found to be $L \propto \sigma^4$ for elliptical galaxies. Figure 4.18 shows this correlation for these galaxies; again, the symbols are the same as in Figure 4.16. The solid line shows the slope of $L \propto \sigma^4$ in this plot; the data are roughly consistent with such a relationship. For the later-type galaxies (starred symbols) in this plot, the total luminosity is for the bulge only; plotted here is the absolute K magnitude of the bulge component, not the entire galaxy.

We can also examine differences within this bulge sample. Figure 4.19 shows the location in the FP plot of each bulge in the sample colored according to the morphological type of the host galaxy. In this plot, red symbols represent S0/a or Sa galaxies, orange symbols represent Sab galaxies, green symbols represent Sb galaxies, blue symbols show Sbc galaxies, and violet symbols show Sc, Scd, and Sd galaxies. Figure 4.20 shows the location of bulges on the FP colored according to their barred status. Magenta symbols represent unbarred galaxies, violet symbols present barred galaxies, and teal symbols show galaxies which are intermediate. In both of these plots, no clear dependencies on type or barred status emerge. The number of galaxies in each morphological bin is small (≤ 10) so this is not surprising. An important fact to keep in mind here is that galaxy characteristics such as morphological type and bar status depend on the wavelength at which one makes this determination (Jarrett et al. 2003); the morphological types used here are from the RC3, which is based on B -band images.

4.4 Discussion

All our FP results for the samples presented in Chapters 3 and 4 are presented in Table 4.4. Our finding for the bulges of $a = 1.94 \pm 0.12$, $b = -0.51 \pm 0.09$ is significantly different from previous results on the FP of bulges. Moriondo et al. (1999) find $a = 0.97 \pm 0.13$, $b = -0.61 \pm 0.08$; a is different at the 8σ level. Moriondo

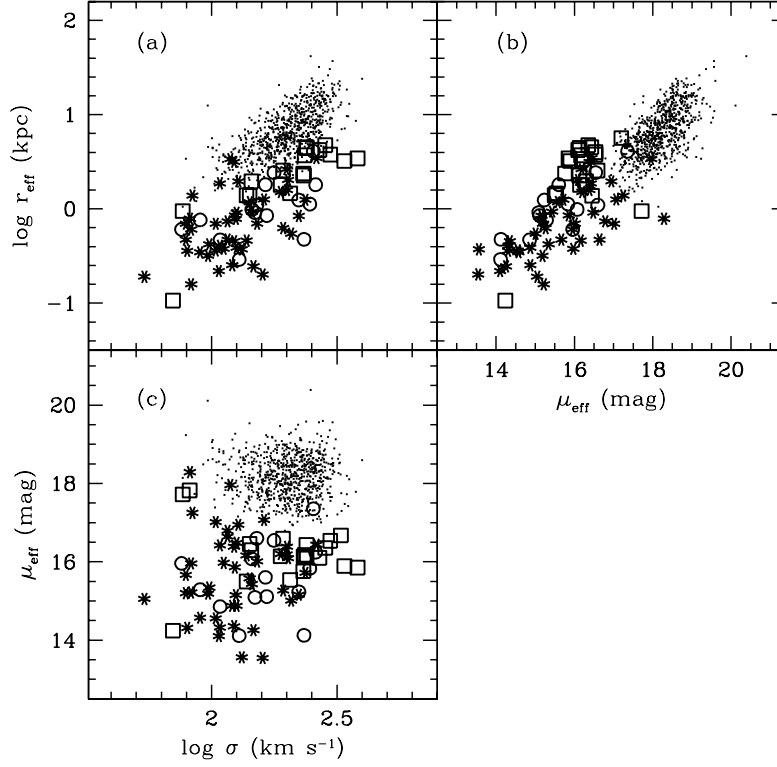


Figure 4.17: The three projections of the FP viewed in the coordinates of the observed quantities. The symbols are the same as in Figure 4.16. Panel (b) shows the projection closest to edge-on (which is also the Kormendy relation), panel (c) shows the projection closest to face-on, and panel (a) is intermediate.

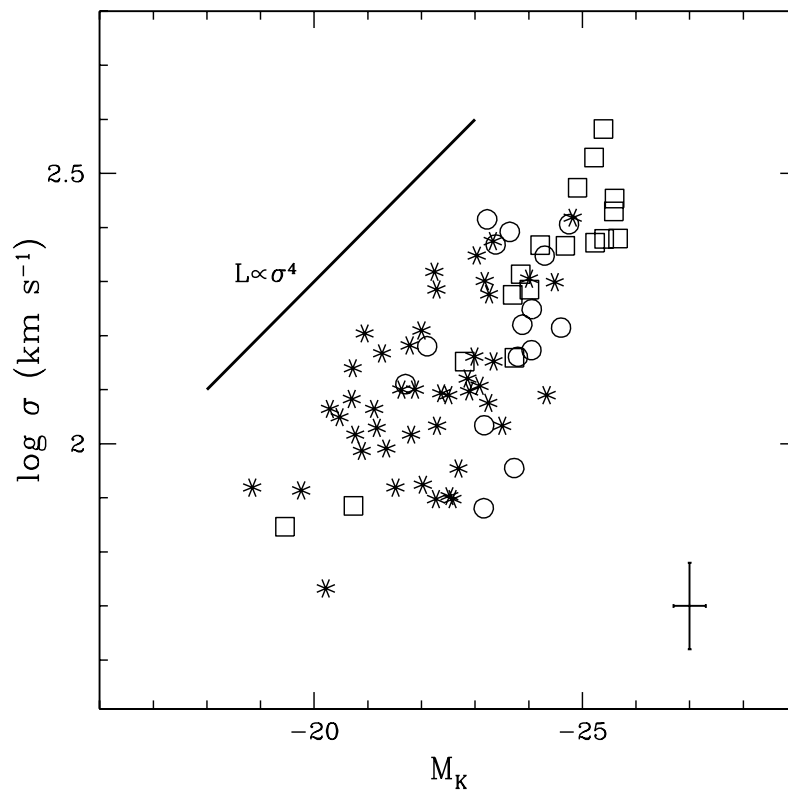


Figure 4.18: The Faber-Jackson relation. The open circles are S0s and the open squares are Es from Silge & Gebhardt (2005), and the starred symbols are bulges from this chapter. The error bars in the lower right-hand corner show typical sizes of uncertainties for these galaxies. The solid line shows the slope of $L \propto \sigma^4$ in this plot.

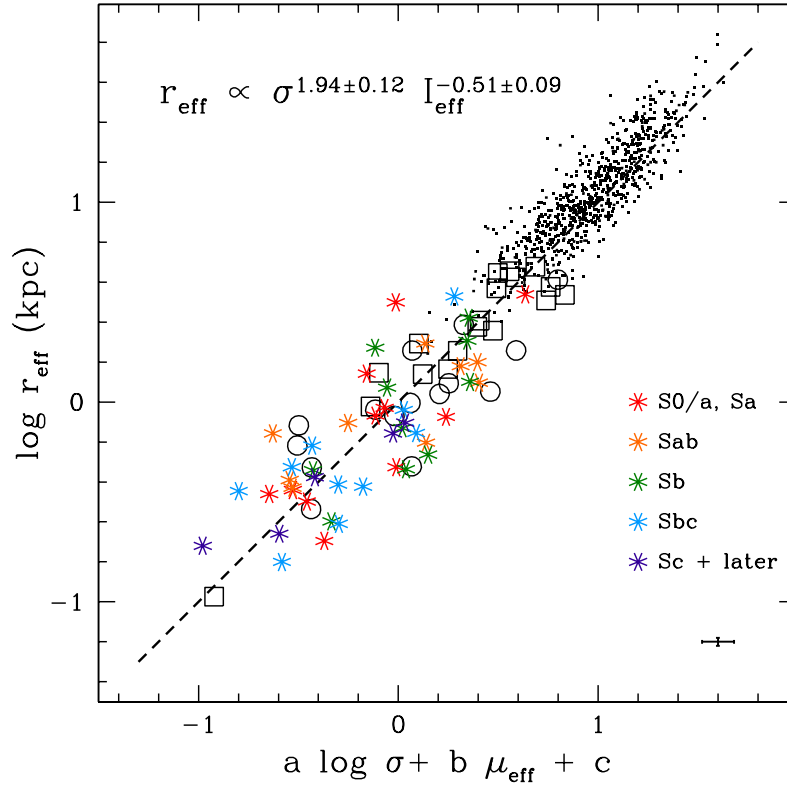


Figure 4.19: Same as Figure 4.16, but showing differences between the bulge sample by morphological type. Red symbols represent S0/a or Sa galaxies, orange symbols represent Sab galaxies, green symbols represent Sb galaxies, blue symbols show Sbc galaxies, and violet symbols show Sc, Scd, and Sd galaxies.

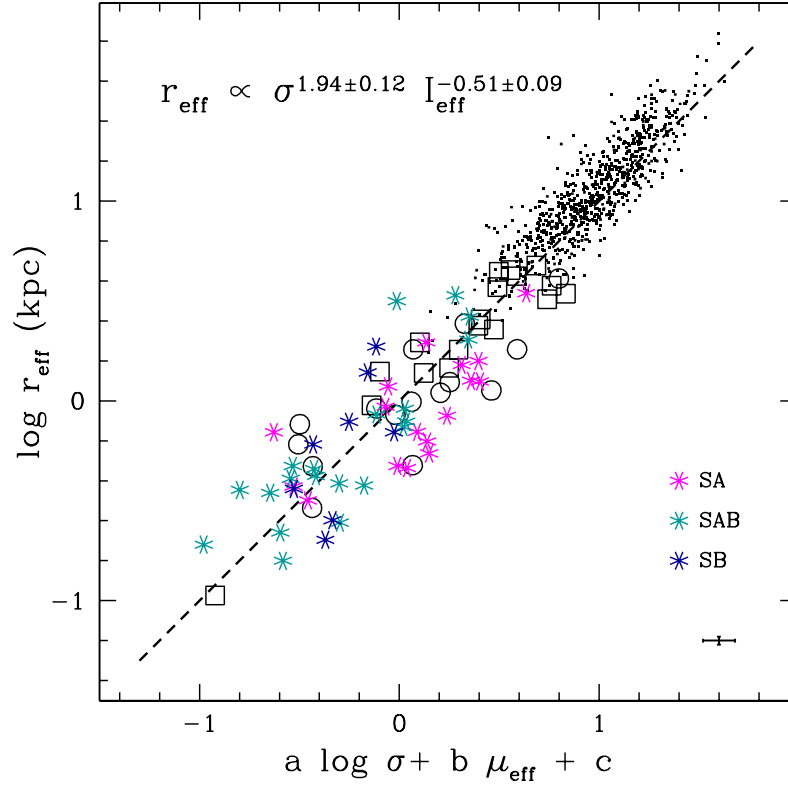


Figure 4.20: Same as Figure 4.16, but showing differences between barred, unbarred, and intermediate galaxies. Magenta symbols represent unbarred galaxies, violet symbols present barred galaxies, and teal symbols show galaxies which are intermediate.

et al. (1999) perform their bulge/disk decompositions on H -band images, which may still be dust-affected enough to bias their measurements of the photometric characteristics of the bulges. More likely, though, their kinematic measurements are affected. They use rotation curves based on optical emission lines, i.e. gas in the disk. Depending on how the relationship between disk gas rotation and stellar kinematics in the bulge depends on luminosity (or mass), this observational choice could explain the difference between our results.

Our result also differs from the main conclusion of Falc3n-Barroso et al. (2002). These authors do not fit a FP to their bulges only, but rather fit to a larger sample including both elliptical galaxies and bulge galaxies and then examine the dependence of residuals with galaxy type, etc. They find that the bulges lie below the FP defined by elliptical galaxies, at a 2σ level. This would imply that bulges are slightly brighter than otherwise analogous elliptical galaxies. We do not find such a result. The coefficient c , which represents the zero-point of the FP, is -7.44 ± 0.33 for our sample of early-type galaxies in the previous chapter and -7.41 ± 0.58 for the bulge galaxies. This is illustrated in Figure 4.16, where the bulge galaxies obviously lie in the same region of space as the early-type galaxies. Our study uses K -band light; we could explain this difference if Falc3n-Barroso et al. (2002) used optical light by invoking dust and stellar population variation. Spiral galaxies have more dust and more recent star formation and thus may be separated from elliptical galaxies in the three-dimensional FP space in the B -band and not separated in the K -band. However, Falc3n-Barroso et al. (2002) find that bulges are slightly lower than ellipticals using both B -band and K -band photometry; they find a 2σ shift in both bands. This is not consistent with our result. Only one galaxy, the S0 pec galaxy NGC 7332 is in common between our samples, and we include it in our early-type sample of the previous chapter. The kinematic measurements of Falc3n-Barroso et al. (2002) are not likely the source of the problem; they are Ca II

triplet measurements that are aperture corrected.

We find that the bulges basically lie in the same place of the three-dimensional FP space as our early-type galaxies, but we do find a moderate difference in the slope of the FP of bulges compared to the FP of early-type galaxies. For the early-type galaxies, we find $a = 1.72 \pm 0.09$, $b = -0.62 \pm 0.06$; a is different at the 2σ level. These coefficients are also significantly different from optical FPs of Es. Our value for a is very close to the virial prediction of $a = 2$ while our value for b is half of that predicted by the virial theorem ($b = 1$). Differences from the simple virial prediction can be attributed to systematic variation of M/L ratio with luminosity and/or breakdown of dynamical homology. The difference between the E and bulge FPs means that these relationships are not the same for elliptical galaxies as for bulges. For instance, this result could be explained by the change in the kinematic profile with luminosity (i.e. breakdown of dynamical homology) for elliptical galaxies being different from that for spiral galaxies. Or, for another example, if the difference from the virial prediction is all due to M/L variation, then our result would indicate $M/L \propto L^\gamma$, with a different value for γ for early-type galaxies than for bulge galaxies. The evidence for early-type galaxies is that both effects are at work; for spiral galaxies, we would like to understand nonhomology through spatially resolved kinematics and M/L variation through such studies as Drory et al. (2004) and Kauffmann et al. (2003).

One conclusion we can draw is that at least some bulges are distinct from elliptical galaxies; they are not merely Es that happen to live inside a disk. The differences discussed in the previous paragraph indicate that there are moderate structural and/or population differences. This can serve as further evidence that some fraction of bulges form through a separate process from pure E galaxies as argued by Kormendy & Kennicutt (2004). Further study can indicate if the differences between elliptical and bulge FPs are consistent with an important role for

secular evolution in bulge formation.

We find a small amount of intrinsic scatter ($\text{rms} = 0.088$) in our FP of bulges. This is a somewhat larger amount of scatter than that found for FPs of early-type galaxies ($\text{rms} = 0.069$ in the previous chapter). For early-type galaxies, the scatter is not controlled by age and metallicity effects (Pahre et al. 1998) but does appear to depend on environment (Bernardi et al. 2003b). The scatter of the early-type FP also does not change much with observed passband, indicating that galaxy-to-galaxy differences in dust and stellar population content are not the driving force behind the scatter. None of the previous results on the FP of bulges report intrinsic scatter so we cannot examine the behavior of the scatter with observed passband, environment, etc. None of the galaxies in our sample sample even moderately dense regions of the universe; our sample can be considered a field sample and we cannot examine the environmental aspects of the scatter within our sample. We can, however, note the increase of scatter as we move from early-type to late-type galaxies. This does fit in well with our pictures of bulges as more heterogeneous objects than elliptical galaxies. This could be explained by bulges being more nonhomologous than elliptical galaxies, or by having enough variation in relative dust content or star formation history to increase the scatter. Measuring spatially resolved kinematics of a sample of bulge galaxies could address the first question, and having the detailed mid-IR and far-IR observations that Spitzer will provide for local galaxies can help address the second question. The distances to these bulges are based on the Virgo-centric flow model (instead of surface brightness fluctuations, as in the case of the early-type galaxies of the previous chapter) and thus are less certain, so the increased scatter could also be due to increased distance errors.

4.5 Conclusions

In this project, we have built an all-infrared FP of late-type galaxies, using both near-IR imaging and kinematics. We have observed 45 nearby bulge galaxies and measured their stellar kinematics using the $2.29\mu\text{m}$ (2-0) ^{12}CO absorption band-head, combining these new measurements with published 2MASS K -band photometric quantities for these galaxies to examine the tight relationship among the structural and kinematic properties of galaxies known as the FP. This technique allows us to effectively deal with such problems as dust extinction, effects of recent star formation, and sample bias. We find a FP relationship of

$$r_{eff} \propto \sigma^{1.94 \pm 0.12} I_{eff}^{-0.51 \pm 0.09}.$$

This result is moderately different from FP relationships for early-type galaxies, indicating that bulges are distinct from elliptical galaxies with different structural and/or population characteristics. It is significantly different from previous results on the FP of bulges (Moriondo et al. 1999; Falc3n-Barroso et al. 2002), most likely due to the difficulty of studying bulges with their techniques. It is because of these difficulties that utilizing near-IR kinematics holds such promise in expanding our detailed knowledge of bulge galaxies.

Table 4.1: Basic properties of bulge galaxies

Galaxy	Type	v (km s ⁻¹)	$(m - M)^1$ (mag)	D (Mpc)	M_K^2 (mag)
NGC 253	SAB(s)c	243	—	2.929	-23.56
NGC 488	SA(r)b	2272	—	26.379	-25.14
NGC 660	SB(s)a pec	850	—	11.122	-22.89
NGC 891	SA(s)b	528	29.61±0.14	8.356	-23.67
NGC 1964	SAB(s)b	1659	—	18.216	-23.62
NGC 2146	SB(s)ab pec	893	—	14.792	-23.79
NGC 2196	(R')SA(rs)ab	2321	—	25.500	-23.90
NGC 2339	SAB(rs)bc	2206	—	27.111	-23.66
NGC 2681	(R')SAB(rs)0/a Sy	692	31.18±0.34	17.219	-23.75
NGC 2683	SA(rs)b Sy2,LINER	411	29.44±0.36	7.727	-23.11
NGC 2775	SA(r)ab	1354	—	16.142	-24.00
NGC 2782	SAB(rs)a Sy1	2562	—	33.235	-23.74
NGC 2841	SA(r)b Sy1,LINER	638	—	9.688	-23.87
NGC 2844	SA(r)a	1486	—	21.205	-21.74
NGC 2903	SB(s)d	556	—	5.824	-22.79
NGC 2964	SAB(r)bc	1328	—	18.831	-23.02
NGC 3031	SA(s)ab Sy1.8,LINER	-34	27.96±0.26	3.908	-24.13
NGC 3169	SA(s)a pec	1238	—	14.936	-23.59
NGC 3227	SAB(s) pec Sy1.5	1157	—	14.492	-23.17
NGC 3344	(R)SAB(r)bc	586	—	5.507	-21.27
NGC 3351	SB(r)b	778	—	6.855	-22.52
NGC 3368	SAB(rs)ab Sy,LINER	897	30.08±0.20	10.375	-23.76
NGC 3521	SAB(rs)bc	801	—	6.410	-23.25
NGC 3718	SB(s)a pec Sy1,LINER	993	—	15.679	-23.22
NGC 4258	SAB(s)bc Sy1.9,LINER	448	29.31±0.14	7.278	-23.85
NGC 4303	SAB(rs)bc Sy2	1566	—	23.917	-25.05
NGC 4314	SB(rs)a LINER	963	—	10.356	-22.62
NGC 4438	SA(s)0/a pec LINER	71	—	16.5	-23.82
NGC 4579	SAB(rs)b Sy1.9,LINER	1519	—	24.268	-25.44
NGC 4594	SA(s)a Sy1.9,LINER	1024	29.95±0.18	9.772	-24.99
NGC 4736	(R)SA(r)ab Sy2,LINER	308	28.58±0.18	5.200	-23.47
NGC 4826	(R)SA(rs)ab Sy2	408	29.37±0.20	7.482	-24.04
NGC 5055	SA(rs)bc LINER	504	—	6.605	-23.49
NGC 5457	SAB(rs)cd	241	—	4.827	-22.91
NGC 5746	SAB(rs)b	1724	—	25.526	-25.16
NGC 5850	SB(r)b	2556	—	32.726	-24.47
NGC 5921	SB(r)bc LINER	1480	—	20.570	-23.47
NGC 5985	SAB(r)b Sy1,LINER	2517	—	34.346	-24.53
NGC 6384	SAB(r)bc LINER	1665	—	23.730	-24.35
NGC 6946	SAB(rs)cd	48	—	4.911	-23.09
NGC 6951	SAB(rs)bc Sy2,LINER	1424	—	22.392	-24.53
NGC 7013	SA(r)0/a LINER	779	—	13.601	-22.95
NGC 7217	R)SA(r)ab Sy,LINER	952	—	14.860	-24.03
NGC 7469	(R')SAB(rs)a Sy1.2	4892	—	57.892	-24.97
NGC 7814	SA(S)ab LINER	1050	30.60±0.14	13.183	-23.52

References (1) from Tonry et al. (2001); (2) calculated using m_K from 2MASS LGA or XSC

Table 4.2: Disk/bulge decomposition parameters

galaxy	image source ¹	total bulge flux (mag)	r_{eff} (arcsec)	Sérsic n	bulge axis ratio	total disk flux (mag)	r_d (arcsec)	disk axis ratio	bulge/total ratio
NGC 253	LGA	5.99	29.63	4.00	0.58	3.93	149.64	0.26	0.13
NGC 488	LGA	8.76	9.23	3.01	0.86	7.20	35.19	0.78	0.19
NGC 660	LGA	9.29	3.74	1.60	0.53	7.63	18.91	0.30	0.18
NGC 891	LGA	7.61	31.14	1.70	0.89	6.08	98.97	0.08	0.20
NGC 1964	LGA	8.80	5.16	1.77	0.45	8.33	19.05	0.46	0.39
NGC 2146	LGA	7.96	10.95	1.65	0.40	7.78	25.17	0.50	0.46
NGC 2196	A	8.95	15.87	4.00	0.69	8.83	17.30	0.90	0.47
NGC 2339	A	10.54	2.94	2.48	0.65	8.76	13.62	0.84	0.16
NGC 2681	LGA	8.49	4.15	4.00	0.85	8.04	21.67	0.94	0.40
NGC 2683	LGA	8.72	12.31	3.92	0.90	6.28	45.22	0.26	0.10
NGC 2775	LGA	8.76	8.00	2.94	0.91	7.30	24.71	0.80	0.21
NGC 2782	A	10.24	5.31	2.18	0.76	9.20	14.72	0.80	0.28
NGC 2841	LGA	7.69	11.62	3.09	0.70	6.33	55.92	0.42	0.22
NGC 2844	A	11.34	4.59	4.00	0.73	10.33	7.91	0.49	0.28
NGC 2903	LGA	8.06	24.66	4.00	0.31	6.18	52.58	0.49	0.15
NGC 2964	A	10.90	4.13	4.00	0.82	8.36	16.97	0.78	0.09
NGC 3031	LGA	4.63	65.94	4.00	0.73	4.52	136.14	0.45	0.47
NGC 3169	LGA	7.84	11.63	3.66	0.66	8.23	25.94	0.69	0.59
NGC 3227	LGA	9.64	3.12	4.00	0.60	7.90	29.65	0.45	0.17
NGC 3344	LGA	9.86	5.93	3.76	0.68	7.54	36.69	0.87	0.11
NGC 3351	LGA	8.48	7.60	1.06	0.82	6.93	38.34	0.87	0.19
NGC 3368	LGA	7.79	8.09	2.12	0.75	6.67	31.65	0.64	0.26
NGC 3521	LGA	7.77	7.91	4.00	0.64	6.03	40.99	0.52	0.17
NGC 3718	A	9.17	4.77	4.00	0.84	8.22	22.95	0.85	0.29
NGC 4258	LGA	7.43	25.85	4.00	0.65	5.66	74.96	0.47	0.16
NGC 4303	LGA	9.37	4.09	1.78	0.85	6.95	36.40	0.79	0.10
NGC 4314	LGA	8.05	27.63	4.00	0.91	8.34	33.30	0.25	0.57
NGC 4438	LGA	8.10	11.69	4.00	0.65	8.08	18.46	0.48	0.50
NGC 4579	LGA	7.44	22.44	4.00	0.63	7.07	45.20	0.75	0.42
NGC 4594	LGA	5.13	73.01	4.00	0.67	6.35	54.94	0.13	0.75
NGC 4736	LGA	5.72	14.79	2.30	0.95	6.07	52.16	0.70	0.58
NGC 4826	LGA	6.79	19.20	4.00	0.73	5.67	52.36	0.55	0.26
NGC 5055	LGA	7.32	21.85	4.00	0.75	5.92	56.53	0.56	0.22
NGC 5457	LGA	8.66	33.67	2.97	0.67	5.56	117.28	0.88	0.05
NGC 5746	LGA	8.03	16.37	2.43	0.83	7.21	59.88	0.12	0.32
NGC 5850	LGA	9.07	11.78	4.00	0.84	8.74	37.67	0.33	0.42
NGC 5921	LGA	10.05	6.07	4.00	0.70	8.28	31.14	0.65	0.16
NGC 5985	LGA	11.56	4.44	1.30	0.59	8.14	35.20	0.50	0.04
NGC 6384	LGA	8.63	29.33	4.00	0.46	7.85	42.55	0.79	0.33
NGC 6946	LGA	8.24	8.01	4.00	0.81	5.37	90.53	0.76	0.07
NGC 6951	A	9.48	4.35	1.05	0.77	7.66	26.20	0.59	0.16
NGC 7013	A	9.78	4.82	1.28	0.55	7.97	15.98	0.56	0.16
NGC 7217	LGA	7.68	21.99	3.20	0.91	7.50	22.65	0.89	0.46
NGC 7469	LGA	9.14	11.24	4.00	0.77	10.58	6.34	0.33	0.79
NGC 7814	LGA	7.34	23.65	3.72	0.68	8.56	42.51	0.18	0.75

References: (1) LGA = Large Galaxy Atlas (Jarrett et al. 2003), A = 2MASS Atlas image;

Table 4.3: Properties of observed spectra and K -band Fundamental Plane quantities

Galaxy	Total Exposure Time (minutes)	S/N (pixel ⁻¹)	Extraction Window	σ (km s ⁻¹)	Equivalent Width (Å)	r_{eff} (arcsec)	r_{eff} (kpc)	μ_{eff} (mag)
NGC 253	72	28	1.8'' × 21.7''	98 ± 6	13.8 ± 0.38	29.63	0.421	15.34
NGC 488	192	12	1.8'' × 8.4''	142 ± 22	18.0 ± 1.5	9.23	1.180	15.58
NGC 660	144	17	1.8'' × 10.5''	160 ± 15	19.4 ± 1.0	3.74	0.202	13.55
NGC 891	192	16	1.8'' × 17.5''	162 ± 22	15.7 ± 1.2	31.14	1.262	17.07
NGC 1964	144	13	1.8'' × 15.4''	123 ± 51	5.1 ± 1.4	5.16	0.456	14.36
NGC 2146	150	22	1.8'' × 14.0''	125 ± 16	15.8 ± 0.75	10.95	0.785	15.15
NGC 2196	288	14	1.8'' × 10.5''	128 ± 53	6.7 ± 1.1	15.87	1.962	16.95
NGC 2339	112	23	1.8'' × 7.0''	126 ± 15	16.5 ± 0.77	2.94	0.386	14.87
NGC 2681	120	56	1.8'' × 10.5''	90 ± 6	11.9 ± 0.54	4.15	0.346	14.57
NGC 2683	304	34	1.8'' × 16.1''	138 ± 12	13.2 ± 0.50	12.31	0.461	16.16
NGC 2775	216	18	1.8'' × 12.6''	193 ± 34	11.5 ± 1.1	8.00	0.626	15.27
NGC 2782	168	15	1.8'' × 9.1''	124 ± 24	21.0 ± 1.1	5.31	0.856	15.86
NGC 2841	104	30	1.8'' × 15.4''	208 ± 24	14.7 ± 0.60	11.62	0.546	15.01
NGC 2844	144	12	1.8'' × 6.3''	116 ± 24	18.9 ± 1.4	4.59	0.472	16.64
NGC 2903	168	17	1.8'' × 18.2''	104 ± 15	24.4 ± 1.0	24.66	0.696	17.01
NGC 2964	144	14	1.8'' × 6.3''	112 ± 25	20.8 ± 1.4	4.13	0.377	15.97
NGC 3031	48	45	1.8'' × 12.6''	237 ± 19	15.8 ± 0.4	65.94	1.249	15.72
NGC 3169	96	23	1.8'' × 16.1''	223 ± 29	20.6 ± 0.81	11.63	0.842	15.16
NGC 3227	64	42	1.8'' × 8.4''	107 ± 11	8.3 ± 0.39	3.12	0.219	14.10
NGC 3344	140	74	0.3'' × 10.5''	83 ± 7	15.4 ± 0.56	5.93	0.158	15.22
NGC 3351	128	91	0.3'' × 12.6''	121 ± 5	15.0 ± 0.37	7.60	0.253	14.88
NGC 3368	72	34	1.8'' × 18.9''	108 ± 11	11.9 ± 0.48	8.09	0.407	14.32
NGC 3521	48	29	1.8'' × 12.6''	147 ± 19	15.0 ± 0.64	7.91	0.246	14.25
NGC 3718	80	19	1.8'' × 9.8''	104 ± 22	8.3 ± 1.0	4.77	0.363	14.56
NGC 4258	72	24	1.8'' × 12.6''	126 ± 13	11.9 ± 0.75	25.85	0.912	16.49
NGC 4303	140	98	0.3'' × 13.5''	80 ± 6	14.9 ± 0.37	3.09	0.358	14.31
NGC 4314	168	13	1.8'' × 14.0''	84 ± 29	12.7 ± 1.0	27.63	1.387	17.25
NGC 4438	96	30	1.8'' × 17.5''	145 ± 16	22.4 ± 0.56	11.69	0.935	15.43
NGC 4579	32	91	0.3'' × 18.0''	199 ± 7	14.5 ± 0.39	22.44	2.640	16.19
NGC 4594	48	43	1.8'' × 24.5''	262 ± 22	13.7 ± 0.43	73.01	3.459	16.44
NGC 4736	48	83	1.8'' × 17.5''	132 ± 7	11.7 ± 0.18	14.79	0.373	13.56
NGC 4826	72	23	1.8'' × 16.8''	79 ± 46	15.8 ± 0.78	19.20	0.696	15.20
NGC 5055	88	24	1.8'' × 14.0''	152 ± 21	12.7 ± 0.72	21.85	0.700	16.01
NGC 5457	120	10	1.8'' × 6.3''	82 ± 17	13.7 ± 1.7	33.67	0.788	18.29
NGC 5746	108	83	0.3'' × 15.6''	202 ± 8	13.7 ± 0.52	16.37	2.026	16.09
NGC 5850	174	15	1.8'' × 6.3''	108 ± 43	12.8 ± 1.1	11.78	1.869	16.42
NGC 5921	160	13	1.8'' × 2.8''	83 ± 20	15.4 ± 1.2	6.07	0.605	15.96
NGC 5985	160	29	0.3'' × 8.1''	116 ± 26	14.9 ± 1.3	4.44	0.739	16.79
NGC 6384	184	77	0.3'' × 10.8''	119 ± 6	14.8 ± 0.50	29.33	3.374	17.96
NGC 6946	32	22	1.8'' × 6.3''	54 ± 7	16.9 ± 0.73	8.01	0.191	15.05
NGC 6951	168	13	1.8'' × 7.7''	79 ± 27	16.7 ± 1.4	4.35	0.472	15.67
NGC 7013	144	16	1.8'' × 7.0''	97 ± 29	17.6 ± 1.0	4.82	0.318	15.19
NGC 7217	144	14	1.8'' × 5.6''	200 ± 48	21.3 ± 1.4	21.99	1.584	16.38
NGC 7469	108	101	0.3'' × 4.5''	123 ± 14	—	11.24	3.155	16.39
NGC 7814	64	48	1.8'' × 10.5''	189 ± 17	16.6 ± 0.37	23.65	1.512	16.20

Table 4.4: Results for Fundamental Plane fits

Sample	Photometric	Kinematic	a	b
	Data	Data		
~ 9000 SDSS early-type galaxies	r^*	optical	1.51 ± 0.07	-0.76 ± 0.02
~ 800 SDSS early-type galaxies	K	optical	1.81 ± 0.06	-0.75 ± 0.05
35 local E and S0 galaxies	K	CO bandhead	1.72 ± 0.09	-0.62 ± 0.06
19 local E galaxies	K	CO bandhead	1.78 ± 0.07	-0.60 ± 0.05
19 local E galaxies	B	optical	1.39 ± 0.08	-0.73 ± 0.06
45 local bulge galaxies	K	CO bandhead	1.94 ± 0.12	-0.51 ± 0.09

Chapter 5

The Central Supermassive Black Hole in Centaurus A

5.1 An Unusual Nearby Neighbor

NGC 5128 (Centaurus A) is an important object for our understanding of central black holes, galaxy mergers, AGN activity, and the relationships among these components of galaxy evolution. However, the very characteristics which make this galaxy so interesting have also been serious roadblocks to more detailed knowledge. NGC 5128 contains large amounts of dust which hamper optical spectroscopy, especially in the central regions which are so critical for accurately measuring the black hole (BH) mass. We measure the stellar kinematics of NGC 5128 using new data from the Gemini Near Infrared Spectrograph (GNIRS) at Gemini South; we utilize the region around the CO bandheads at $2.3\ \mu\text{m}$. This observational treatment opens up a new avenue for black hole research as it allows us to probe the most interesting galaxies; NGC 5128 is the prime example.

NGC 5128 is our nearest neighbor galaxy harboring a powerful central AGN. It is a massive elliptical galaxy which hosts a strong, variable X-ray/radio source

and a massive, complex disk composed of dust, gas, and young stars. The unusual morphology of NGC 5128 was first ascribed to a significant and recent merger event by Baade & Minkowski (1954). This merger hypothesis is well-supported by the existence of optical and HI shells at large radii and the polar orientation of the disk of dust and gas along the photometric minor axis of the galaxy (Malin et al. 1983; Quillen et al. 1993; Israel 1998). The recent merger activity and central AGN are likely associated with each other, and make NGC 5128 an interesting case for BH studies. Its notable proximity makes it an attractive target, as spatial resolution on the sky translates to small linear scales in the galaxy itself.

The correlation (Gebhardt et al. 2000a,b; Ferrarese & Merritt 2000) in bulge galaxies between central black hole mass (a local property) and velocity dispersion (a global property) sheds light on the formation and evolutionary histories of both the black hole and its host. Many theories (Silk & Rees 1998; Haehnelt & Kauffmann 2000; Ostriker 2000; King 2003) predict such a correlation, and with the over twenty models that have been presented to date, none have been excluded. One of the best ways to determine the underlying physics is to study those galaxies that have an active nucleus, i.e. have a central BH which is actively accreting material, such as NGC 5128. If these galaxies lie in a different regime in correlation studies, we begin to understand the governing processes and roles of bulge and BH growth. Gebhardt et al. (2000b) use reverberation mapping estimates of the BH masses of AGN galaxies and find the same correlation as for quiescent galaxies. NGC 5128 is much closer than any of these galaxies and thus we can make a more precise measurement of the BH using stellar kinematics, the technique used for normal local galaxies. Also, NGC 5128's recent merger history holds implications for the BH- σ correlation; we can extend the parameter space within which we know how galaxies behave in this correlation.

Although galaxies with active nuclei have been a large motivation in the

search for BHs, it is difficult to make a direct dynamical mass determination for the BHs which we understand to power these AGNs. The nuclei of many AGN galaxies are heavily obscured by dust, and NGC 5128 is no exception. At optical wavelengths, the central nucleus is nearly invisible, veiled by the rich dust lane. Such dust obscuration hampers kinematic measurements made using optical data; the central BH of a galaxy like NGC 5128 cannot be measured using optical data. Moving to the near-infrared allows us to minimize these problems. Near-IR wavelengths are long enough to minimize dust extinction; the extinction in the K band is only 7% of that at B (Gaffney et al. 1995; Baes & Dejonghe 2002). Also, galaxy light in this spectral regime is almost always dominated by the older, redder stellar population (Rieke & Lebofsky 1979; Origlia & Oliva 2000; Silge & Gebhardt 2003) and is thus less affected by recent star formation. Kinematics in this spectral regime should be the best measure of the underlying stellar potential of the galaxy. As infrared instrumentation (such as GNIRS on Gemini South used in this paper) becomes more available and efficient, this region is becoming an important tool in the study of galaxies (Silge & Gebhardt 2003).

With such a motivation, Marconi et al. (2001) provide an estimate of the BH in NGC 5128 using J -band and K -band gas dynamical measurements. They find a black hole mass of $2^{+3.0}_{-1.4} \times 10^8 M_\odot$. Given a velocity dispersion for NGC 5128 of $\sim 150 \text{ km s}^{-1}$, we would expect a BH mass around $3 \times 10^7 M_\odot$ from the BH- σ correlation. If this BH mass is correct, NGC 5128 has the largest offset ever measured from the BH- σ correlation (currently measured for over forty galaxies). This is an important point. One issue is the difficulty of interpreting gas dynamics. Sarzi et al. (2002) has shown that without a well-ordered gas disk it may be impossible to determine the enclosed mass from such observations. Marconi et al. (2001) claim they see no evidence for strong nongravitational motions, but there are few galaxies with reliable enclosed masses from both gas and stellar kinematics so it is difficult to know how

to interpret these results.

Thus, NGC 5128 is important because it has recently undergone a merger, it contains a rich gas disk, its apparently large BH is actively accreting material, and it is on our doorstep. In this paper, we report the BH mass measured from near-infrared stellar kinematics and its offset relative to other galaxies. This data can help us refine our knowledge of how galaxies grow both their bulge and BH.

The distance to NGC 5128 is a matter of some debate. Israel (1998) compiles and summarizes results from globular cluster and planetary nebulae counts, globular cluster surface brightness fluctuations, and *HST* observations of halo red giant branch stars; he finds good agreement between these sources with a distance of $D = 3.4 \pm 0.15$ Mpc. More recently, the *I*-band surface brightness fluctuation study of the galaxy itself by Tonry et al. (2001) found $D = 4.2 \pm 0.3$ Mpc. Rejkuba (2004) measures the Mira period-luminosity relation and the luminosity of the tip of the red giant branch to find $D = 3.84 \pm 0.35$ Mpc. The BH measurement of Marconi et al. (2001) described above assumes $D = 3.5$ Mpc; we also use this assumption. At this distance, $1''$ on the sky corresponds to 17 pc.

5.2 Data

5.2.1 Surface Brightness Profile

To measure the BH mass, we need both photometric measurements and kinematic measurements with sufficient spatial resolution and radial extent. We combine *HST* and 2MASS imaging of NGC 5128 to satisfy these needs. *K*-band *HST* observations of NGC 5128 were obtained by Schreier et al. (1998). The nuclear region of NGC 5128 was observed on 11 August 1997 in the F222M filter in NICMOS with an exposure time of 1280 seconds. Schreier et al. (1998) report the azimuthally averaged surface brightness out to a radius of $\sim 10''$. Within $0.65''$, the surface brightness

profile of NGC 5128 is dominated by emission from a strong unresolved source, the central AGN. We do not include this light in our dynamical modeling because it does not reflect the stellar density distribution. We extrapolate to radii smaller than $0.65''$ using the *HST* data outside this radius. The logarithm of the surface brightness outside $0.65''$ is nearly linear with $r^{1/4}$, so we extrapolate this $r^{1/4}$ profile inward to our innermost kinematic point. The dynamical modeling is not strongly dependent on this extrapolation because the amount of light (and thus enclosed mass) involved at these small radii is not large and does not have a significant impact on the gravitational potential.

For photometry at larger radii, we utilize the 2MASS Large Galaxy Atlas (LGA) (Jarrett et al. 2003). These authors construct large mosaics for each of the 100 largest galaxies as seen in the near-infrared. Jarrett et al. (2003) join 2MASS scans and iteratively remove the sky background, resulting in carefully constructed, well-calibrated images of these galaxies. We use the *K*-band image of NGC 5128, the tenth largest galaxy in the atlas.

We use the multi-Gaussian expansion (MGE) method of Cappellari (2002) to fit the surface brightness profile to the 2MASS image. The MGE method is a simple parametrization with an analytic deprojection which is flexible enough to model realistic multicomponent objects. This method uses a series expansion of two-dimensional Gaussian functions to represent galaxy images. Figure 5.1 shows the result of MGE fitting for NGC 5128; this figure shows a contour map of the 2MASS LGA *K*-band image with the contours of the best-fitting MGE model superimposed. This model was constructed to have constant position angle with radius; allowing the position angle to vary does not improve the fit. The position angle was fixed at 38 degrees east of north. The best-fit model uses six two-dimensional Gaussian functions to represent the surface brightness of NGC 5128. The dust lane of NGC 5128 is visible even in this *K*-band image, emphasizing the high level of dust obscu-

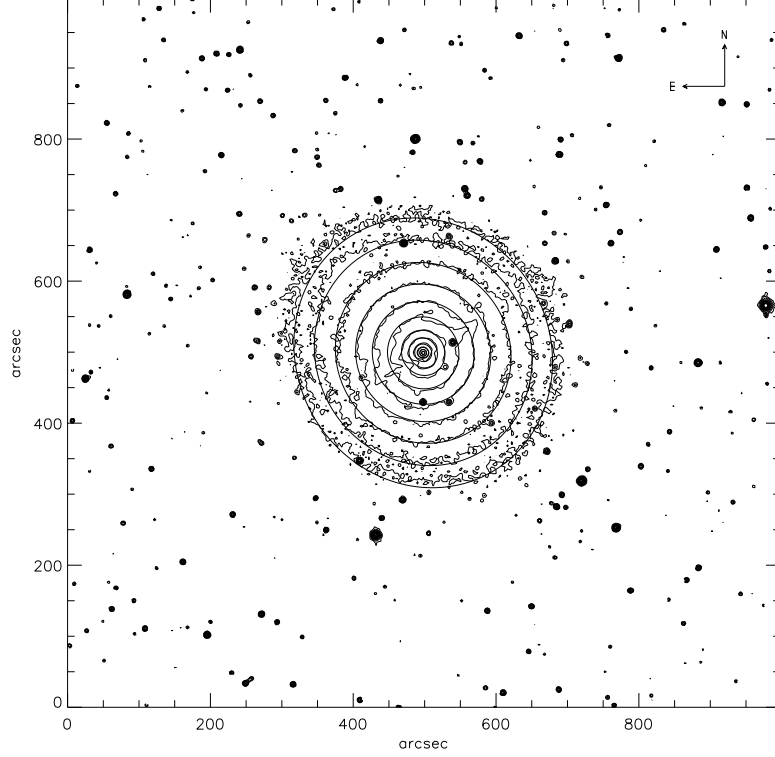


Figure 5.1: Contour map of the 2MASS LGA *K*-band image of NGC 5128. Overlaid are the contours of the MGE best-fitting model; this model’s profiles are shown in Figure 5.2. The contours are logarithmically spaced but arbitrary.

ration in this galaxy. The dust lane does not significantly hamper the MGE fitting or the kinematic observations below, however. Figure 5.2 illustrates this; the left panels show the comparison between the 2MASS photometry and the best-fitting MGE model while the right panels show the radial variation of the relative error along the profiles.

The dynamical modeling we use to constrain the BH mass assumes axisymmetry. Evidence exists that NGC 5128 is moderately triaxial (Israel 1998) but the photometric data suggest that it can be well-represented for our purposes as a

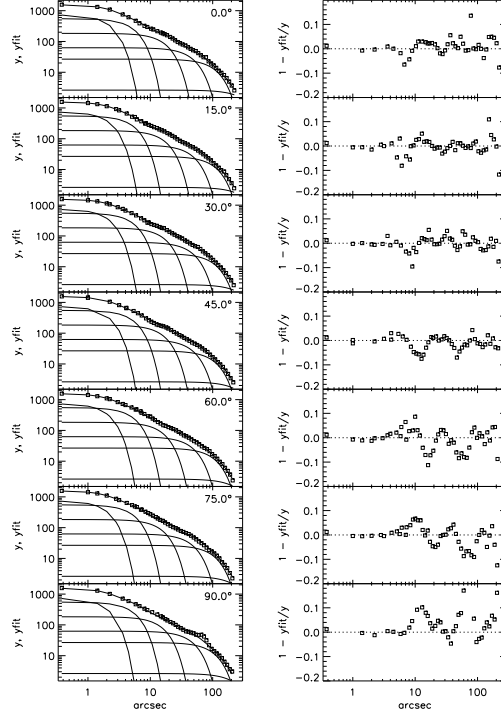


Figure 5.2: Left panels: comparison between the 2MASS LGA *K*-band photometry of NGC 5128 (open squares) and the (N=6) Gaussian MGE best-fitting model (solid line). The individual Gaussian components are also shown. The angles noted in the upper right hand corner of each panel are measured relative to the photometric major axis. Right panels: radial variation of the relative error along the profiles.

spheroid of constant ellipticity. The model with constant position angle fits the surface brightness well, and figure 5.3 shows that the ellipticity of the galaxy is small and does not change drastically. This figure presents the ellipticity of the MGE best-fitting model as a function of radius; the ellipticity is never much higher than 0.1. Thus, we can represent NGC 5128 in our modeling as a spheroid with constant projected ellipticity of 0.05. Figure 5.4 presents the final surface brightness profile along the major axis which we use in our dynamical modeling. The dashed line is the profile from the MGE best-fitting model of the 2MASS LGA image and the solid

line is the *HST* profile of Schreier et al. (1998). The *HST* data have been adjusted to match the 2MASS data between 2 and 10''; there is good agreement in the shape of the two profiles. The arrow indicates the radius of transition between domination by the AGN and domination by the stellar density distribution; the profile within this radius has been extrapolated from the *HST* data outside this radius.

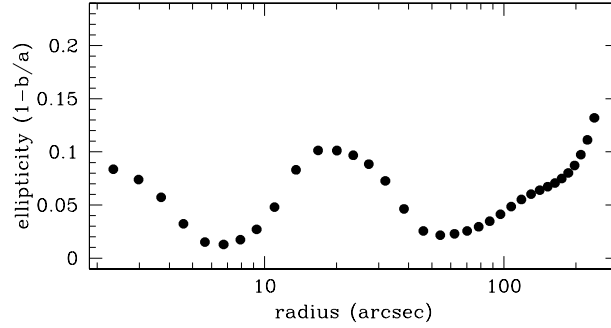


Figure 5.3: *K*-band ellipticity as a function of radius along the major axis for NGC 5128.

NGC 5128 is so enshrouded in dust that is reasonable to examine how affected observations are by dust even in the *K*-band. Marconi et al. (2000) report *HST* observations of the nucleus of NGC 5128 in *V*, *I*, and *H*, and *K*. They assume no color gradients between any of these bands and derive the implied reddening for each band. They report a dereddened *K*-band surface brightness profile. The shape of this profile is very close to the observed profile, showing deviation only within $\sim 1''$. The dereddened profile is still nearly linear with $r^{1/4}$ so we take the same approach and extend the profile inward into the region dominated by the AGN light, then compare the mass implied by the two profiles. Using the M/L_K ratio implied by the velocity dispersion profile described in Section 2 (and in agreement with the dynamical modeling of Sections 3 and 4), the enclosed stellar mass at 1'' for an edge-on model is $2 \times 10^7 M_\odot$ for the original profile and $3 \times 10^7 M_\odot$ for the dereddened

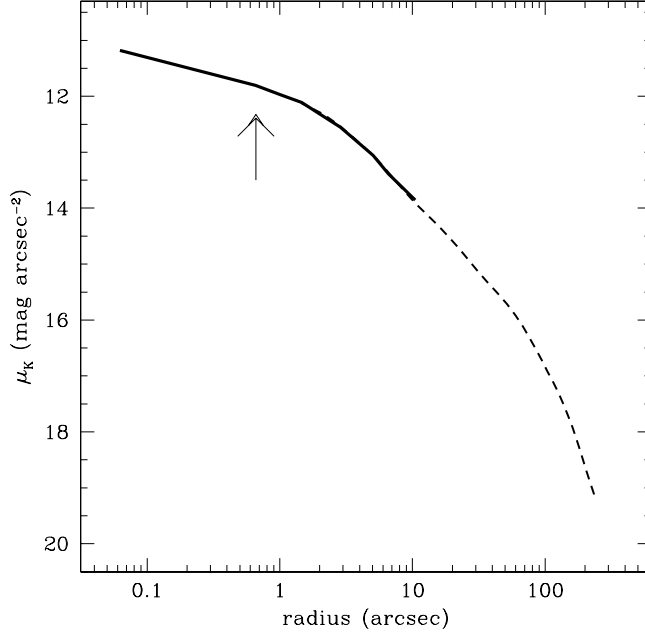


Figure 5.4: *K*-band surface brightness for NGC 5128. The dashed line is from the MGE fitting of the 2MASS LGA image and the solid line is from the *HST* data of Schreier et al. (1998). The *HST* data have been adjusted to match the 2MASS data between 2 and 10". The arrow indicates the radius at which light from the AGN dominates; the profile within this radius has been extrapolated from the *HST* data outside this radius.

profile. This difference of $1 \times 10^7 M_\odot$ is a small fraction of the BH mass we measure, and thus will not have a significant effect. We ran a small suite of dynamical models using the dereddened profile and found that this is indeed the case; there is no difference in our results. Similarly, this applies to the extrapolation of the stellar light into the region dominated by emission from the AGN. The difference in implied enclosed mass for different extrapolations is even smaller than for the original and dereddened profiles and the results of our modeling are not dependent on changes in this extrapolation.

5.2.2 Kinematic Observations

NGC 5128 was observed on 2004 March 8 and June 15 as part of system verification for the Gemini Near-Infrared Spectrograph (GNIRS) on Gemini South, using Gemini program identification number GS-2004A-SV-8. GNIRS has a 1024×1024 Aladdin III InSb detector array with a spatial scale of $0''.15 \text{ pixel}^{-1}$. We utilize the long-slit, short-camera mode of GNIRS which can obtain the spectrum of the K -band atmospheric window ($1.9 \mu\text{m}$ to $2.5 \mu\text{m}$) in one exposure. Using a 32 l/mm grating and $0.3'' \times 99''$ slit, we obtained spectral resolution of 1600, measured from calibration lamps lines and night sky lines. With this resolution, we can measure velocity dispersions down to 80 km s^{-1} , much smaller than the dispersion of NGC 5128.

We utilize the K -band CO absorption bandheads from evolved red stars to measure the stellar kinematics of NGC 5128. The $(2-0)^{12}\text{CO}$ absorption bandhead at $2.293 \mu\text{m}$ is the first of a series of many bandheads which stretch out redward. These features are in a dark part of the infrared sky spectrum and are intrinsically sharp and deep, making this region very sensitive to stellar motions (Lester & Gaffney 1994). They are the strongest absorption features in galactic spectra between $1\text{-}3 \mu\text{m}$; this region is optimal for studying stellar kinematics because wavelengths are long enough to minimize extinction from dust but short enough to avoid emission from hot dust (Gaffney et al. 1995). Silge & Gebhardt (2003) present a detailed calibration of stellar kinematics measured using the first CO bandhead.

The first observation was made with the slit oriented perpendicular to the inner dust ring (along the major axis at large radii), centered on the bright AGN. The second observation was made with the slit oriented parallel to the dust line but offset from the center by $0.85''$. Individual exposures were 120 seconds; between exposures on the object, sky exposures of 120 seconds were taken $\sim 200''$ to the southeast. NGC 5128 is very large on the sky and large telescope offsets are required to obtain

good sky subtraction. The total on-source integration time was 2160 seconds for the slit position perpendicular to the dust lane and 1680 seconds for the slit position parallel to the dust lane. We measured the seeing from images of telluric calibration stars and the central unresolved AGN. The seeing during the first observation was $0''.45$; during the second it was $0''.6$.

To remove the shape of the telluric absorption spectrum from our observations, we observed an A0V star (HD107422). A dwarfs have nearly featureless spectra in this region (Wallace & Hinkle 1997); we require a good measure of telluric absorption because we are interested in the detailed shape of the galaxy spectrum. Silge & Gebhardt (2003) present more details on this point. The A0V observations were made by dithering the telescope $10''$ across the slit to measure the sky at the same slit position in alternating exposures.

Wavelength calibration for both galaxy and star observations was carried out using the arc lamps of the Facility Calibration Unit for Gemini South. Guiding was provided by the peripheral wavefront sensor assigned to a star outside the science field for the galaxy or telluric standard. During the off-source sky exposures for the galaxy observations, the guiding was paused and we relied on the telescope tracking because of the difficulty presented by the large offset; this sky subtraction procedure worked well. No attempt is made to flux calibrate the spectra since we are only concerned with the kinematic analysis.

5.2.3 Data Reduction

Data reduction proceeds similarly to that described in Silge & Gebhardt (2003). We rectify the images in the spectral direction using the arc lamp lines and subtract each sky exposure from its associated object exposure to remove the sky background. The subtracted images are then shifted in the spatial direction so that the center of the galaxy in each image is aligned; we calculate the biweight (Beers et al. 1990) of all

the processed images to make one image for the galaxy. The one-dimensional spectra are then extracted from the two-dimensional image in nearly logarithmically spaced spatial bins. The stellar spectra are reduced in a similar manner but extracted in a single aperture. We then remove the telluric absorption spectrum from the galaxy spectra by dividing by a “flat” spectrum, obtained from the A0V. We obtain good results for this spectral flattening compared to our experience with other instruments and sites.

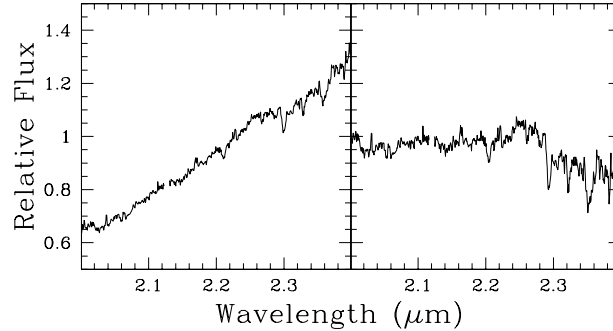


Figure 5.5: Spectrum for one spatial bin $0.''45$ from the galaxy center. The left panel shows the spectrum dominated by the AGN emission; the right panel shows the spectrum after this AGN continuum shape has been removed.

The second observation was taken with the slit offset from the center of the galaxy but the first observation was well-centered on the central nucleus. The spectra in the central spatial bins from this observation are dominated by emission from the central AGN; the CO bandheads are filled in by this emission. We worked to recover some of this information by removing the AGN emission. The equivalent width of the $(2-0)^{12}\text{CO}$ bandhead is largely constant with radius in this galaxy for regions outside the AGN, so we measure the AGN contribution by its dilution of the equivalent width. After this process, we are able to use data within $0.''3$ of the center in the kinematic fitting. Spectra out to $1''$ exhibit changes in equivalent width which require removal of AGN light. Figure 5.5 illustrates the results of this

step for one bin $0.''45$ from the center. The left panel shows the spectrum before removal of the AGN emission and the right panel shows the spectrum after this process, ready for its kinematic fitting.

5.2.4 Extracting the Velocity Distribution

Once we have the spectrum in each spatial bin, we extract the kinematic information. A galaxy spectrum is the convolution of the line-of-sight velocity distribution (LOSVD) with an average stellar spectrum; to obtain this internal kinematic information, we use the fitting technique of Gebhardt et al. (2000c), deconvolving the spectrum directly in pixel space using a maximum penalized likelihood estimate to obtain a nonparametric LOSVD. An initial velocity profile is chosen and this profile is convolved with a stellar template spectrum. The residuals to the galaxy spectrum are calculated and the velocity profile is changed to minimize the residuals and provide the closest match to the observed galaxy spectrum.

The choice of template star is important for kinematic fitting using the CO bandheads; this feature is sensitive to template mismatch (Silge & Gebhardt 2003). Thus, we give the fitting program a variety of template stellar spectra and simultaneously fit for the velocity profile and the stellar template weights. As a result, our fitting procedure provides both the LOSVD and stellar population information. We use the near-IR stellar spectral atlas of Wallace & Hinkle (1997) as our templates, choosing nine stars with $(2-0)^{12}\text{CO}$ equivalent widths ranging from less than 5 \AA to over 20 \AA . These spectra have a somewhat higher spectral resolution than ours, so before using them as stellar templates we have carefully convolved them to our spectral resolution using a Gaussian distribution with $\sigma = 5.37 \text{ \AA}$. The best fit almost always gives most of the weight to a few of the template stars. The fits in all the spatial bins are dominated by K and M giants with smaller contributions from other stars with smaller and larger equivalent widths; there is no significant trend

with radius for the template make-up.

Figure 5.6 shows the results for some example spatial bins for NGC 5128. The noisy line is the observed spectrum and the smooth line is the template stellar spectrum convolved with the derived LOSVD. Each frame in figure 5.6 shows the spectrum in one spatial bin on one side of the galaxy; in the actual fitting we fit both sides of the galaxy simultaneously with the LOSVD flipped around the $v = 0$ axis for the opposite side. For the spatial bins where we removed the AGN emission, we were not able to use the same wavelength region for the fitting. The AGN removal worked best over smaller wavelength regions; in the innermost few bins we fit only the first bandhead while in intermediate bins we fit the first two. From $1''$ outward, we used the full region shown in figure 5.6.

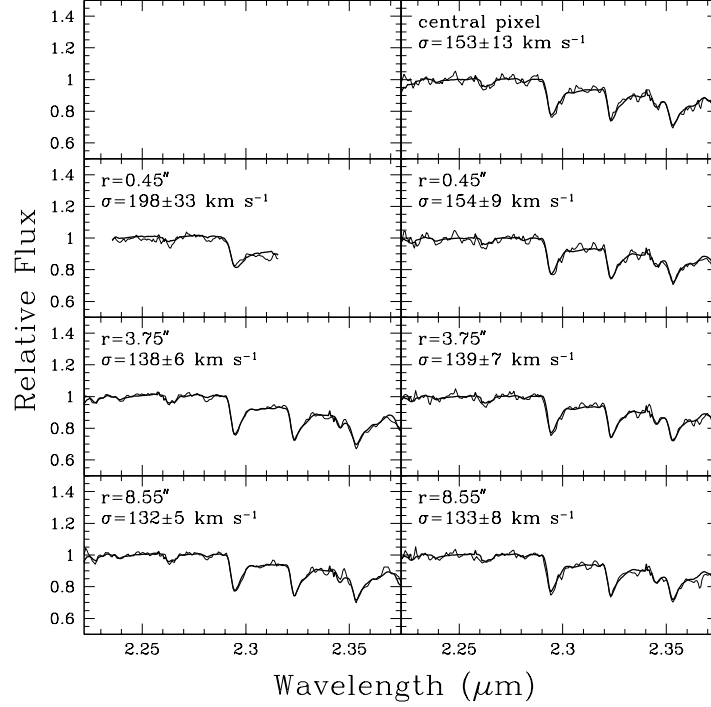


Figure 5.6: Rest-frame spectra for seven example spatial bins (noisy line) and for the template stellar spectrum convolved with the derived LOSVD for that bin (smooth line). The derived second moment of the LOSVD and its 68% uncertainty is reported for each of these bins. The left panels show data from the axis perpendicular to the dust disk; the right panels show data from the axis parallel to the dust disk but offset from the center.

We determine the uncertainties for the LOSVDs using the Monte Carlo bootstrap approach of Gebhardt et al. (2000c). The initial fit to the observed galaxy spectrum is used to generate 100 simulated spectra with noise chosen to match that of the observed spectrum. These 100 synthetic galaxy spectra are then deconvolved to determine their LOSVDs in the same way the original observed spectrum is deconvolved. These LOSVDs provide a distribution of values for each velocity bin which allows us to estimate the uncertainty and examine any bias in the moments

of the LOSVD. The median of the distribution determines any potential bias from the initial fit, and the spread of the distribution determines the uncertainty. In order to generate the 68% confidence bands, we choose the 16% to 84% values from the 100 realizations.

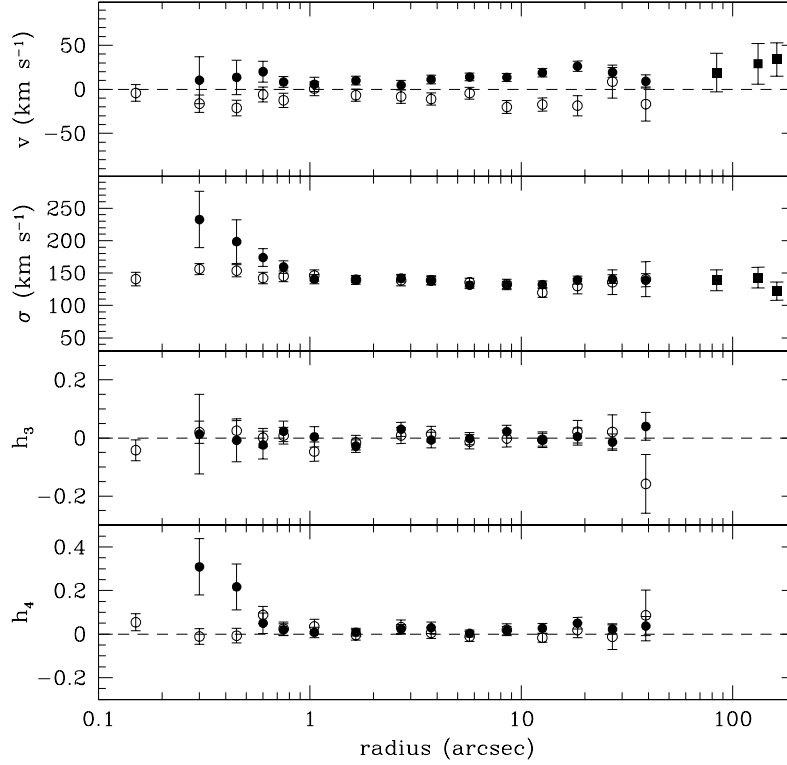


Figure 5.7: Gauss-Hermite moments of the LOSVDs along the slit perpendicular to the dust disk (filled circles) and along the slit parallel to the dust disk but offset from the center (open circles). The filled squares are from Peng et al. (2004) and are along the same axis as the filled circles.

Most LOSVD fitting techniques make some assumption about the shape of the LOSVD, i.e. it is Gaussian or Gauss-Hermite polynomial. Our technique obtains a nonparametric LOSVD; no a priori assumptions about the shape of the LOSVD

are made except that it is nonnegative in all bins and subject to some smoothness constraint. We are able to exploit the full LOSVDs in the dynamical modeling below. We plot the parameterization of the LOSVDs by Gauss-Hermite moments in figure 5.7 and present them in table 5.1. The velocity dispersion is very close to 135 km s^{-1} on both axes for most of the radius range ($\sim 2''$ to $\sim 40''$). The luminosity-weighted σ_* using an aperture of $60''$ along the slit parallel to the dust disk is $138 \pm 15 \text{ km s}^{-1}$. The axis perpendicular to the dust lane (which was centered on the galaxy nucleus) shows a steep rise in both σ and h_4 (which indicates a triangular distortion from a Gaussian shape, i.e. strong high velocity wings on the LOSVD) within the central arcsecond. We detect rotation along both axes, the photometric major axis and the axis parallel to the dust disk in the center, as have other authors including Peng et al. (2004) and Hui et al. (1995). This is not strictly consistent with an axisymmetric model, as we discuss later.

These Gemini observations go out to $\sim 40''$, but this is only about halfway to the half-light radius. According to Jarrett et al. (2003), the K -band half-light radius is $r_{eff} = 82.6''$. Limited spatial extent can significantly reduce the precision to which one can measure the BH mass (Richstone et al. 2004) so we include kinematic data at larger radii to increase the precision of our measurement. We use a kinematic study of planetary nebulae in NGC 5128 (Peng et al. 2004) which extends well into the galaxy halo. Peng et al. (2004) report the rotation curve and velocity dispersion along the photometric major axis out to $80'$, including planetary nebulae within a perpendicular distance of $\pm 120''$ to this axis. The largest radii are not important to us as we are mainly interested in the gravitational potential at smaller radii; we include their first three points only, extending our kinematic coverage to $2r_{eff}$. These kinematic data are rotation velocities and velocity dispersions, not full LOSVDs. In our dynamical modeling, we assume Gaussian LOSVDs with first and second moments to match the planetary nebulae data for these points. The

lack of higher order information at these large radii does not effect the BH mass measurement. The planetary nebulae data are shown in figure 5.7 and presented in table 5.1.

5.3 Dynamical Models

The dynamical models are constructed as in Gebhardt et al. (2000c) and Gebhardt et al. (2003) using the orbit superposition technique first proposed by Schwarzschild (1979). We use the surface brightness profile described above to estimate the luminosity density distribution; the surface brightness can be deprojected assuming axisymmetry and some chosen inclination. This luminosity density then translates to a mass density distribution, assuming some stellar mass-to-light (M/L) ratio and BH mass. It is this mass density distribution which then defines the potential for a given model. Using this derived potential, we follow a representative set of orbits which sample the available phase space. We then determine the orbit superposition (i.e. nonnegative set of weights for the orbits) which provides the best match (the minimum χ^2) to the data. We can impose smoothness on the phase-space distribution function by maximizing entropy (Richstone & Tremaine 1988; Thomas et al. 2004). We repeat this process for a variety of BH masses, M/L ratios, and inclinations to find the overall best match.

To obtain a smooth χ^2 distribution, it is necessary to include an adequate number of orbits. We sample the gravitational potential by launching orbits from points in the three-dimensional space spanned by the energy E , the angular momentum L_z , and the third integral I_3 . The limits of this space are well-understood, and Richstone et al. (2004) details the considerations for the sampling of this phase space. Our final model contains $\sim 10,000$ orbits, adequate to obtain a smooth χ^2 distribution for our binning scheme.

To compare the model with the data, we map both the observations and

orbits to a grid of 20 radial bins, 5 angular bins, and 17 velocity bins. The time a given orbit spends in a given bin translates to its contribution to the light in that bin, and thus the mass. The radial binning scheme for the model is the same as that for the data shown in figure 5.7 and table 5.1; we have data on the major and minor axes, i.e. in two angular bins of the model. The binning schemes are chosen to maximize the S/N of the data. The velocity bins span the minimum and maximum velocities of the orbits; these must be chosen carefully because the high-velocity wings of the LOSVD are affected the most by a BH. We incorporate seeing in the model by convolving the light distribution for each orbit with the PSF of the kinematic observations. The Gemini observing runs had PSFs, approximated as Gaussians, of $0''.45$ in the March run and $0''.60$ in the June run. The planetary nebulae data have such large binning that seeing does not affect them.

For each model, we use the best-fit orbit superposition to match the light in each of the 100 spatial bins and the LOSVDs in the 33 bins where we have data. We fit to the full LOSVDs, not a parameterization such as the Gauss-Hermite moments. The orbit weights are chosen so that the luminosity density in each spatial bin matches the data to better than 1%, with typical matches better than 0.1%. This match is treated as a constraint, not as a difference to be minimized. We do minimize χ^2 for each model, with $\chi^2 = \Sigma[(y_i - y'_i)/\sigma_i]^2$, where the y_i 's are the LOSVD bin heights of the data, the y'_i 's are the LOSVD bin heights of the model, and σ_i is the uncertainty of the bin height of the data. Each combination of BH mass and stellar M/L ratio has an orbit superposition which gives a minimum χ^2 ; we then compare the χ^2 of different such combinations to find the best match to the data. We use this measure of χ^2 to determine the uncertainties in the BH mass and stellar M/L as well. These are correlated, as the model can exchange mass in the BH for higher M/L, and thus we use the two-dimensional χ^2 distribution to determine the 68% confidence bands for these quantities, where $\Delta\chi^2 = 1$ for one

degree of freedom.

5.4 Results

The fact that NGC 5128 has rotation along more than one axis has interesting implications for its dynamical structure. This galaxy is either tumbling or triaxial. Tumbling is not an equilibrium dynamical state, but as a recent major merger, NGC 5128 may well not be in dynamical equilibrium. Strictly speaking, this means that we cannot match well the kinematics of NGC 5128 and the kinematics of an axisymmetric orbit superposition model. In our models, we choose to identify one axis of the observations with the rotation axis of the model; the rotation on the other axis serves only to balloon up the χ^2 . We find that the best-fitting models for NGC 5128 constructed in this way are not very good fits and have unrealistic characteristics; we choose to take another approach.

We return to our LOSVDs in each bin and symmetrize them about $v = 0$, taking the mean of each side to make the new, symmetric LOSVD. These new LOSVDs have no net rotation. This is not the true state of NGC 5128, but the resulting LOSVDs do imply nearly the same enclosed mass as our “true” LOSVDs. The kinetic energy is proportional to $(v^2 + \sigma^2)$; using a symmetric LOSVD forces the kinetic energy from the v^2 term into the σ^2 term. The quantity $(v^2 + \sigma^2)$ is nearly identical for each pair of “true” and symmetrized LOSVDs. We can then build orbit superposition models to match the “true” kinematics along one axis which we identify as the axis of rotation and these no-rotation kinematics along the other axis. NGC 5128 is the first galaxy with such a complex dynamical structure to be targeted with the orbit superposition method for measuring a BH; although this symmetrization on the minor axis is not ideal, it is reasonable to believe that it will not bias the result for the central BH mass and M/L since we are fitting to $(v^2 + \sigma^2)$.

We are then faced with the quandary of which axis to identify as the rotation axis. It seems logical that the rotation along the direction of the dust disk at small radii would be important for the determination of the BH mass; however, inclusion of rotation at large radii also has important affects on inferred BH masses (Richstone et al. 2004). It is unclear what the best choice would be, especially since BH masses have not been determined using orbit superposition models for galaxies with such complex dynamical structure as NGC 5128. We thus choose to repeat our entire modeling procedure for both cases, first matching to the rotating kinematics along the dust disk axis and non-rotating kinematics along the photometric major axis (hereafter DUST), then switching to rotating kinematics along the photometric major axis and non-rotating kinematics along the dust disk axis (hereafter PHOT). We can thus compare the BH masses inferred by including different data.

Figure 5.8 presents the results of this process. Each panel shows χ^2 as a function of BH mass and M/L ratio, obtained by comparing model kinematics to observed kinematic data for NGC 5128. The left panel shows the DUST models and the right panel shows the PHOT models. The contours are drawn using a two-dimensional smoothing spline (Wahba 1990) but the modeled values are fairly smooth and large smoothing is not necessary. Figure 5.9 presents the χ^2 goodness of fit as a function of black hole mass; we have marginalized the two-dimensional χ^2 distributions shown in figure 5.8 over M/L to obtain these distributions, i.e. used the M/L for each point in figure 5.9 which provides the smallest χ^2 at that BH mass. The dashed line and open squares are for the DUST models while the solid line and filled circles are for the PHOT models. The points show the χ^2 of individual models; the lines are marginalized from the smoothed distributions illustrated in the contours shown in figure 5.8. The models with rotation along the dust axis had overall higher χ^2 values so these are offset vertically for plotting purposes.

The BH masses from the two sets of models are in excellent agreement. For

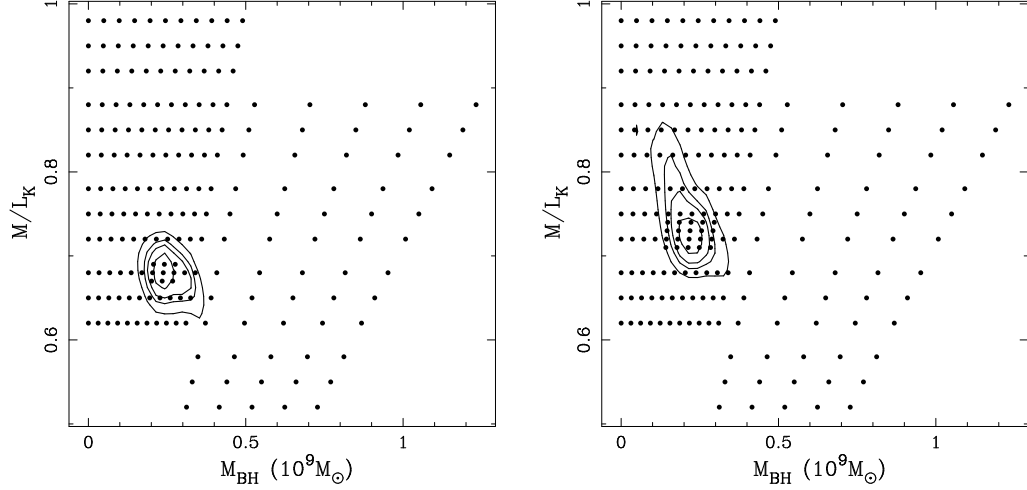


Figure 5.8: Two-dimensional plots of χ^2 as a function of BH mass and M/L ratio for both orientations we modeled. The left-hand panel shows models with rotation along the galaxy’s photometric major axis (PHOT models) and the right-hand panel shows models with rotation along the dust disk (DUST models). The points represent models. The contours were determined by a two-dimensional smoothing spline interpolated from these models and represent $\Delta\chi^2$ of 1.0, 2.71, 4.0, and 6.63 (corresponding to 68%, 90%, 95%, and 99% for 1 degree of freedom).

the PHOT models, the BH mass is $2.4^{+0.3}_{-0.2} \times 10^8 M_\odot$; for the DUST models, it is $2.2^{+0.3}_{-0.3} \times 10^8 M_\odot$. The PHOT models have significantly lower χ^2 ($\Delta\chi^2 = 28.3$), so we identify this as the preferred orientation. The photometric major axis of the galaxy (the rotation axis of the PHOT models) is the important axis for most of the galaxy’s mass; it is reasonable that this is more important for a dynamical model of the galaxy. The M/L_K ratios are $0.68^{+0.01}_{-0.02}$ for the PHOT models and $0.72^{+0.03}_{-0.02}$ for the DUST models. These are not in agreement to within the 68% confidence limits but are close. These M/L_K ratios are in good agreement with those found for bulges and elliptical galaxies (Moriondo et al. 1998; Mobasher et al. 1999). Interestingly, there is some covariance in the DUST models but very little in the PHOT models.

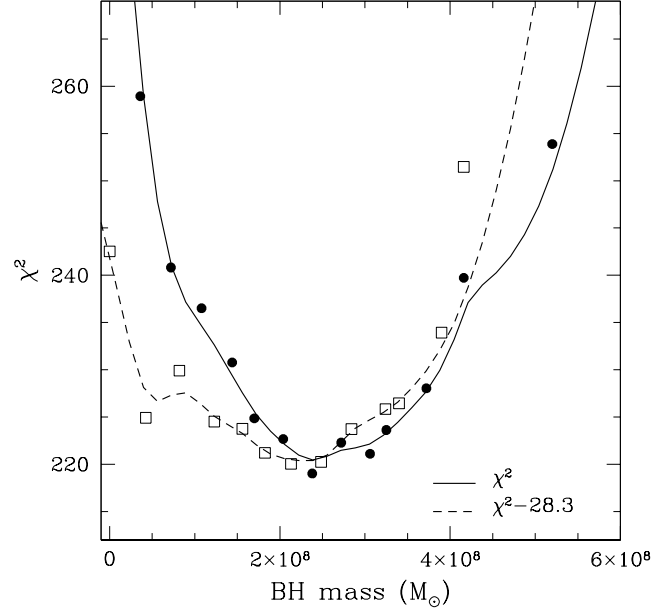


Figure 5.9: The χ^2 goodness of fit obtained by comparing model kinematics to observed kinematic data for NGC 5128, versus model black hole mass. The dashed line and open squares are for the models with the rotation axis along the dust disk (DUST models), and the solid line and filled circles are for the models with the rotation axis along the photometric major axis of the galaxy (PHOT models).

The PHOT models use the data that were well-centered on the galaxy nucleus on the model’s rotation axis. In contrast, the DUST models use the data that were offset from the nucleus along the direction of the model’s rotation axis and thus do not have any data on the actual rotation axis of the model. Such data appear to be important in breaking the degeneracy between BH mass and M/L ratio and placing the strongest constraints on each quantity.

Figure 5.10 compares the model kinematics with the observed kinematics for each axis on which we have data, for each orientation of rotation that we modeled. The left panels are for the PHOT models and the right panels are for the DUST models. The squares are from the photometric major axis and the circles are from

the axis parallel to the dust disk but offset from the nucleus. The open symbols are the actual (or symmetrized) data and the filled or starred symbols are from the models. We emphasize that we fit the full LOSVDs and that this plot shows only the Gauss-Hermite moments of the LOSVDs. Notice the symmetrization of the observed data; $v = 0$ for every radial point on the dust axis for the PHOT models and every radial point on the photometric major axis for the DUST models.

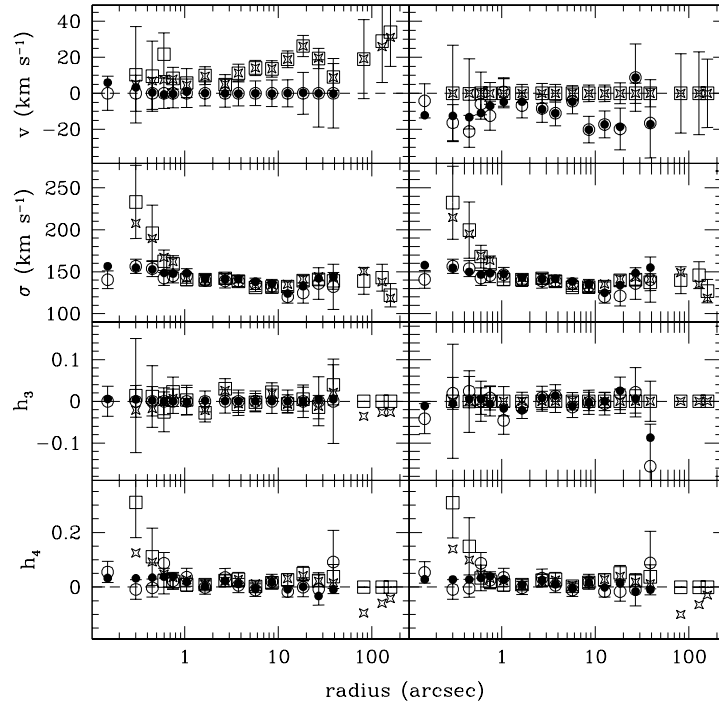


Figure 5.10: Comparison of observed kinematic data along each slit for NGC 5128 with model kinematics for the two best-fitting edge-on models. The left-hand panel compares to the best-fitting edge-on model with rotation along the photometric major axis (PHOT models) and the right-hand panel compares to the best-fitting edge-on model with rotation along the dust disk (DUST models). The open symbols are the data: circles for the axis parallel to the dust disk but offset from the center and squares for the galaxy photometric major axis. The filled circles are from the model on the axis parallel to the dust disk and the starred squares are from the model on the galaxy photometric major axis.

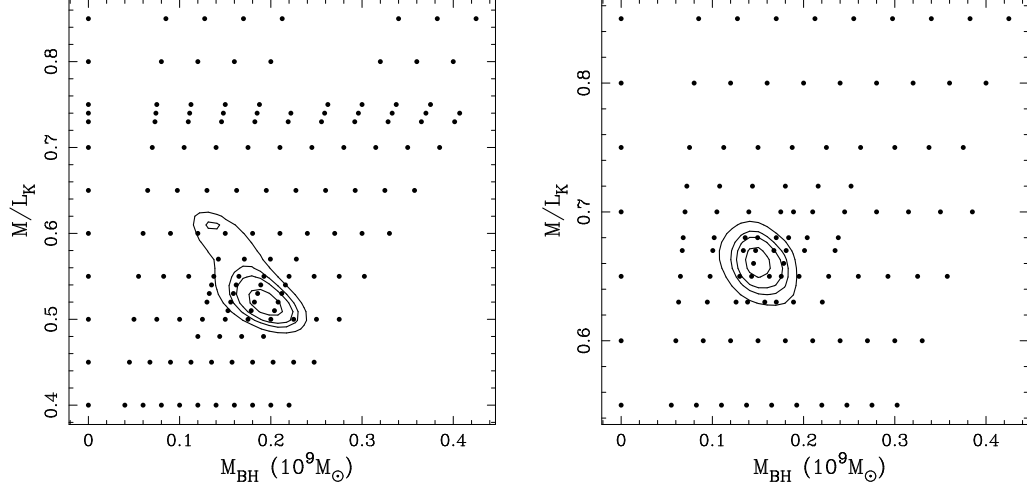


Figure 5.11: Same as figure 5.8 but for models with PHOT configuration and with inclination of 45° (left-hand panel) and 20° (right-hand panel).

NGC 5128 appears very round but it is possible that it is intrinsically quite flattened. Dynamical models such as those of Wilkinson et al. (1986) and Hui et al. (1995) conclude that it is indeed flattened, with axis ratios of 1:0.98:0.55 and 1:0.92:0.79. The orbit-based models described above are all for an edge-on configuration, i.e. assuming the NGC 5128 is indeed nearly intrinsically round. We test the effect of using a model with different inclinations. We take the case of inclination $i = 20^\circ$, which implies axis ratios of 1:1:0.5, and $i = 45^\circ$, which implies axis ratios of 1:1:0.9. Figure 5.11 presents the results for the PHOT configuration of the kinematic data, the two-dimensional distribution of χ^2 as a function of BH mass and M/L ratio. The best-fit BH mass for $i = 20^\circ$ is $1.5^{+0.3}_{-0.2} \times 10^8 M_\odot$ and the best-fit M/L_K ratio is $0.68^{+0.02}_{-0.02}$. The M/L_K ratio is in good agreement with the edge-on models but the BH mass is $\sim 30\%$ smaller. Previous studies using this technique (Gebhardt et al. 2000c, 2003) have found that on average, inclination appears to cause a 30%

random change in the BH mass, exactly what we find here. The best-fit BH mass for $i = 45^\circ$ is $1.8_{-0.4}^{+0.4} \times 10^8 M_\odot$ and the best-fit M/L_K ratio is $0.53_{-0.03}^{+0.04}$, a BH mass intermediate between the other two inclinations. The edge-on and $i = 20^\circ$ estimates of the BH mass are only different by 2σ and this somewhat smaller BH mass does not markedly affect our conclusions below. The χ^2 of the edge-on model is significantly less than either inclined model ($\Delta\chi^2 \sim 100$) so we adopt that value for the BH mass. It is uncertain whether we can constrain the actual inclination of NGC 5128; the effect of intrinsic triaxiality on the inferred inclination of an axisymmetric model is unknown. It is unclear what these results indicate for the intrinsic axis ratios of this galaxy, but changing the inclination of the model drastically does not change the BH mass much so our conclusions are not hampered by this limitation.

5.5 Discussion

Our BH masses for all modeled inclinations are in good agreement with the gas dynamical results of Marconi et al. (2001). This agreement supports these authors' claim that the gas kinematics of NGC 5128 are well described by an ordered gas disk and suggests that in such situations, gas dynamics give reliable estimates for BH masses. Also, NGC 5128 has the largest offset from the BH- σ correlation ever measured. The BH of NGC 5128 is five to ten times larger than it should be as predicted by this correlation. Marconi & Hunt (2003) use the BH mass from Marconi et al. (2001) to place NGC 5128 (along with ~ 25 other objects) in the correlation between BH mass and near-infrared bulge luminosity. Marconi & Hunt (2003) find that the spread in this correlation is similar to that of the BH- σ correlation. NGC 5128 does lie above this relation (i.e. its BH mass is somewhat high compared to its near-IR bulge luminosity) but it is not a striking outlier in this relation. Our own estimate of the K -band bulge luminosity is somewhat in conflict with this result. Our estimate of $M_K = -23.7$ mag (based on the 2MASS imaging described

in Section 2.1) is fainter than $M_K = -24.5$ presented by Marconi et al. (2001); using our bulge luminosity, the BH of NGC 5128 is more discrepant compared to the local galaxy population. Interestingly, NGC 5128 is not a strong outlier in the all-infrared Faber-Jackson relation or Fundamental Plane (Silge & Gebhardt, in preparation). The host galaxy appears quite normal compared to the local galaxy population while the BH mass is startlingly high.

The remarkably high BH mass for NGC 5128 suggests that its BH assembled before the host stellar bulge. There are a few other observations that suggest this. Walter et al. (2004) use molecular gas observations of the host galaxy of a $z = 6.42$ quasar to show that it is missing the large stellar bulge implied by the BH- σ and BH- L_{bulge} correlations. A large BH is in place, but there does not appear to be an associated stellar bulge. This, along with our result for NGC 5128, is in sharp difference to the census of BHs in local galaxies described by Ho (2004) and others and the result for QSOs (Shields et al. 2003). There are several attractive theoretical models which explain the observed BH- σ correlation (Silk & Rees 1998; Fabian 1999; King 2003) and some also naturally explain such galaxy properties as color bimodality and the Faber-Jackson relation (Murray et al. 2005; Springel et al. 2004). These models all use similar feedback arguments to show how an actively accreting BH can regulate its own growth by expelling gas from its immediate vicinity through an outflow or wind. The wind becomes stronger as the BH grows, driving away the gas that fuels the BH growth; the models connect the ultimate size the BH can attain with the host galaxy characteristics (i.e. σ). These models have been invoked to explain the BH- σ correlation of normal galaxies; understanding NGC 5128 and its offset from the BH- σ relation in the context of these arguments will provide an important clue for our understanding of the role of central BHs in galaxy formation.

Why is NGC 5128 such an unusual galaxy in this respect? The two most obvious possibilities are the recent major merger it has undergone and its AGN

activity. The AGN activity seems to be a likely culprit. It is possible that a supermassive black hole that is currently growing by accreting material could be large compared to its host galaxy; perhaps the host galaxy has not had time to catch up to the growth of the BH. However, there has been some study of the BH- σ correlation in galaxies with active nuclei and this is not what has been found. Gebhardt et al. (2000b) studied the relationship between galaxy velocity dispersion and BH mass measured by reverberation mapping for a sample of active galaxies and found that these active galaxies are consistent with the BH- σ correlation for quiescent galaxies. We need more BH masses measured through stellar (or possibly in some cases, gas) dynamics for active galaxies to further explore this issue.

NGC 5128's merger history presents another possibility which has been less studied until now. Perhaps some aspect of the merging process builds up the central black hole of a galaxy before later evolution causes the galaxy's velocity dispersion to catch up. For instance, if two galaxies with central supermassive BHs merge, their BHs may merge into one BH quickly while it may take much longer for the new galaxy to assume its final dynamical configuration. If some scenario like this is the case, we have happened to catch NGC 5128 at this stage in its merger when its supermassive BH has this specific relationship to the galaxy as a whole. Little is known about the central BHs of galaxies that have undergone recent mergers; NGC 5128 is the first such galaxy to have its central BH measured.

It is also possible that both of these aspects are acting in NGC 5128, of course. For both of these questions, using near-infrared kinematics holds promise for making progress. Many AGN and all recent merger galaxies are significantly dusty and thus inaccessible to optical spectroscopy. Using the techniques described here, we can reliably measure the kinematics of such galaxies. NGC 5128 is so enshrouded in dust that even its K -band light shows signs of reddening but this does not hamper our kinematic measurements or dynamical modeling. Also, with

the untimely death of STIS on HST, our main method of measuring black holes has been eliminated and we can no longer rely on our previous techniques. If we want to continue to explore the connections between black holes and their host galaxies that HST first uncovered, the only method currently available is to use stellar kinematics measured at near-IR wavelengths. The excellent atmospheric seeing in the near-IR at good telescope sites, such as with Gemini and GNIRS, allows us to probe the central regions of nearby galaxies where the gravitational effects of the black hole are strongest. Also, as adaptive optics instrumentation becomes more available, we can push to higher spatial resolution and thus the sphere of influence of black holes of more distant galaxies.

Table 5.1: Gauss-Hermite moments of LOSVDs for NGC 5128

radius (")	parallel to dust disk, offset				perpendicular to dust disk, centered			
	v (km s ⁻¹)	σ (km s ⁻¹)	h_3	h_4	v (km s ⁻¹)	σ (km s ⁻¹)	h_3	h_4
0.00	-12±10	153±13	0.036±0.053	0.056±0.051				
0.15	-4±9	141±11	-0.042±0.036	0.054±0.039				
0.30	-16±10	156±9	0.020±0.038	-0.011±0.036	10±27	233±44	0.013±0.137	0.309±0.129
0.45	-21±9	154±9	0.025±0.035	-0.007±0.033	14±19	198±34	-0.008±0.074	0.217±0.105
0.60	-6±8	142±9	0.001±0.032	0.088±0.039	20±12	174±14	-0.024±0.048	0.050±0.047
0.75	-12±8	145±8	0.008±0.029	0.025±0.031	8±6	159±10	0.023±0.035	0.020±0.027
1.05	1±8	146±9	-0.047±0.033	0.035±0.033	6±8	141±7	0.004±0.035	0.008±0.024
1.65	-7±7	140±7	-0.016±0.025	-0.004±0.024	10±5	140±5	-0.028±0.022	0.009±0.018
2.70	-8±8	139±8	0.009±0.028	0.032±0.033	5±5	142±6	0.030±0.024	0.024±0.021
3.75	-11±7	139±7	0.013±0.027	0.006±0.026	11±5	138±6	-0.007±0.027	0.029±0.026
5.70	-4±7	136±7	-0.013±0.025	-0.011±0.023	14±4	131±5	-0.002±0.021	0.003±0.016
8.55	-20±7	133±8	-0.002±0.029	0.020±0.027	14±5	132±5	0.022±0.022	0.016±0.019
12.60	-17±7	120±7	-0.006±0.027	-0.017±0.020	19±5	132±5	-0.006±0.022	0.027±0.022
18.45	-19±12	130±12	0.022±0.039	0.018±0.035	26±6	139±6	0.005±0.029	0.050±0.027
27.00	9±19	136±19	0.021±0.059	-0.012±0.059	19±6	141±7	-0.014±0.028	0.022±0.021
38.85	-17±19	141±27	-0.158±0.101	0.086±0.116	9±8	139±10	0.040±0.048	0.037±0.044
82.35					19±22 ^a	139±16 ^a		
129.4					29±23 ^a	143±16 ^a		
158.8					34±19 ^a	122±14 ^a		

References: (a) Peng et al. (2004)

Chapter 6

Conclusions

In order to calibrate the CO bandhead for kinematic analysis, we have obtained spectra and measured the stellar kinematics in a sample of 25 nearby early-type galaxies (with velocity dispersions from less than 100 km s^{-1} to over 300 km s^{-1}) using the near-infrared CO absorption bandhead at $2.29 \mu\text{m}$. Our median uncertainty for the dispersions is $\sim 10\%$. We examine the effects of dust on existing optical kinematic measurements. We find that the near-infrared velocity dispersions are in general smaller than optical velocity dispersions, with differences as large as 30%. The median difference is 11% smaller, and the effect is of greater magnitude for higher dispersion galaxies. The lenticular galaxies (18 out of 25) appear to be causing the shift to lower dispersions while the classical ellipticals (7 out of 25) are consistent between the two wavelength regimes. If uniformly distributed dust causes these differences, we would expect to find a correlation between the relative amount of dust in a galaxy and the fractional change in dispersion, but we do not find such a correlation. We do see correlations both between velocity dispersion and CO bandhead equivalent width, and velocity dispersion and Mg_2 index. The differences in dispersion are not well explained by current models of dust absorption. The lack of correlation between the relative amount of dust and shift in dispersion possibly

suggests that dust does not have a similar distribution from galaxy to galaxy. Some of the galaxies with the most discrepant values of optical and near-IR dispersions show evidence of dust disks or clumpy dust, but others do not. The CO equivalent widths of these galaxies are quite high ($\geq 10 \text{ \AA}$ for almost all), requiring the light at these wavelengths to be dominated by very cool stars.

We combine near-infrared stellar kinematic measurements with the photometry of 2MASS to build an all-infrared Fundamental Plane (FP). We use the CO bandhead at $2.29 \mu\text{m}$ to measure the stellar kinematics of a sample of 35 nearby elliptical galaxies. Combined with K -band imaging of these galaxies available from 2MASS, we examine the tight relationship among the structural and kinematic properties of galaxies known as the FP. The FP provides important clues and constraints for how galaxies form and evolve (i.e. evolution of FP with redshift, galaxy type, etc.). We find a best-fit FP relationship of

$$r_{eff} \propto \sigma^{1.72 \pm 0.09} I_{eff}^{-0.62 \pm 0.06}.$$

This is a markedly steep FP relationship, especially compared to those observed using optical wavelengths. These differences indicate that although breakdown of homology may play a role in the tilt of the FP, variation of M/L with galaxy properties such as luminosity must also play a role. The intrinsic scatter for our infrared FP relationship ($\text{rms} = 0.069$) is similar to local optical samples, implying that galaxy-to-galaxy differences in dust content, star formation history, or metallicity are not the driving force behind the thickness of the FP.

We combine near-infrared stellar kinematic measurements with the photometry of 2MASS to place bulges of late-type galaxies on the Fundamental Plane (FP) of galaxies. We use the CO bandhead at $2.29 \mu\text{m}$ to measure the stellar kinematics of a sample of nearby spiral galaxies. Combined with K -band imaging of these galaxies available from 2MASS, we examine the tight relationship among the structural and

kinematic properties of galaxies known as the FP. The FP provides important clues and constraints for how galaxies form and evolve (i.e. evolution of FP with redshift, galaxy type, etc.). We find a best-fit FP relationship of

$$r_{eff} \propto \sigma^{1.94 \pm 0.12} I_{eff}^{-0.51 \pm 0.09}.$$

This is significantly different from FP relationships for early-type galaxies, indicating that bulges are distinct from elliptical galaxies with different structural and/or population characteristics. The intrinsic scatter ($\text{rms} = 0.088$) is larger than that for early-type samples, consistent with our view of bulges as a less homogeneous family than elliptical galaxies.

Infrared spectrographs such as GNIRS on Gemini South unlock new possibilities to study the central black holes in dusty galaxies that have been inaccessible to previous black hole studies. We exploit good near-infrared seeing to measure the central black hole (BH) of Centaurus A (NGC 5128). We measure the stellar kinematics of NGC 5128 using the region around the CO bandheads at $2.3 \mu\text{m}$ and determine the black hole mass using axisymmetric orbit-based models. Black holes are believed to be essential components of galaxies, and their evolutionary states appear to be closely linked to those of their hosts. Our current knowledge does not go much beyond this; galaxies such as NGC 5128 (an AGN and recent merger) can further develop this knowledge. However, NGC 5128 and galaxies like it contain large amounts of dust which hamper optical spectroscopy, making near-infrared measurements an attractive alternative. We find a BH mass of $2.4_{-0.2}^{+0.3} \times 10^8 M_{\odot}$ for an edge-on model, $1.8_{-0.4}^{+0.4} \times 10^8 M_{\odot}$ for a model with inclination of 45° , and $1.5_{-0.2}^{+0.3} \times 10^8 M_{\odot}$ for a model with inclination of 20° . We adopt the value for the edge-on model since it has significantly lower χ^2 ; however, it is unlikely that we can constrain the actual inclination of moderately triaxial NGC5128 using an axisymmetric modeling procedure. These estimates, based on adjusting the asym-

metric kinematics of NGC 5128 so we can use an axisymmetric code, are consistent with the range of acceptable BH masses implied by a previous gas dynamical study. However, these estimates are five to ten times higher than that predicted by the correlation between BH mass and velocity dispersion. If NGC 5128 will eventually follow the trend for quiescent galaxies, this result suggests that its BH assembled first before its host component. NGC 5128 thus provides an important example for our knowledge of central black holes; this technique can be applied to other such galaxies to further explore this question.

This observational treatment opens up a new avenue for black hole research, Fundamental Plane studies, and a variety of other areas that rely on kinematic measurements. It allows us to probe the most interesting galaxies; Cen A is a prime example. We are also able to utilize adaptive optics, which only work well in the near-IR; we have used this technique to measure the BH mass of NGC 4486A. No longer are messy, dusty, and complicated galaxies outside the realm of our kinematic tools. This dissertation project opens up many new possibilities for expanding our dynamical understanding of nearby galaxies.

Bibliography

- Andredakis, Y. C., Peletier, R. F., & Balcells, M. 1995, MNRAS, 275, 874
- Andredakis, Y. C. & Sanders, R. H. 1994, MNRAS, 267, 283
- Baade, W. & Minkowski, R. 1954, ApJ, 119, 215
- Baes, M. & Dejonghe, H. 2000, MNRAS, 313, 153
- . 2001, ApJL, 563, L19
- . 2002, MNRAS, 335, 441
- Baes, M., Dejonghe, H., & De Rijcke, S. 2000, MNRAS, 318, 798
- Balcells, M., Graham, A. W., & Peletier, R. F. 2004, ArXiv Astrophysics e-prints astro-ph/0404381
- Barth, A. J., Ho, L. C., & Sargent, W. L. W. 2002, AJ, 124, 2607
- Beers, T. C., Flynn, K., & Gebhardt, K. 1990, AJ, 100, 32
- Bender, R., Burstein, D., & Faber, S. M. 1992, ApJ, 399, 462
- Bernardi, M., Sheth, R. K., Annis, J., et al. 2003a, AJ, 125, 1866
- . 2003b, AJ, 125, 1817
- Bower, G. A., Green, R. F., Bender, R., et al. 2001, ApJ, 550, 75

- Burstein, D., Bertola, F., Buson, L. M., Faber, S. M., & Lauer, T. R. 1988, *ApJ*, 328, 440
- Busarello, G., Capaccioli, M., Capozziello, S., Longo, G., & Puddu, E. 1997, *A&A*, 320, 415
- Cappellari, M. 2002, *MNRAS*, 333, 400
- Cappellari, M., Bacon, R., Bureau, M., et al. 2005, *ArXiv Astrophysics e-prints* astro-ph/0505042
- Carollo, C. M. 1999, *ApJ*, 523, 566
- Carollo, C. M., Stiavelli, M., de Zeeuw, P. T., & Mack, J. 1997, *AJ*, 114, 2366
- Carollo, C. M., Stiavelli, M., de Zeeuw, P. T., Seigar, M., & Dejonghe, H. 2001, *ApJ*, 546, 216
- Carollo, C. M., Stiavelli, M., & Mack, J. 1998, *AJ*, 116, 68
- Carollo, C. M., Stiavelli, M., Seigar, M., de Zeeuw, P. T., & Dejonghe, H. 2002, *AJ*, 123, 159
- Ciotti, L., Lanzoni, B., & Renzini, A. 1996, *MNRAS*, 282, 1
- Cutri, R. M., Skrutskie, M. F., Van Dyk, S., et al. 2003, Explanatory supplement to the 2MASS All Sky Data Release (Pasadena: Caltech)
- Davies, R. L., Burstein, D., Dressler, A., et al. 1987, *ApJS*, 64, 581
- di Nella, H., Garcia, A. M., Garnier, R., & Paturel, G. 1995, *A&AS*, 113, 151
- Djorgovski, S. & Davis, M. 1987, *ApJ*, 313, 59
- Doyon, R., Wells, M., Wright, G. S., et al. 1994, *ApJL*, 437, L23

- Dressler, A., Lynden-Bell, D., Burstein, D., et al. 1987, ApJ, 313, 42
- Drory, N., Bender, R., Feulner, G., et al. 2004, ApJ, 608, 742
- Erwin, P. & Sparke, L. S. 2003, ApJS, 146, 299
- Förster Schreiber, N. M. 2000, AJ, 120, 2089
- Faber, S. M. & Jackson, R. E. 1976, ApJ, 204, 668
- Faber, S. M., Wegner, G., Burstein, D., et al. 1989, ApJS, 69, 763
- Fabian, A. C. 1999, MNRAS, 308, L39
- Falcón-Barroso, J., Peletier, R. F., & Balcells, M. 2002, MNRAS, 335, 741
- Ferrarese, L. & Merritt, D. 2000, ApJL, 539, L9
- Fisher, D. 1997, AJ, 113, 950
- Fisher, D., Franx, M., & Illingworth, G. 1996, ApJ, 459, 110
- Gaffney, N. I., Lester, D. F., & Doppmann, G. 1995, PASP, 107, 68
- Gaffney, N. I., Lester, D. F., & Telesco, C. M. 1993, ApJL, 407, L57
- Gebhardt, K., Bender, R., Bower, G., et al. 2000a, ApJL, 539, L13
- Gebhardt, K., Kormendy, J., Ho, L. C., et al. 2000b, ApJL, 543, L5
- Gebhardt, K., Richstone, D., Kormendy, J., et al. 2000c, AJ, 119, 1157
- Gebhardt, K., Richstone, D., Tremaine, S., et al. 2003, ApJ, 583, 92
- Golev, V. & Prugniel, P. 1998, A&AS, 132, 255
- Goudfrooij, P. & de Jong, T. 1995, A&A, 298, 784
- Graham, A. & Colless, M. 1997, MNRAS, 287, 221

- Haehnelt, M. G. & Kauffmann, G. 2000, MNRAS, 318, L35
- Hildebrand, R. H. 1983, QJRAS, 24, 267
- Ho, L. C. W. 2004, in *Coevolution of Black Holes and Galaxies*, 293–+
- Huchra, J. P., Brodie, J. P., Caldwell, N., Christian, C., & Schommer, R. 1996, ApJS, 102, 29
- Hui, X., Ford, H. C., Freeman, K. C., & Dopita, M. A. 1995, ApJ, 449, 592
- Israel, F. P. 1998, ARA&A, 8, 237
- Jarrett, T. H., Chester, T., Cutri, R., et al. 2000, AJ, 119, 2498
- Jarrett, T. H., Chester, T., Cutri, R., Schneider, S. E., & Huchra, J. P. 2003, AJ, 125, 525
- Jorgensen, I., Franx, M., & Kjaergaard, P. 1995, MNRAS, 276, 1341
- . 1996, MNRAS, 280, 167
- Kauffmann, G., Heckman, T. M., White, S. D. M., et al. 2003, MNRAS, 341, 33
- Kelson, D. D., Illingworth, G. D., van Dokkum, P. G., & Franx, M. 2000, ApJ, 531, 184
- King, A. 2003, ApJL, 596, L27
- Kleinmann, S. G. & Hall, D. N. B. 1986, ApJS, 62, 501
- Knapp, G. R., Guhathakurta, P., Kim, D., & Jura, M. A. 1989, ApJS, 70, 329
- Kormendy, J. 1977, ApJ, 218, 333
- Kormendy, J., Bender, R., Evans, A. S., & Richstone, D. 1998, AJ, 115, 1823

- Kormendy, J. & Djorgovski, S. 1989, *ARA&A*, 27, 235
- Kormendy, J. & Freeman, K. C. 2004, in *IAU Symposium*, 377–+
- Kormendy, J. & Kennicutt, R. C. 2004, *ARA&A*, 42, 603
- Kraan-Korteweg, R. C. 1986, *A&AS*, 66, 255
- Kwan, J. & Xie, S. 1992, *ApJ*, 398, 105
- Lauer, T. R., Ajhar, E. A., Byun, Y.-I., et al. 1995, *AJ*, 110, 2622
- Lester, D. F. & Gaffney, N. I. 1994, *ApJL*, 431, L13
- Lester, D. F., Hill, G. J., Doppmann, G., & Froning, C. S. 2000, *PASP*, 112, 384
- Malin, D. F., Quinn, P. J., & Graham, J. A. 1983, *ApJL*, 272, L5
- Marconi, A., Capetti, A., Axon, D. J., et al. 2001, *ApJ*, 549, 915
- Marconi, A. & Hunt, L. K. 2003, *ApJL*, 589, L21
- Marconi, A., Schreier, E. J., Koekemoer, A., et al. 2000, *ApJ*, 528, 276
- Mathis, J. S., Ruml, W., & Nordsieck, K. H. 1977, *ApJ*, 217, 425
- Mathis, J. S. & Whiffen, G. 1989, *ApJ*, 341, 808
- Mobasher, B., Guzman, R., Aragon-Salamanca, A., & Zepf, S. 1999, *MNRAS*, 304, 225
- Moriondo, G., Giovanardi, C., & Hunt, L. K. 1998, *A&A*, 339, 409
- Moriondo, G., Giovanelli, R., & Haynes, M. P. 1999, *A&A*, 346, 415
- Murray, N., Quataert, E., & Thompson, T. A. 2005, *ApJ*, 618, 569
- Nelson, C. H. & Whittle, M. 1995, *ApJS*, 99, 67

- Origlia, L. & Oliva, E. 2000, *A&A*, 357, 61
- Ostriker, J. P. 2000, *Physical Review Letters*, 84, 5258
- Pahre, M. A., Djorgovski, S. G., & de Carvalho, R. R. 1998, *AJ*, 116, 1591
- Peletier, R. F. 1993, *A&A*, 271, 51
- Peng, C. Y., Ho, L. C., Impey, C. D., & Rix, H. 2002, *AJ*, 124, 266
- Peng, E. W., Ford, H. C., & Freeman, K. C. 2004, *ApJ*, 602, 685
- Puxley, P. J., Doyon, R., & Ward, M. J. 1997, *ApJ*, 476, 120
- Quillen, A. C., Graham, J. R., & Frogel, J. A. 1993, *ApJ*, 412, 550
- Rayner, J. T., Toomey, D. W., Onaka, P. M., et al. 2003, *PASP*, 115, 362
- Rejkuba, M. 2004, *A&A*, 413, 903
- Renzini, A. 1999, in *The Formation of Galactic Bulges*, 9–+
- Rest, A., van den Bosch, F. C., Jaffe, W., et al. 2001, *AJ*, 121, 2431
- Richstone, D., Gebhardt, K., Aller, M., et al. 2004, *ArXiv Astrophysics e-prints* astro-ph/0403257
- Richstone, D. O. & Tremaine, S. 1988, *ApJ*, 327, 82
- Rieke, G. H. & Lebofsky, M. J. 1979, *ARA&A*, 17, 477
- Rowan-Robinson, M. 1986, *MNRAS*, 219, 737
- Sargent, W. L. W., Schechter, P. L., Boksenberg, A., & Shortridge, K. 1977, *ApJ*, 212, 326
- Sarzi, M., Rix, H., Shields, J. C., et al. 2002, *ApJ*, 567, 237

- Schreier, E. J., Marconi, A., Axon, D. J., et al. 1998, *ApJL*, 499, L143+
- Schwarzschild, M. 1979, *ApJ*, 232, 236
- Shields, G. A., Gebhardt, K., Salviander, S., et al. 2003, *ApJ*, 583, 124
- Shier, L. M., Rieke, M. J., & Rieke, G. H. 1994, *ApJL*, 433, L9
- . 1996, *ApJ*, 470, 222
- Silge, J. D. & Gebhardt, K. 2003, *AJ*, 125, 2809
- . 2005, *AJ*, submitted
- Silge, J. D., Gebhardt, K., Bergmann, M., & Richstone, D. 2005, *AJ*, in press
- Silk, J. & Rees, M. J. 1998, *A&A*, 331, L1
- Springel, V., Di Matteo, T., & Hernquist, L. 2004, *ArXiv Astrophysics e-prints* astro-ph/0411108
- Tamura, M., Kleinmann, S. G., Scoville, N. Z., & Joyce, R. R. 1991, *ApJ*, 371, 131
- Thomas, J., Saglia, R. P., Bender, R., et al. 2004, *MNRAS*, 353, 391
- Tonry, J. & Davis, M. 1979, *AJ*, 84, 1511
- Tonry, J. L. & Davis, M. 1981, *ApJ*, 246, 666
- Tonry, J. L., Dressler, A., Blakeslee, J. P., et al. 2001, *ApJ*, 546, 681
- Trager, S. C., Worthey, G., Faber, S. M., Burstein, D., & Gonzalez, J. J. 1998, *ApJS*, 116, 1
- Tran, H. D., Tsvetanov, Z., Ford, H. C., et al. 2001, *AJ*, 121, 2928
- Treu, R., Ellis, R. S., Liao, T. X., et al. 2005, *ArXiv Astrophysics e-prints* astro-ph/0503164

- Trujillo, I., Burkert, A., & Bell, E. F. 2004, ApJ, 600, L39
- van der Marel, R. P., Rix, H. W., Carter, D., et al. 1994, MNRAS, 268, 521
- van Dokkum, P. G. & Franx, M. 1995, AJ, 110, 2027
- van Dokkum, P. G., Franx, M., Kelson, D. D., & Illingworth, G. D. 1998, ApJ, 504, L17+
- Wahba, G. 1990, Spline Models for Observational Data (Society for Industrial & Applied Math)
- Wallace, L. & Hinkle, K. 1997, ApJS, 111, 445
- Walter, F., Carilli, C., Bertoldi, F., et al. 2004, ApJL, 615, L17
- White, S. D. M., Davis, M., Huchra, J., & Latham, D. 1983, MNRAS, 203, 701
- Wiklind, T. & Henkel, C. 1995, A&A, 297, L71
- Wilkinson, A., Sharples, R. M., Fosbury, R. A. E., & Wallace, P. T. 1986, MNRAS, 218, 297

Vita

Julia Dorothea Silge was born in Fort Worth, Texas, on June 10, 1978, the daughter of Linda Hoener Smith and Paul Fielding Smith. She graduated from Lake Country Christian School in Fort Worth in 1996 and Texas A&M University in College Station in 2000 with a Bachelor of Science in physics. In 2000, she began graduate studies in astronomy at the University of Texas at Austin under the supervision of Karl Gebhardt, completing a Master of Arts in astronomy in 2002. She married Robert Lawrence Silge, a graduate of Texas A&M University and the University of Texas Southwestern Medical School, in June 2002.

Permanent Address: 89 Central Ave.

Hamden, CT 06517

This dissertation was typeset with $\text{\LaTeX 2}_{\epsilon}$ ¹ by the author.

¹ $\text{\LaTeX 2}_{\epsilon}$ is an extension of \LaTeX . \LaTeX is a collection of macros for \TeX . \TeX is a trademark of the American Mathematical Society. The macros used in formatting this dissertation were written by Dinesh Das, Department of Computer Sciences, The University of Texas at Austin, and extended by Bert Kay, James A. Bednar, and Ayman El-Khashab.